

University of Windsor

## Scholarship at UWindor

---

Electronic Theses and Dissertations

Theses, Dissertations, and Major Papers

---

8-3-2017

### Investigation of the Formability of TRIP780 Steel Sheets

Yang Song

*University of Windsor*

Follow this and additional works at: <https://scholar.uwindsor.ca/etd>

---

#### Recommended Citation

Song, Yang, "Investigation of the Formability of TRIP780 Steel Sheets" (2017). *Electronic Theses and Dissertations*. 6602.

<https://scholar.uwindsor.ca/etd/6602>

This online database contains the full-text of PhD dissertations and Masters' theses of University of Windsor students from 1954 forward. These documents are made available for personal study and research purposes only, in accordance with the Canadian Copyright Act and the Creative Commons license—CC BY-NC-ND (Attribution, Non-Commercial, No Derivative Works). Under this license, works must always be attributed to the copyright holder (original author), cannot be used for any commercial purposes, and may not be altered. Any other use would require the permission of the copyright holder. Students may inquire about withdrawing their dissertation and/or thesis from this database. For additional inquiries, please contact the repository administrator via email ([scholarship@uwindsor.ca](mailto:scholarship@uwindsor.ca)) or by telephone at 519-253-3000ext. 3208.

**Investigation of the Formability of TRIP780 Steel Sheets**

By

**Yang Song**

A Thesis

Submitted to the Faculty of Graduate Studies  
through the Department of **Mechanical, Automotive & Materials Engineering**  
in Partial Fulfillment of the Requirements for  
the Degree of **Master of Applied Science**  
at the University of Windsor

Windsor, Ontario, Canada

2017

© 2017 Yang Song

**Investigation of the Formability of TRIP780 Steel Sheets**

By

**Yang Song**

APPROVED BY:

---

A. Alpas  
Mechanical, Automotive & Materials Engineering

---

W. Altenhof  
Mechanical, Automotive & Materials Engineering

---

D. Green, Advisor  
Mechanical, Automotive & Materials Engineering

June 2<sup>nd</sup>, 2017

## **Declaration of Originality**

I hereby certify that I am the sole author of this thesis and that no part of this thesis has been published or submitted for publication.

I certify that, to the best of my knowledge, my thesis does not infringe upon anyone's copyright nor violate any proprietary rights and that any ideas, techniques, quotations, or any other material from the work of other people included in my thesis, published or otherwise, are fully acknowledged in accordance with the standard referencing practices. Furthermore, to the extent that I have included copyrighted material that surpasses the bounds of fair dealing within the meaning of the Canada Copyright Act, I certify that I have obtained a written permission from the copyright owner(s) to include such material(s) in my thesis and have included copies of such copyright clearances to my appendix.

I declare that this is a true copy of my thesis, including any final revisions, as approved by my thesis committee and the Graduate Studies office, and that this thesis has not been submitted for a higher degree to any other University or Institution.

## **Abstract**

The formability of a metal sheet is dependent on its work hardening behaviour and its forming limits; and both aspects must be carefully determined in order to accurately simulate a particular forming process. This research aims to characterize the formability of a TRIP780 sheet steel using advanced experimental testing and analysis techniques. A series of flat rolling and tensile tests, as well as shear tests were conducted to determine the large deformation work hardening behaviour of this TRIP780 steel. Nakazima tests were carried out up to fracture to determine the forming limits of this sheet material. A highly-automated method for generating a robust FLC for sheet materials from DIC strain measurements was created with the help of finite element simulations, and evaluated against the conventional method. A correction algorithm that aims to compensate for the process dependent effects in the Nakazima test was implemented and tested with some success.

## Acknowledgements

I would like to express my sincere gratitude to my advisor, Dr. D. E. Green, for allowing me the opportunity to complete this project, and for his patience, commitment and guidance that continuously helped me throughout the course of my study and research. Dr. Green is my mentor and a person I look up to as a role model.

My sincere appreciation to Dr. W. Altenhof for sharing his knowledge and expertise in finite element simulations, the inputs specific to the package of LS-DYNA, and also for lending the DIC cameras which were crucial to this work. I would also like to express my appreciation to Dr. A. Alpas for his support, valuable comments, and suggestions to improve the thesis.

Sincere thanks to Ms. Isadora van Riemsdijk from Arcelormittal Dofasco for sponsoring the TRIP material and providing material data.

Sincere thanks to the technologists in the Faculty of Engineering at the University of Windsor, but especially to Mr. Andrew Jenner. Andy was always helpful throughout the course of my research and has devoted an incredible amount of time and effort, helping with specimen preparation, equipment builds and setups, just to name a few. Special thanks to Matthew Bondy, for his invaluable help in experiments. Matt tutored me in the use of a lot of the experimental equipment used in this project, including the MTS universal testing machines and the DIC system. He is my “go to” person for technical difficulties.

My thanks also to my fellow colleagues in the CRC metal forming laboratory, Alexandra Rose and Mario Vasilescu, for their help in experimental setup and testing. Discussions with them inspired improvements in the setup and procedure for numerous experiments.

# Table of Contents

Declaration of Originality .....	iii
Abstract .....	iv
Acknowledgements .....	v
List of Figures .....	x
List of Tables .....	xv
Nomenclature and Abbreviations .....	xvi
1 . Introduction.....	1
1.1 Background .....	1
1.2 Motivation.....	2
1.3 Research Objectives.....	4
1.4 Outline of the Thesis .....	5
2 . Literature Review.....	6
2.1 Continuum Mechanics and Constitutive Equations .....	6
2.1.1 Strain definitions .....	6
2.1.2 Yielding Criterion and Plasticity .....	7
2.1.3 Anisotropy.....	8

2.1.4	Hill’s 1948 Anisotropic Yield Criterion .....	8
2.1.5	Hill’s 1990 Anisotropic Yield Criterion .....	9
2.1.6	Barlat’s 1989 Anisotropic Yield Criterion.....	10
2.2	Mechanical Tests for Work Hardening Behaviour .....	10
2.2.1	Uniaxial Tensile Test (modified with pre-strains from rolling).....	10
2.2.2	Shear Test.....	12
2.2.3	Hydraulic Bulge Test .....	13
2.3	Work Hardening Models.....	14
2.3.1	Power Law Model.....	14
2.3.2	Johnson-Cook Model .....	15
2.3.3	Khan-Huang-Liang (KHL) Model.....	16
2.4	Transformation Induced Plasticity (TRIP).....	16
2.4.1	TRIP Material Properties from a Microscopic Aspect .....	17
2.4.2	Processing and Application of TRIP Steels .....	19
2.5	Digital Image Correlation (DIC).....	20
2.6	Forming Limit and Formability Tests.....	23
2.6.1	Experimental determination of FLC .....	23



2.6.2	Formability Tests .....	24
2.6.2.1	Nakazima Test .....	24
2.6.2.2	Marciniak Test .....	26
2.6.3	Measuring Strain and Identifying the Onset of Necking .....	26
2.6.3.1	The Traditional North American Method.....	26
2.6.3.2	The Bragard Method.....	27
2.6.3.3	DIC Analysis Methods .....	28
2.6.4	Compensation for Process-Dependent Effects in Nakazima Tests.....	37
2.7	Summary of Literature Review.....	39
3 .	Research Methodology .....	40
3.1	Uniaxial Tensile Tests Combined with Incremental Rolling.....	40
3.2	Shear Tests .....	42
3.3	Finite Element Simulation of Nakazima Tests .....	43
3.4	Formability Tests .....	47
4 .	Results and Analysis .....	50
4.1	Tensile Test Results Analysis .....	50
4.2	Shear Test Results Analysis.....	54
4.3	Simulation Results Analysis .....	56

4.4	Analysis of Nakazima Test Results .....	61
5 .	Discussion .....	70
5.1	The Work Hardening Behaviour of TRIP780.....	70
5.2	Forming Limits of TRIP780 .....	72
6 .	Conclusions, Recommendations and Future Work.....	80
	Bibliography .....	82
	Appendix.....	88
	Appendix A – Rolling and Tensile Test.....	88
	Appendix B – Reduced Keyword Input .....	89
	Appendix C – Nakazima Specimen Geometries .....	95
	Appendix D – Nakazima Testing Procedure.....	101
	Appendix E – Nakazima Testing Setup .....	106
	Appendix F – Finite Element Results Verification .....	107
	Vita Auctoris.....	108

## List of Figures

Figure 1 – FLC of two grades of steel sheet generated from DIC data [3].....	3
Figure 2 – ASTM E8 specimen geometry [10] (dimensions in mm) .....	11
Figure 3 – Shear test specimen used by Sarker [14] (dimensions in mm).....	12
Figure 4 – Schematic of a bulge test [17] .....	13
Figure 5 – Relationship between ductility and strength for various grades of steel [24] .	17
Figure 6 – Schematic representation of the microstructure of TRIP steels [24].....	18
Figure 7 – FCC to BCC/BCT lattice transformation [25] .....	19
Figure 8 – Illustration of the epipolar constraint in DIC [29].....	22
Figure 9 – Schematic of the stereo vision DIC system [29] .....	23
Figure 10 – Example of an FLC [30].....	24
Figure 11 – Schematic of the Nakazima test [32].....	25
Figure 12 – Schematic of the Marciniak test [32].....	26
Figure 13 – FLC of 1.5mm DP600 sheet generated from DIC data [23] .....	28
Figure 14 – Example of 2D contours of the top surface geometry of a plane strain Nakazima specimen [36].....	30
Figure 15 – Description of the surface slope criterion [36] .....	30

Figure 16 – Illustration of the strain rate departure criterion [36] .....	31
Figure 17 – Description of the surface height difference criterion [38] .....	32
Figure 18 – Illustration of the strain gradient increment criterion [37] .....	34
Figure 19 – Illustration of the transition of incremental strain path criterion [39]. .....	34
Figure 20 – Example of the 2 <sup>nd</sup> derivative of thickness strain criterion [39]. .....	35
Figure 21 – Illustration of the maximum load criterion applied to uniaxial tension test data [40] .....	36
Figure 22 – Preparation of tensile specimen .....	41
Figure 23 – Shear test specimen with speckle pattern in the two gauge areas .....	42
Figure 24 – Shear test fixture .....	43
Figure 25 – A quarter simulation model for a fully clamped Nakazima test .....	46
Figure 26 – Section view of Nakazima test tooling .....	49
Figure 27 – Nakazima test process flow chart .....	49
Figure 28 – Tensile stress-strain curve .....	51
Figure 29 – R-value vs. true plastic strain .....	53
Figure 30 – Extended flow curve (RD) obtained from tensile tests after successive flat rolling .....	53
Figure 31 – Extended flow curve (TD) obtained from tensile tests after successive flat rolling .....	54

Figure 32 – Shear stress - principal strain curves obtained from a shear test.....	55
Figure 33 – Normal/shear strain ratio in a shear test .....	55
Figure 34 – Shear test flow curves.....	56
Figure 35 – Finite element model of a plane strain Nakazima specimen showing the distribution of the effective strain .....	57
Figure 36 – Validation of the predicted strain distribution in a plane-strain Nakazima test specimen in terms of, a) the major strain, b) the minor strain .....	58
Figure 37 – Validation of the predicted strain path for a point near the center of a plane strain Nakazima specimen, with mesh sensitivity analysis.....	59
Figure 38 – Photograph of plane-strain Nakazima specimens: a) the undeformed blank, and b) the as-formed specimen .....	60
Figure 39 – Experimental strain paths in the Nakazima tests determined using DIC .....	62
Figure 40 – Example of the strain-rate departure criterion for a Nakazima test specimen deformed along strain path #2.....	64
Figure 41 – Evolution of the 2D cross-sectional contour of the top surface of a Nakazima specimen, $t = [0, 47.58]$ sec .....	65
Figure 42 – 1 <sup>st</sup> derivative of a cross-sectional contour from Figure 41 .....	65
Figure 43 – 2 <sup>nd</sup> derivative of a cross-sectional contour from Figure 41 .....	66
Figure 44 – Maximum 2 <sup>nd</sup> derivative of cross-sectional contour vs. time.....	66
Figure 45 – Evolution of the 2 <sup>nd</sup> derivative of strains in time .....	68

Figure 46 – An illustration of strain history for outer, middle and inner layers of a Nakazima specimen .....	69
Figure 47 – Forming limit strain results after different corrections (SP: strain path correction; CP: contact pressure correction) .....	69
Figure 48 – The work hardening behaviour of TRIP780.....	70
Figure 49 – Extended flow curve (RD) obtained from tensile tests after successive flat rolling .....	71
Figure 50 – Extended flow curve (TD) obtained from tensile tests after successive flat rolling .....	71
Figure 51 – Conventional FLC of the TRIP780 determined by the Keeler method.....	73
Figure 52 – Comparison of FLC’s for TRIP780 obtained using different strain measurements.....	74
Figure 53 – FLC of TRIP780 generated with the surface-slope criterion .....	75
Figure 54 – FLC of TRIP780 generated with the strain-rate departure criterion .....	76
Figure 55 – Comparison of FLC’s for TRIP780 obtained using different analysis methods .....	77
Figure 56 – FLC of TRIP780 generated with the surface-slope criterion (compensated)	78
Figure 57 – FLC of TRIP780 generated with the strain-rate departure criterion (compensated) .....	79
Figure 58 – the Flat Roller, the EDM tensile specimen and the tensile test setup.....	88

Figure 59 – Nakazima test setup.....	106
Figure 60 – Energy plot for the entire model of simulation .....	107
Figure 61 – Contact force couples, No.1, 2 and 3 represent punch-specimen, upper die-specimen and lower die-specimen. ....	107

## List of Tables

Table 1 – TRIP780 Chemical Composition.....	16
Table 2 – TRIP780 As-received Material Properties.....	17
Table 3 – Rolling Strain.....	52



## Nomenclature and Abbreviations

<b>Term</b>	<b>Explanation</b>
AHSS	Advanced High Strength Steels
AOI	Area of Interest
CGA/SGA	Circle/Square Grid Analysis
DIC	Digital Image Correlation
EDM	Electrical Discharge Machining
FE, FEA	Finite Element, Finite Element Analysis
FLC, FLD	Forming Limit Curve, Forming Limit Diagram
FLC <sub>0</sub>	Plane strain intercept of the Forming Limit Curve
FMTI	Forming Measurement Tool Innovations
LVDT	Linear Variable Differential Transformer
RMSE	Root Mean Squared Error
TRIP	Transformation Induced Plasticity – a Family of AHSS
TRIP780	A grade of multi-phase TRIP steel with a minimum tensile strength of 780 MPa

# 1. Introduction

## 1.1 Background

The 1973 Oil Crisis in the United States prompted the National Highway Traffic Safety Administration (NHTSA) to establish Corporate Average Fuel Economy (CAFE) regulations to improve the fuel economy of passenger cars and light trucks. Although the Oil Crisis ended, CAFE remained to regulate the fuel consumption of modern automobiles and to control toxic and greenhouse gas emissions. One method to reduce fuel consumption is to reduce vehicle mass.

In the 1990's, new trends in the automotive industry resulted in vehicle mass increases compared to vehicles from previous generations. Complicated shapes, adaptive suspension systems, reinforced uni-body structures, driver assistance systems and in-car infotainment systems have greatly improved the performance of vehicles in terms of handling, structural integrity, safety and comfort. However, these systems also resulted in additional components and increased vehicle mass, which brought many undesirable side effects, including increased fuel consumption and emissions.

In 1998, the UltraLight Steel Auto Body Final Engineering Report [1] was released, detailing the results of work to reduce automobile mass as well as increasing safety performance. The reduction of vehicle mass resulted in increased fuel economy, overall vehicle efficiency, and a reduction in toxic emissions and CO<sub>2</sub> emissions. The UltraLight Steel Auto Body (ULSAB) Consortium achieved this through the introduction of a new generation of steel grades and advanced manufacturing processes.

One significant contribution to the reduction of vehicle mass was the introduction of Advanced High Strength Steels (AHSS) into the body and structure of vehicles. With increased strength, the implementation of AHSS allows for significant reduction in thickness of sheet metal components with comparable or even improved structural integrity and impact resistance. The down-gauging leads to a considerable drop in mass

of vehicle body-in-white, compared to vehicles manufactured from conventional mild steel grades.

## **1.2 Motivation**

AHSS sheets have more complex work hardening behaviour due to their multiphase microstructure as compared to mild steel. The multiphase nature of AHSS sometimes makes it more challenging to acquire material data through experiments and to model the deformation behaviour of the material [2]. The higher strength of the AHSS grades compared to mild steel grades also results in much higher contact forces between the sheet metal and the dies during a forming process. Due to their increased strength, AHSS grades also exhibit greater springback, due to the recovery of the elastic deformation developed in the sheet metal during the forming process. These factors are grounds for more complicated strain histories that can make forming processes more difficult to simulate.

A typical forming process sometimes induces a higher effective strain in the formed part than that attained at maximum load in a uniaxial tensile test. Moreover, the forming of AHSS sheets usually involves higher die contact stresses, which lead to complex, three-dimensional stress states. A reliable method to experimentally determine the work hardening behaviour of AHSS up to high strain levels is crucial to the numerical modeling of the forming of AHSS materials.

Another challenge in the use of AHSS sheet materials in structural and body parts of vehicles is their lower formability and limited post-uniform elongation, as compared to conventional mild steel grades. A sheet metal reaches its limit of formability when the strains localize and a through-thickness neck develops. A forming limit curve (FLC) is a plot in a major strain versus minor strain coordinate system of the lowest threshold strain states beyond which there is a risk of necking. The determination of the forming limit of an AHSS steel grade is more difficult, since the process to develop a neck on a

formability test specimen is less repeatable. Therefore, the work of testing, measuring and determining the forming limit curve (FLC) is more labour-intensive, and the experimental data display more variability. Figure 1 shows an example of FLC produced for two different grades of AHSS that appear difficult to interpret [3].

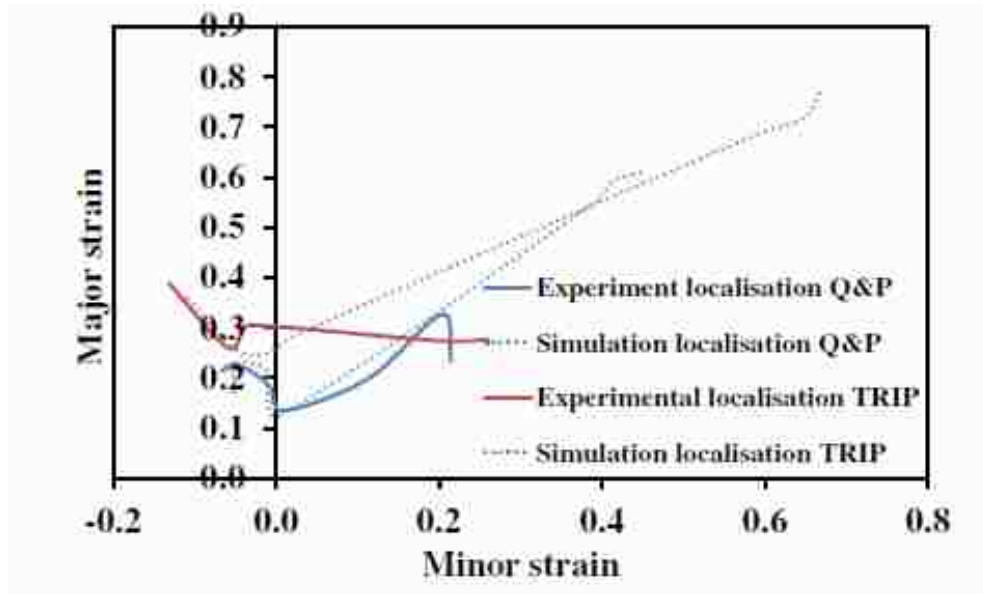


Figure 1 – FLC of two grades of steel sheet generated from DIC data [3]

Characterizing the behaviour of AHSS sheets with accuracy, both in terms of their work hardening behaviour and forming limit, is essential to accurately predict the outcome of a forming process. Automotive part designers utilize the higher work hardening ability of AHSS to make stronger, lighter parts with complex shapes and features, hence need to form the sheet metals to higher strain levels. An FLC is especially important for numerical modeling and process design in the sheet metal forming industry, because it represents the limit strains of the material based on experimental data. The traditional North American grid analysis method (Keeler method), which is commonly used for the experimental determination of FLCs, uses electro-etching to mark the specimens and

requires that the test be stopped just at the onset of necking [4]. The strains in the neck are measured from the electro-etched grids at a single state of deformation after the testing process, and the spatial resolution of the measured strains is generally about 2.5 mm (0.1 inch). The introduction and development of digital image correlation (DIC) in the past two decades has enabled more consistent characterization of sheet forming limits. The DIC method is a non-contact surface deformation measurement method that depends on a random, high-contrast pattern (known as a speckle pattern) applied to the undeformed sheet. The DIC method records digital images throughout the full deformation history of the test piece. With currently available equipment, the spatial resolution of the DIC system can easily get into sub-millimeter level for a standard size formability test specimen. The data obtained through the DIC method is very extensive since it provides a high-resolution measure of the strain field across the specimen at very close time steps throughout the entire deformation history. With the increased amount of strain data acquired from experiments, more details in the deformation history can be extracted to accurately characterize the formability of AHSS sheet metals.

### **1.3 Research Objectives**

The objectives of this research are to characterize the formability of 1.5mm TRIP780 steel sheets (a grade of AHSS) in terms of both its work hardening behaviour and its forming limit. In particular, it will be sought to develop an automated procedure for generating a robust FLC for this and other sheet materials that can be verified with the FLC obtained using the conventional Keeler method which identifies the onset of necking based on visual and tactile evaluations.

## 1.4 Outline of the Thesis

The main subdivisions of the thesis are outlined below:

Chapter 2 is a review of the literature on the topics of constitutive equations, TRIP material properties, experimental methods for material characterization, DIC algorithms for strain measurements, and methods for detecting the onset of necking in formability tests.

Chapter 3 describes the procedures that were used to conduct the numerical simulations, the tests for characterizing the work hardening behaviour and forming limit, and the analyses to verify the change in material microstructure, for the TRIP780 material.

Chapter 4 presents the numerical and experimental results that were obtained. Verification and validation of numerical results were also performed.

Chapter 5 compares the flow curves obtained using different mechanical tests, and also compares the different forming limits obtained with different methods for identifying the onset of necking.

Chapter 6 summarizes the main outcomes of the research. An automated method was developed to determine the FLC from DIC strain data, and suggestions for further improving and calibrating this method are provided.

## 2. Literature Review

This chapter is a review of results from previous studies that forms the basis of the research conducted and documented in this thesis.

### 2.1 Continuum Mechanics and Constitutive Equations

In this first section, some of the important principles and variables that are necessary to describe the constitutive behaviour of metal sheets will be reviewed. This will allow us to select the most appropriate constitutive equations to numerically simulate sheet forming operations.

#### 2.1.1 Strain definitions

Different definitions of strain are used across different fields, and each one is suited to particular deformation conditions, standards, common practices and the input or output requirements of software used for processing the data. It is at the discretion of the researcher to select a definition best suited to the application.

Consider the elongation of a bar from an initial length  $L_0$  to a final length  $L$ . The Seth-Hill family of strain is defined in Equation 2.1. [5]

$$\varepsilon = \frac{1}{\kappa}(\lambda^\kappa - 1), \text{ where } \lambda = \frac{L}{L_0} \text{ and } \kappa \text{ is a chosen integer} \quad (2.1)$$

Lengths are always positive, hence  $0 < \lambda < \infty$ . Some commonly used strain measures correspond to different choices of the parameter  $\kappa$ . [5]

$$\text{Engineering Strain } (\kappa = 1): \varepsilon^{eng} = \lambda - 1 = \frac{L - L_0}{L_0} \quad (2.2)$$

$$\text{True Strain (Henkey, logarithmic, } \kappa \rightarrow 0): \quad \varepsilon^{true} = \ln \lambda = \ln \frac{L}{L_0} \quad (2.3)$$

$$\text{Lagrange Strain (} \kappa = 2): \quad \varepsilon^{Lag} = \frac{1}{2}(\lambda^2 - 1) \quad (2.4)$$

For example, the true strain definition is generally used to define the plastic flow curve. However, it is common practice in the stamping industry to plot FLCs using the engineering strain definition.

### 2.1.2 Yielding Criterion and Plasticity

For many isotropic ductile materials, the von Mises yield criterion (Equation 2.5) gives a good estimate of the state of stress at the onset of yielding.

$$\bar{\sigma} = \frac{1}{\sqrt{2}} \sqrt{(\sigma_1 - \sigma_2)^2 + (\sigma_2 - \sigma_3)^2 + (\sigma_3 - \sigma_1)^2}, \quad (2.5)$$

where  $\bar{\sigma}$  is the effective stress. Yielding is considered to occur when the effective stress is equal to the yield stress in uniaxial tension.

When accounting for the plastic work per unit volume (Equation 2.6), the von Mises effective strain can be calculated as shown in Equation 2.7.

$$dW^p = \sigma_{ij} d\bar{\varepsilon}_{ij}^p = \bar{\sigma} d\bar{\varepsilon}^p \quad (2.6)$$

$$d\bar{\varepsilon}^p = \sqrt{\frac{2}{3} [(d\bar{\varepsilon}_1^p)^2 + (d\bar{\varepsilon}_2^p)^2 + (d\bar{\varepsilon}_3^p)^2]} \quad (2.7)$$



### 2.1.3 Anisotropy

Generally, sheet materials are not entirely isotropic. A material is anisotropic when it possesses different mechanical properties in different directions. Anisotropy in sheet metal typically results from the cold rolling process, where a crystallographic texture develops in a way that strengthens the sheet metal in certain directions.

The degree of anisotropy in a sheet metal is described by Lankford's coefficient, commonly known as the R-value. The R-value is defined as the width-to-thickness true plastic strain ratio, obtained experimentally after a certain level of deformation (e.g. at  $\varepsilon_1 = 0.15$ ) in a uniaxial tensile test (Equation 2.8).

$$R = \frac{\varepsilon_w}{\varepsilon_t} = \frac{\varepsilon_2^p}{\varepsilon_3^p} = \frac{\ln(w/w_0)}{\ln(t/t_0)} \quad (2.8)$$

The thickness strain can be difficult to measure in a uniaxial tensile test, and is generally derived from the major and minor strains with the use of the constant volume assumption under plastic deformation [6]. The R-value is typically measured in the rolling direction, the transverse direction, and at 45° to the rolling direction, to characterize the planar anisotropy. The three R-values can be averaged using Equation 2.9 to obtain an average  $\bar{R}$ , which describes the normal anisotropy of the sheet.

$$\bar{R} = \frac{R_0 + 2R_{45} + R_{90}}{4} \quad (2.9)$$

As the  $\bar{R}$ -value of a material increases, it shows greater resistance to changes in thickness during the forming process.

### 2.1.4 Hill's 1948 Anisotropic Yield Criterion

Hill proposed the first anisotropic yield function for orthotropic sheet materials in 1948, as an extension to von Mises' yield criterion, as shown in Equation 2.10, where  $F$ ,  $G$ ,  $H$ ,  $L$ ,  $M$  and  $N$  are material constants [7].

$$2f(\sigma_{ij}) = F(\sigma_y - \sigma_z)^2 + G(\sigma_z - \sigma_x)^2 + H(\sigma_x - \sigma_y)^2 + 2L\tau_{yz}^2 + 2M\tau_{zx}^2 + 2N\tau_{xy}^2 = 1 \quad (2.10)$$

Hill's 1948 criterion can be expressed in terms of the yield stresses in different orientations of a sheet metal. The effective stress,  $\bar{\sigma}$ , is usually defined from the uniaxial flow stress in the rolling direction. For thin sheet metals, out-of-plane stress components are generally neglected. After reduction, Hill's 1948 yield criterion can be written in terms of R-values, as shown in Equation 2.11.

$$\bar{\sigma}^2 = \frac{(1+R_0)\sigma_x^2 - 2R_0\sigma_x\sigma_y + R_0(1+1/R_{90})\sigma_y^2 + (2R_{45}+1)(1+R_0/R_{90})\tau_{xy}^2}{1+R_0} \quad (2.11)$$

The work-equivalent effective plastic strain based on Hill's 1948 yield criterion, with the R-values reduced to the average  $\bar{R}$ , can be written as shown in Equation 2.12.

$$\bar{\varepsilon}_p = \left\{ \frac{\bar{R}+1}{2\bar{R}+1} [(\bar{R}+1)(\varepsilon_1^2 + \varepsilon_2^2) + 2\bar{R}\varepsilon_1\varepsilon_2] \right\}^{\frac{1}{2}} \quad (2.12)$$

Due to the simplicity of Hill's 1948 criterion, it is very widely implemented in finite element simulation codes as a basic anisotropic yield criterion.

### 2.1.5 Hill's 1990 Anisotropic Yield Criterion

In 1990, Hill [8] proposed another anisotropic yield criterion, to overcome the inherent limitations of criteria previously proposed. This criterion is shown in Equation 2.13, where  $a$ ,  $b$  and  $m$  are material constants.

$$f(\sigma_{ij}) = |\sigma_x - \sigma_y|^m + \left\{ \frac{\sigma_b}{\tau_{y2}} \right\} \left| (\sigma_x - \sigma_y)^2 + \tau_{xy}^2 \right|^{m/2} + |\sigma_x^2 + \sigma_y^2 + 2\tau_{xy}^2|^{(m/2)-1} \{ -2a(\sigma_x^2 + \sigma_y^2) + b(\sigma_x - \sigma_y)^2 \} = (2\bar{\sigma})^m \quad (2.13)$$

### 2.1.6 Barlat's 1989 Anisotropic Yield Criterion

In 1989, Barlat and Lian [9] proposed a non-quadratic yield criterion to describe the behaviour of aluminum sheets with planar anisotropy, as shown in Equation 2.14. This criterion assumes plane stress conditions and the exponent  $m$  is generally equal to 6 for BCC metals or 8 for FCC metals, and  $a$ ,  $c$ ,  $h$  and  $p$  are material constants.

$$f(\bar{\sigma}_{ij}) = a|K_1 + K_2|^m + a|K_1 - K_2|^m + a|K_1 - K_2|^m = 2\bar{\sigma}^m \quad (2.14)$$

$$\text{with } K_1 = \frac{\sigma_x + h\sigma_y}{2} \quad \text{and} \quad K_2 = \sqrt{\left(\frac{\sigma_x + h\sigma_y}{2}\right)^2 + p^2\tau_{xy}^2}$$

## 2.2 Mechanical Tests for Work Hardening Behaviour

Finite element simulations of sheet metal forming processes require a description of the work hardening behaviour of the sheet metal up to large deformations. The work hardening behaviour of a sheet material can be characterized with various mechanical tests which are known to produce slightly different stress-strain flow curves for inherently different deformation modes. The differences in results come from the fact that deformation micro-mechanisms vary depending on the loading condition.

### 2.2.1 Uniaxial Tensile Test (modified with pre-strains from rolling)

The uniaxial tensile test is one of the most common ways of determining the work hardening behaviour of a wide range of materials. Sheet metal specimens are often machined into a “dog bone” geometry, as specified by the ASTM E8/E8M standard [10]. The specimen is then loaded in tension until it fractures. An illustration of the standard geometry is shown in Figure 2 without tolerance specifications.

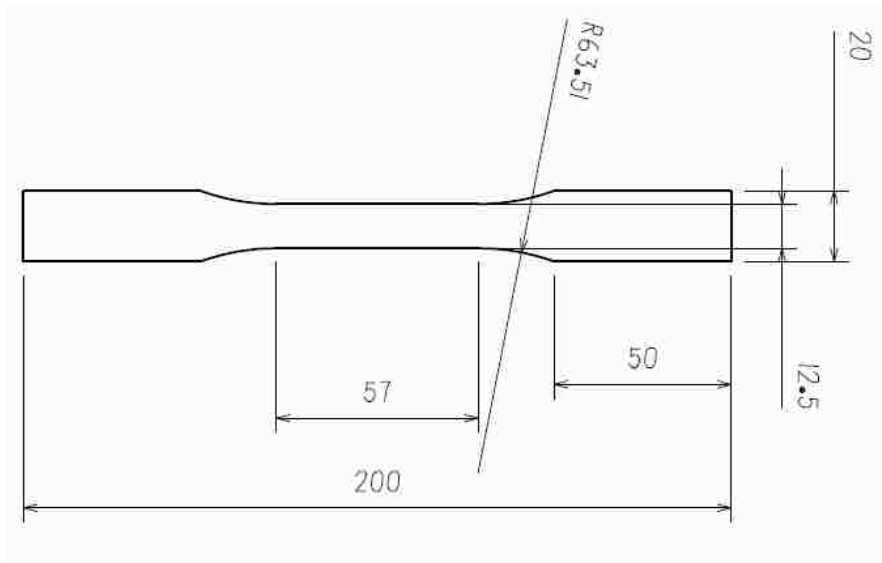


Figure 2 – ASTM E8 specimen geometry [10] (dimensions in mm)

The limitation of a conventional uniaxial tensile test is that it only provides the true stress versus true plastic strain flow curve up to a certain strain level, usually just over 0.2 for typical low carbon steel grades, and even lower for some AHSS grades. However, when the same sheet material is stamped in a set of dies, it can undergo a much greater amount of effective strain than the maximum strain limit in a uniaxial tensile test, due to the biaxial, or even three-dimensional, stress states generated in stamping. The data obtained from tensile testing are insufficient to fully characterize the work hardening behaviour or to carry out FEA simulations. Vasilescu [11] extended the uniaxial tension flow curve of DP600 steel to greater strain levels by pre-straining the material using flat rolling prior to tensile tests. As investigated in the work of Sevillano et al. [12], flat rolling of sheet metals induces homogeneous deformation and is one of the best processes for pre-straining materials up to large strains. Despite the possible discrepancy in the flow curve due to the change in deformation mode, this method provides data up to strains of 1.0 mm/mm or more. The experimental flow curve obtained from successive flat rolling and tensile testing will be more representative of the work hardening behaviour of the sheet than a curve that is extrapolated from a single tensile test.

### 2.2.2 Shear Test

The ideal simple shear loading of an isotropic material creates a deformation mode in which the in-plane principal strains are equal and opposite to each other. The shear test typically provides a flow curve that extends to a higher level of effective strain, compared to that obtained from a uniaxial tension test. The experimental setup for the shear test is usually adapted for use in a universal testing apparatus, with a special fixture made to apply a shearing load.

Different specimen geometries have been investigated to obtain the optimum strain distribution. The ASTM standard [13] specifies a specimen geometry with thin gauge area and large supporting geometry to maintain the alignment in the gauge area, and it is intended to be used in a tensile testing apparatus. A Miyauchi-type of specimen design can be found in previous work from Sarker [14] and Zillmann [15], where there are three clamping areas and two gauge areas that are symmetrically located between the clamped regions. The gauge area on this specimen design is larger; hence, the strain distribution is not strictly in simple shear throughout the gauge area. The benefit is that the setup allows for cyclic testing of shear specimens. Figure 3 shows the specimen geometry.

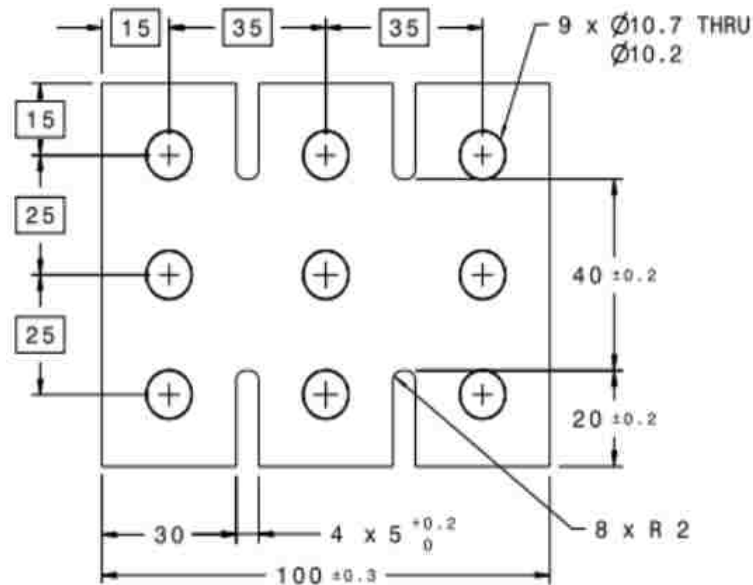


Figure 3 – Shear test specimen used by Sarker [14] (dimensions in mm)

### 2.2.3 Hydraulic Bulge Test

The hydraulic bulge test consists of clamping a circular sheet metal blank around its periphery and applying a hydraulic pressure on one side of the sheet specimen so that it bulges out. The bulge test induces a balanced-biaxial stress state at the apex of the specimen that would lead to a balanced biaxial strain in an isotropic sheet material. It generates stress-strain data up to high strain levels in a single forming process that follows a quasi-linear strain path. The experimental setup requires custom designed tooling to clamp and seal a piece of sheet metal on top of a cavity filled with an incompressible fluid. Koh [16] proposed a bulge test design that uses a plunger to displace the forming fluid, and relies on DIC software to track the height of the bulge. Gutscher et al. [17] proposed a slightly different design that uses a punch to displace the fluid, and a position transducer to track the displacement of the apex of the specimen. Since the fluid acts directly on the specimen, the bulge test achieves a very uniform distribution of stress. A schematic of a typical bulge test can be found in Figure 4.

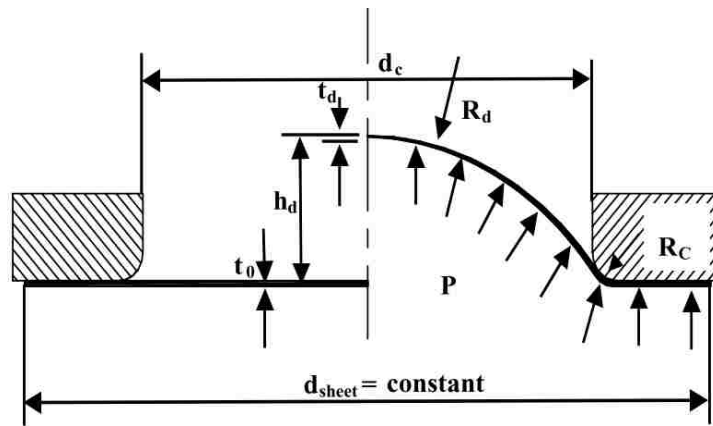


Figure 4 – Schematic of a bulge test [17]

The effective stress and strain,  $\bar{\sigma}$  and  $\bar{\epsilon}$ , are expressed in Equation 2.15 and Equation 2.16, respectively in terms of:  $R_d$ , the instantaneous radius at the apex of the dome,  $t_d$ , the thickness at the apex of the dome,  $p$ , the hydraulic pressure, and  $t_0$ , the initial thickness of the sheet [17].

$$\bar{\sigma} = \left( \frac{R_d}{t_d} + 1 \right) \frac{p}{2} \quad (2.15)$$

$$\bar{\varepsilon} = -\ln \left( \frac{t_d}{t_0} \right) \quad (2.16)$$

Equation 2.17 and Equation 2.18 further express  $R_d$  and  $t_d$  in terms of:  $d_c$ , the diameter of the cavity,  $h_d$ , the height of the dome,  $R_c$ , the die profile radius, and  $n$ , the strain hardening exponent [17].

$$R_d = \frac{(d_c/2 + R_c)^2 + h_d^2 - 2R_ch_d}{2h_d} \quad (2.17)$$

$$t_d = \left( \frac{1}{1 + \left( \frac{2h_d}{d_c} \right)^2} \right)^{2-n} \quad (2.18)$$

An iterative method can be used to determine the flow curve, by first entering an initial guess  $n$  value and all the known parameters, then iteratively calculating and updating  $\bar{\sigma}$ ,  $\bar{\varepsilon}$  and  $n$ , until the difference in  $n$  between iterations are within tolerance (smaller than 0.001 in this case) [17].

## 2.3 Work Hardening Models

The work hardening behavior is generally implemented into numerical simulation codes by using a mathematical model that represents the stress-strain curve of the sheet. In this section, several work hardening models will be reviewed.

### 2.3.1 Power Law Model

In 1909, Ludwik [18] first proposed a power law relation to describe the stress-strain curve of polycrystalline metals (Equation 2.19), where  $\sigma$  is the true stress,  $\sigma_0$  is the true

yield stress,  $\varepsilon$  is the true plastic strain,  $K$  is the strength parameter, and  $n$  is the strain hardening exponent. Holloman used a simplified power law relation in 1945 [19]. As shown in Equation 2.20, this relation is most commonly used to describe the effective stress-strain relation for material work hardening in constant temperature and quasi-static loading conditions. Many more advanced work hardening models are developed based on these simple power law relations.

$$\sigma = \sigma_0 + K \varepsilon_p^n \quad (2.19)$$

$$\sigma = K \varepsilon_p^n \quad (2.20)$$

### 2.3.2 Johnson-Cook Model

Proposed in 1983, the Johnson-Cook [20] model is widely implemented in commercial FE codes. The model is popular for modeling dynamic loading problems due to its capability of handling strain rate effects. As shown in Equation 2.21, the Johnson-Cook model consists of three terms multiplied together: strain hardening, strain rate hardening, and thermal softening. The strain rate term and/or the thermal term can be conveniently removed if that variable is not considered.

$$\sigma = [A + B \varepsilon_p^n] [1 + C \ln \dot{\varepsilon}^*] \left[ 1 - \left( \frac{T - T_r}{T_m - T_r} \right)^m \right] \quad (2.21)$$

In Equation 2.21,  $\varepsilon_p$  represents the plastic strain,  $\dot{\varepsilon}^*$  is the dimensionless strain rate (ratio of instantaneous strain rate over reference strain rate),  $T$ ,  $T_r$ ,  $T_m$  are the instantaneous, room and melting temperatures, and  $A$ ,  $B$ ,  $n$ ,  $C$  and  $m$  are material constants.



### 2.3.3 Khan-Huang-Liang (KHL) Model

Khan and Liang proposed the KHL model in 1999 [21], which also incorporates strain hardening, strain rate hardening and thermal softening effects. The relation is shown in Equation 2.22, where  $\varepsilon^p$  represents the true plastic strain,  $\dot{\varepsilon}^*$  is the dimensionless strain rate,  $T$ ,  $T_r$ ,  $T_m$  are the instantaneous, room and melting temperatures,  $D_0^p$  is equated to  $10^6$  s<sup>-1</sup> to make the strain rate non-dimensional, and  $A$ ,  $B$ ,  $n_0$ ,  $n_1$ ,  $C$  and  $m$  are material constants.

$$\sigma = \left[ A + B \varepsilon_p^{n_0} \left( 1 - \frac{\ln \dot{\varepsilon}}{\ln D_0^p} \right)^{n_1} \right] [\dot{\varepsilon}^*]^C \left[ \frac{T_m - T}{T_m - T_r} \right]^m \quad (2.22)$$

### 2.4 Transformation Induced Plasticity (TRIP)

TRIP steels are a family of steel grades that belongs to the first generation of AHSS. An illustration of elongation versus strength of different grades of steels can be found in Figure 5. A TRIP steel comes with at least three, and typically four, phases in the microstructure: a ferrite matrix, some bainite, retained austenite and hard martensite islands. The microstructure of a TRIP steel contains at least 5% retained austenite [22]. The TRIP780 material investigated in this study is provided by Arcelormittal Dofasco, and the material data is taken from the Automotive Partnership of Canada Project Database [23]. The chemical compositions of the material are shown in Table 1, and the as-received mechanical properties of the material are shown in Table 2.

C	Mn	P	S	Si	Al	Cu
0.21	1.74	0.01	0.002	0.05	0.49	<.02
Ni	Cr	Sn	Mo	V	Nb	Ti
<.02	0.2	<.02	<.02	<0.008	0.015	0.003
B	Ca	N	W	Sb		
0.0002	n/a	0.0022	n/a	n/a		

Table 1 – TRIP780 Chemical Composition

Grade	Heat	Coating Type	Coating Weight	Gauge	Dir.
TRIP T780	219813	galvannealed	43 g/m2	1.5 mm min.	T
Yield .2%	UTS MPa	%UEL	% elong.	n 10-20%	
462	855	17.2	22	0.19	

Table 2 – TRIP780 As-received Material Properties

### 2.4.1 TRIP Material Properties from a Microscopic Aspect

Figure 6 [24] presents a schematic of the microstructure of TRIP steels. Just as in dual phase (DP) steels, the dispersion of hard bainite/martensite phases in the soft ferrite creates a high work hardening rate and high formability. The high work hardening mechanism is achieved by the motion of dislocations being hindered by the hard phases. The high ductility is the result of the soft ferrite phase absorbing the strains around the grain boundaries. Moreover, the retained austenite phase progressively transforms into martensite, which typically results in a slightly lower initial work hardening rate, and a substantially higher work hardening rate at higher strain levels, when compared to a DP steel grade of about the same yield and/or ultimate strength.

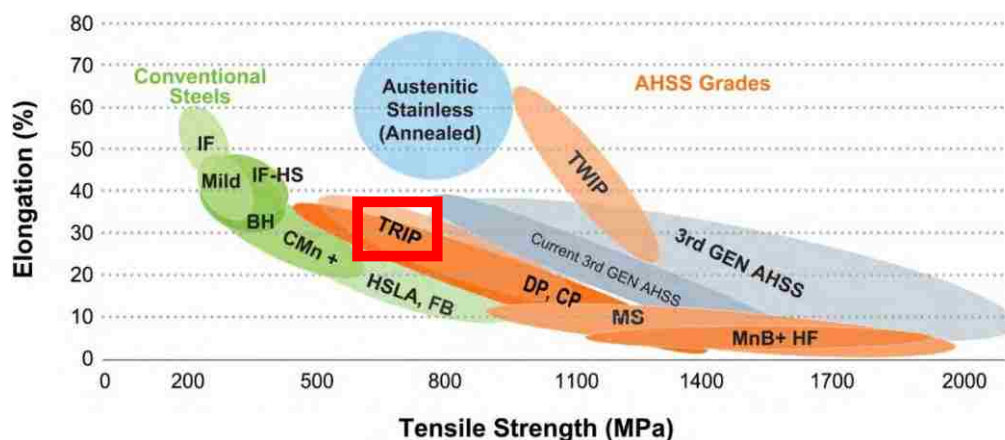


Figure 5 – Relationship between ductility and strength for various grades of steel [24]

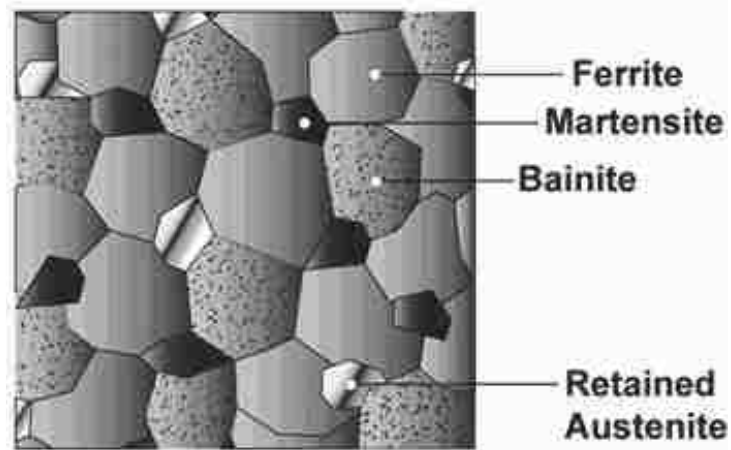


Figure 6 – Schematic representation of the microstructure of TRIP steels [24]

What differentiates TRIP steel from any other AHSS is the high percentage of retained austenite, which is integral to the transformation induced plasticity effect of the material. The added contents, such as silicon and aluminum, accelerate the formation of ferrite and bainite during cooling, and suppress the formation of cementite. The relatively high carbon content also contributes to the stability of the austenite. It is well known that a martensitic transformation occurs when quenching an iron-carbon mixture from the austenitic phase. This causes the austenite, with the face centered cubic (FCC) structure, to transform into martensite, with body centered cubic/tetragonal (BCC/BCT). The process involves some shearing and/or twinning, and is diffusion-less, since diffusion cannot happen when the austenite is being cooled so rapidly [25]. The martensitic transformation in TRIP steels also involves shearing, with the only difference being that the shearing is not a result of the atoms in the lattice moving for an equilibrium state (like in the quenching process), but rather a result of induced strain on a macro scale, which is typically found in all deformation modes in metal forming processes, from drawing to stretching. A simple illustration of the FCC to BCC/BCT transformation in the crystal structure is shown in Figure 7. While the simple tensile and compression distortion originally proposed by Bain [26] may be unrealistic, an equivalent BCT structure can be

obtained from an FCC structure with some more complicated three-dimensional shearing, as well as slip/twinning to allow for stress reduction [25].

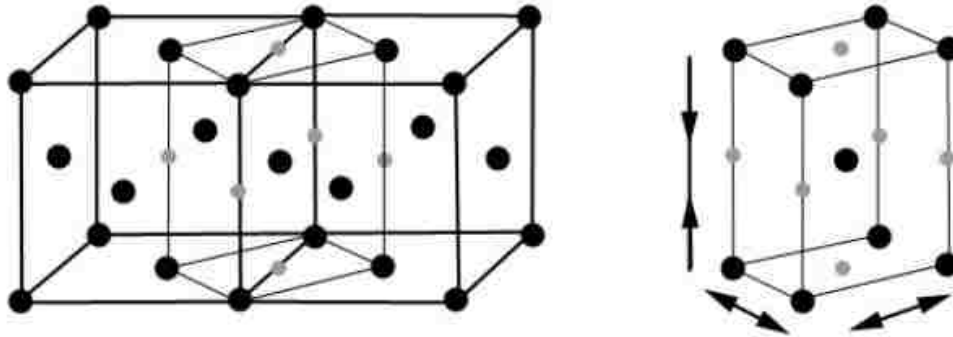


Figure 7 – FCC to BCC/BCT lattice transformation [25]

#### 2.4.2 Processing and Application of TRIP Steels

TRIP steels have excellent mechanical properties in terms of formability, strain energy absorption, fatigue endurance limit, and durability. Another advantage of this grade of steel is the bake hardening effect, where the strength of the material increases when it is heated in a paint oven at about 170 °C after a pre-strain has been applied [24]. The boost in work hardening rate from the martensitic transformation can be tailored to a desired strain level by controlling the carbon content. As the carbon content increases, there is an increase in the strain level required to activate the martensitic transformation. This increases the potential of the TRIP material for applications in crash energy absorption components, where the designer can utilize the transformation induced plasticity to achieve high energy absorption before failure.

The current limitations of the TRIP steel grades include poor edge-stretchability and poor spot-welding behaviour. These drawbacks can generally be addressed and compensated with design or process controls. Aside from the commonly accepted material properties,

the edge-stretchability of a sheet material usually depends on the quality of the edge resulting from the blanking/shearing process. Edge-stretchability can usually be improved by changing the clearance on the blanking/shearing tools, or using an alternative cutting method such as laser trimming or water jet cutting. Another common work-around is to design the formed part with material in excess, and trim the part afterwards.

## **2.5 Digital Image Correlation (DIC)**

Digital Image Correlation (DIC) is a non-contact method for measuring motion, deformation and strains through digitally recorded images. While the earliest development in image correlation dates back to 1950 [27], DIC systems are becoming more popular due to their portability, high resolution, improving reliability, experimental efficiency improvement and cost reduction. DIC systems can be used in any kind of environment if the cameras can be installed to view the surface of the object being studied, and a speckle pattern can be applied to the surface of the specimen. When used in conjunction with a forming process, digital cameras record images throughout the entire process of deformation. Then the DIC software compares each digital image of the test specimen throughout the time history with an image of the undeformed specimen. The area of interest (AOI) in each image, with an applied speckle pattern, is divided into subsets of pixels. The size of the subsets depends on the size of the individual dots that makes up the speckle pattern. Subsets usually overlap to provide a good measurement resolution, while the distance between the subsets are controlled by step-size. The locations of these subsets are tracked throughout the time history, while the surrounding pixels in each subset help recognize the subset as a unique unit in the image. The displacement of the subsets are used to produce a vector field, and further derived into a deformation field. To obtain strain, the change in distance between center locations of different subsets are calculated. DIC systems provide much more information than conventional strain measurement methods, as the material deformation and/or strain information during the entire testing period is recorded at a prescribed rate (usually

around 10Hz for quasi-static metal forming applications). Since the image acquisition, data treatment and calculations are done with a high level of automation, this strain measurement method is very efficient. As implied by Melorose et al. [28], the current state of commercially available image matching/comparing algorithms are equipped with a large number of features to adapt and compensate for circumstances such as low or changing light, slight motion of the camera systems and thick lens or other optical distortions etc., and have been thoroughly analyzed for error progression. These established algorithms are suitable for academic research and industrial applications when used with caution.

For formability tests, DIC system makes it possible to conduct strain path analysis, and to more accurately identify the onset of necking. If the specimen does not undergo necking prior to fracture, due to its limited post-uniform elongation, DIC is still able to capture the strain state just prior to fracture, which is not possible with the conventional method. The major challenge with the use of DIC in formability tests is to develop a generally applicable criterion to identify the onset of necking.

The processing and transformation of geometric data of the studied object in a three-dimensional DIC stereo rig can be conveniently modeled as one rigid transformation and two perspective projections. The two projections of an object from different angles of view produce two sets of two-dimensional geometric information. Since the perspective projections remove the three-dimensional information entirely, the distant and angular relation between the two cameras (from the rigid transformation) is required to recover any out-of-plane motion or deformation of the object. The relation between the cameras in the coordinate system can be determined with the stereo system calibration process, usually taken prior to a DIC measurement. The calibration relies on the epipolar constraint to recognize a two-dimensional pattern of dots with known distances between them. An illustration of the epipolar constraint can be found in Figure 8, where the camera optical centers are represented by  $C$  and  $C'$ , and the three-dimensional point  $M$  and its images  $m$  and  $m'$  lie in a common plane. This common plane intersects each image plane in an epipolar line. The epipolar constraint reduces the matching problem to

a single scan along the epipolar lines [28]. When the total transfer function for the rigid transformation and the two perspective projections are found, a backward derivation of the transfer function for converting the pairs of two-dimensional points back to the three-dimensional points on the object can be performed; the stereo rig is then able to reproduce a three-dimensional model that exactly resembles the available surface geometry of the object, from the pair of two-dimensional images taken by the cameras. A schematic of the stereovision DIC system can be found in Figure 9.

The accuracy of results obtained using DIC techniques depends on many factors, including the resolution and configuration of the cameras used, the quality of the light source, the accuracy of calibration, the quality of the speckle pattern, and the conditions in the surrounding environment.

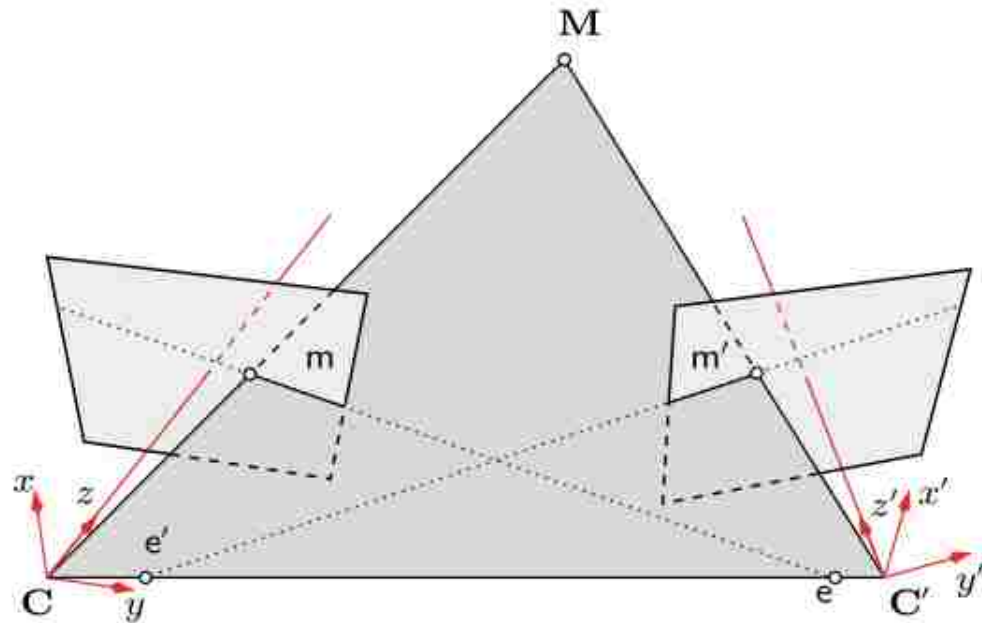


Figure 8 – Illustration of the epipolar constraint in DIC [29]

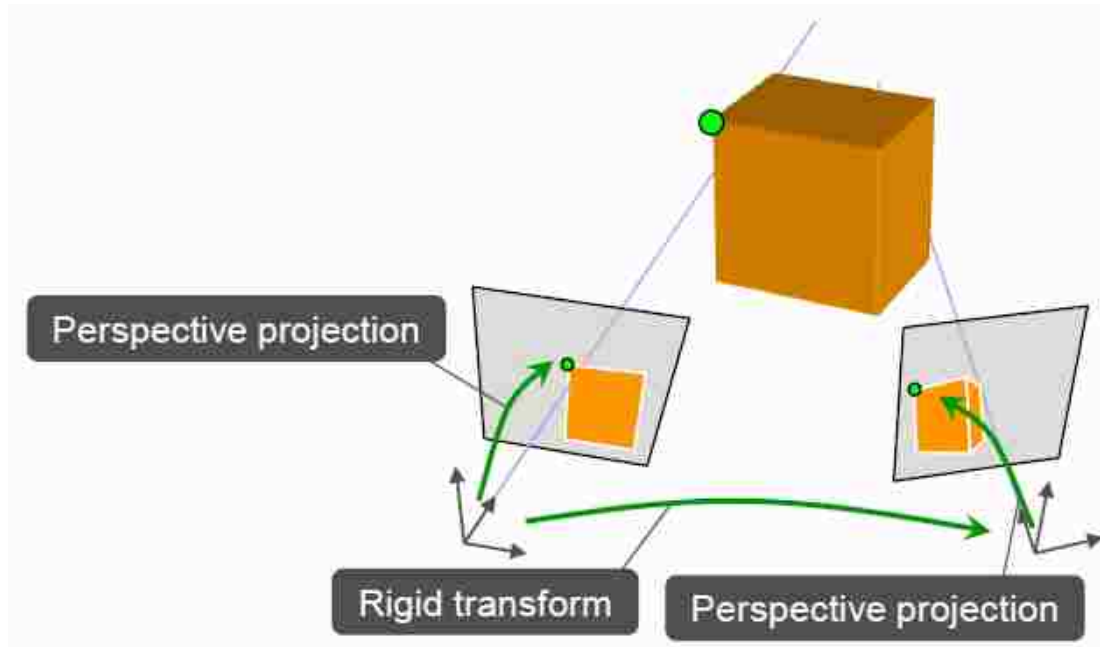


Figure 9 – Schematic of the stereo vision DIC system [29]

## 2.6 Forming Limit and Formability Tests

### 2.6.1 Experimental determination of FLC

The early development of formability tests and the forming limit diagram (FLD) dates back to the early work of Keeler et al. [4]. A forming limit curve (FLC) is a plot in a major strain versus minor strain coordinate system of the lowest threshold strain states beyond which there is a risk of necking. One simple way to graphically interpret an FLC is that, with a confidence zone in mind, all strain states below the curve are safe conditions for forming, while those above the curve will likely result in material necking or splitting. An FLD may also contain another dimension such as strain rate or temperature, and shows how the FLC changes as a function of the process parameter. The FLC has become a widely used graphical representation of the limiting strain for different strain ratios/paths for sheet metals.



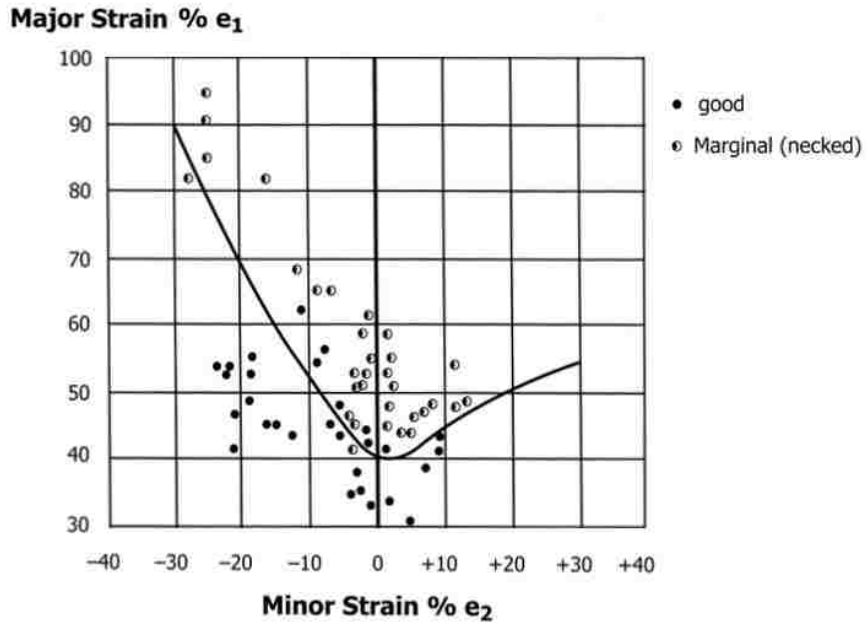


Figure 10 – Example of an FLC [30]

The experimental data used to create the FLC is collected from formability tests where sheet metal specimens are deformed along different strain paths, usually controlled by specimen geometry, up to the onset of necking. The strain states at and near the incipient neck on all test specimens are recorded, and individual strain states are identified as safe, marginal (necked), or failed, based on severity of necking. A typical FLC is shown in Figure 10, with the solid circles representing safe strain states, and the half full circles representing necked strain states.

## 2.6.2 Formability Tests

### 2.6.2.1 Nakazima Test

The Nakazima test is one of the most common ways of testing metal sheets to determine their forming limits [31]. A sheet specimen is clamped between the upper and lower dies

and locked around its periphery to prevent any material from drawing into the die cavity. During the test, the hemispherical punch slowly stretch-forms the specimen into a dome shape. The top side of the specimen is usually marked with a pattern for strain measurement. The upper die features a profile radius to prevent premature fracture due to stress concentration. A schematic of the Nakazima test is shown in Figure 11.

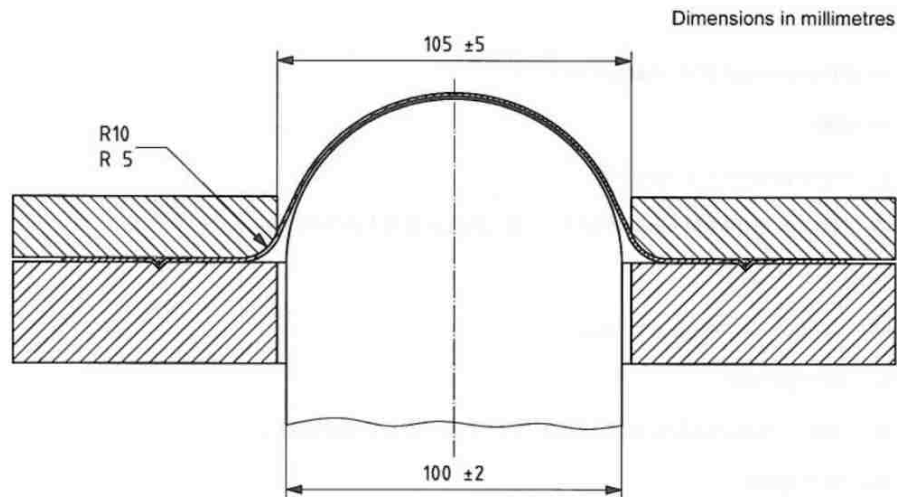


Figure 11 – Schematic of the Nakazima test [32]

The Nakazima test is a simple experiment and the selection of an appropriate lubricant allows the friction between the punch and the specimen to be controlled. The disadvantages of this test are that the hemispherical punch contacts the specimen directly and induces friction, as well as through-thickness and bending stresses in the area of interest. The resulting strain path can therefore be non-linear, and the strains will vary through the sheet thickness. Ming et al. [33] proposed a correction procedure for the strain data measured from Nakazima tests.

### 2.6.2.2 Marciniak Test

As shown in Figure 12, the Marciniak test [34] uses a flat punch with a profile radius. The Marciniak test also requires a “carrier blank” to carry the test specimen over the punch profile radius, and thus prevent it from splitting. A highly formable sheet material with excellent edge stretchability is required for the carrier blanks, with a circular hole in their center. The presence of the carrier blank creates an area free of bending, friction, or through-thickness stress on the test specimen. Lubrication is applied between the carrier blank and the punch to reduce friction. The Marciniak test generates an ideal plane stress condition in the gauge area.

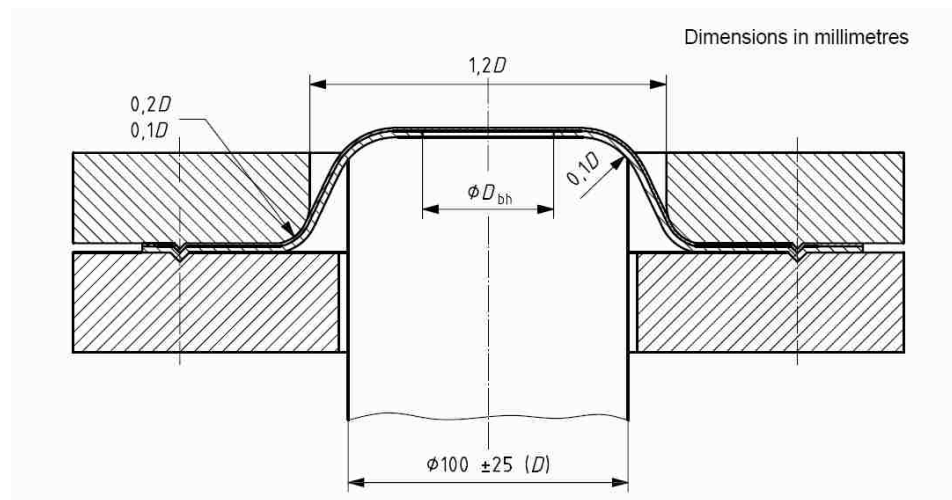


Figure 12 – Schematic of the Marciniak test [32]

### 2.6.3 Measuring Strain and Identifying the Onset of Necking

#### 2.6.3.1 The Traditional North American Method

The ASTM standardized North American method for determining FLC uses a grid-measurement method to obtain the plastic strains on the surface of tested specimens using pre-etched square or circular grids [30]. The Keeler method [4] of determining the forming limit of a sheet material requires that the test be stopped right at the onset of

necking, which can be difficult to achieve in certain circumstances. The strains measured with the grid pattern have limited accuracy due to the size of the grid and the thickness of the electro-etched lines. Subjectivity also exists in the methods of identifying/detecting the neck: a neck can be detected through visual inspection of the specimen's surface appearance and by feeling the specimen with one's fingertip. Moreover, an incipient neck may lie more or less within a particular square or circular grid, which makes it difficult to determine whether the strain data for this grid should be identified as necked, partially necked or questionable. Finally, some material-geometry combinations do not exhibit necking before fracture, making this method ineffective.

### **2.6.3.2 The Bragard Method**

A different approach consists of taking the specimen right to failure (both necking and fracture are acceptable), and interpolating the strain state of the forming limit at the location of failure from a quadratic function fitted from the major strain versus major length data, as described by Bragard [35]. This method is specified in the ISO12004-2 standard for experimental determination of FLC [32]. This method allows the determination of the forming limit even for materials that do not exhibit necking before fracture. Moreover, this post-processing of strain data can be used in conjunction with DIC strain measurements. Furthermore, it is also less subjective as the onset of necking is not judged from the appearance of the specimen surface. Nevertheless, the uncertainty of the method comes from the ambiguous definition of failure and the assumption of a quadratic function fitting the strain distribution. Some FLCs produced with this method are questionable and inconsistent with experimental data from other methods. Examples are shown in Figure 1 and Figure 13.

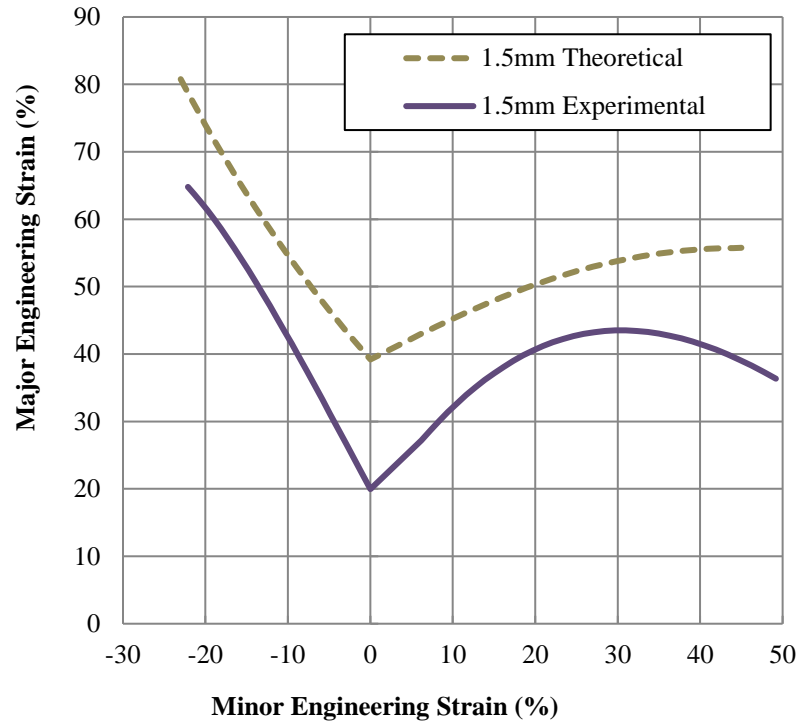


Figure 13 – FLC of 1.5mm DP600 sheet generated from DIC data [23]

### 2.6.3.3 DIC Analysis Methods

In recent years, DIC has been extensively used in conjunction with various data analysis techniques to determine the onset of localized necking within the time domain of the formability test. This section provides a review of some of the more important criteria that have been proposed for identifying the onset of necking, with their benefits and limitations.

#### The Surface Slope Criterion

The surface slope criterion, sometimes referred to as the flat-valley method in some literature [36], takes advantage of DIC data with high resolution in both space and time

domain. This is a geometry-based criterion that detects the onset of necking regardless of rate effects.

The onset of necking is the beginning of the localization of the thickness strain. The top surface of the specimen in the area close to the dome will exactly resemble the shape of the hemispherical punch (with an offset corresponding to the thickness of the sheet), if no localized thickness strain is present. The onset of necking can be identified when the contour of the top surface fails to resemble the shape of the punch.

As shown in Figure 14, this method determines the height contour (Z position vs X position) of a line that lies across the neck on the surface of the specimen throughout the time domain. The instance in time when the profile exhibits a flat portion at the top of the dome is taken as the onset of necking. The derivative  $dz/dx$  corresponding to the flat portion should show a constant zero value, as illustrated in Figure 15. This criterion was developed for the Nakazima test, but can also be adapted to the Marciniak test. A robust frequency low-pass digital differentiator is required for processing the position measurements obtained from the DIC data. Some changes are also required for accommodating imperfections in experiments, such as the occurrence of a neck that is not located on top of the dome.

### The Strain Rate Departure Criterion

As investigated by Zhang et al. [37] and Martinez-Donaire et al. [36], the onset of necking can be identified with a change in strain rate for an “element” outside the neck affected area. Since the localization of the strain happens in a narrow band in proximity to the final neck, the material outside of this band will exhibit a gradual decrease in strain rate. The suggested threshold to take is when the strain rate for an “element” outside the necking area reaches its maximum. A frequency low-pass differentiator is also required. An illustration of this criterion is shown in Figure 16.

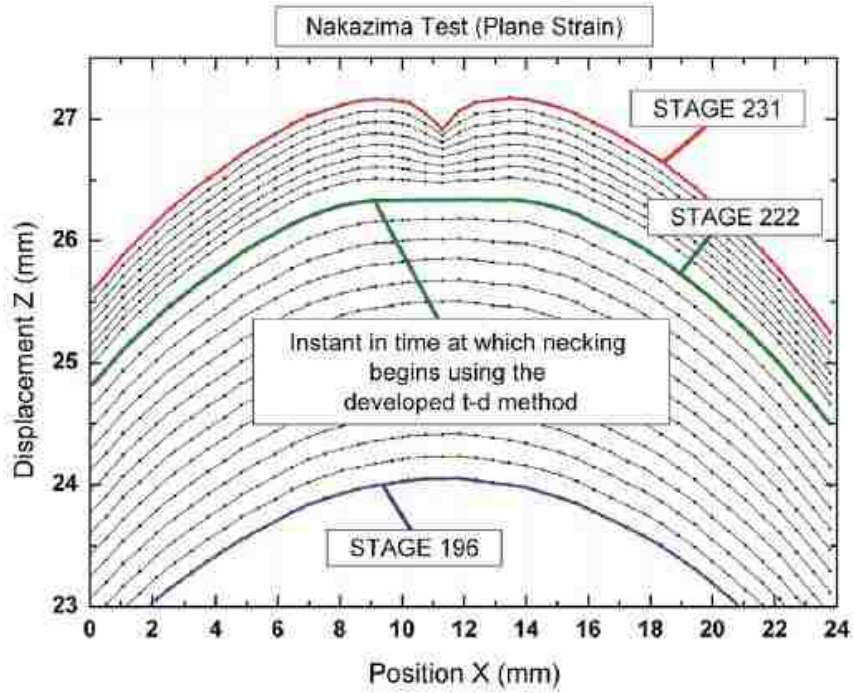


Figure 14 – Example of 2D contours of the top surface geometry of a plane strain Nakazima specimen [36]

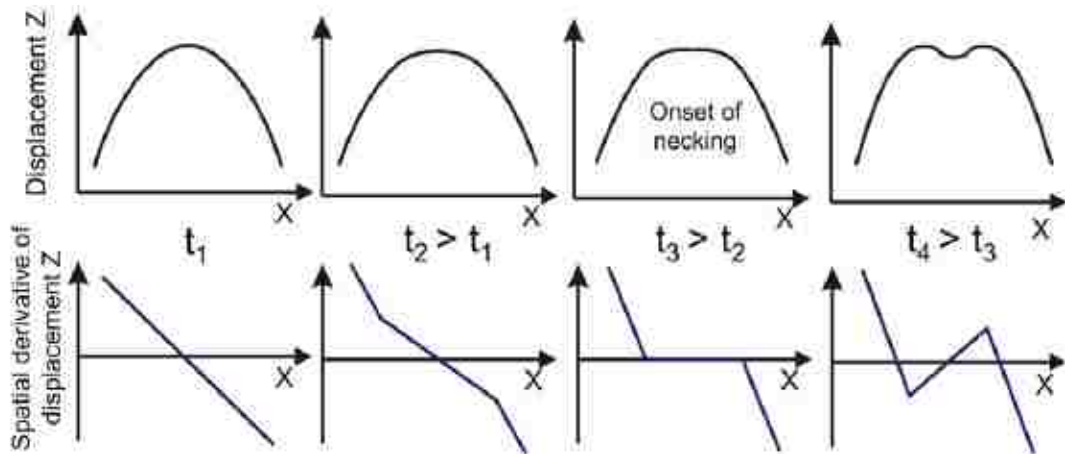


Figure 15 – Description of the surface slope criterion [36]

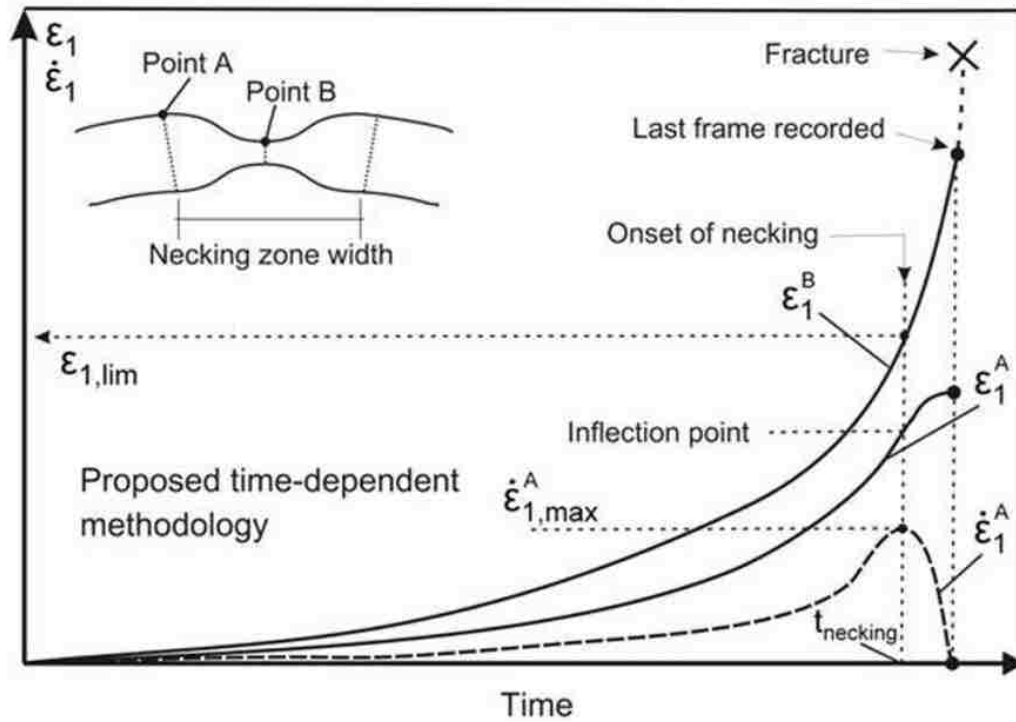


Figure 16 – Illustration of the strain rate departure criterion [36]

### The Surface Height Difference Criterion

Wang et al. [38] proposed the surface height difference criterion which is best suited to the Marciniak test. Two points are taken on a Marciniak specimen, with one in the neck, and the other outside the necking zone. The difference in height (Z position) is measured by the DIC within the time domain. As shown in Figure 17, the onset of necking is identified when the difference in the Z-position of the points starts to rapidly increase.

Since the height difference of different surface points in a Nakazima test continuously change throughout the time history, even without necking, this method is not readily applicable to the Nakazima test.



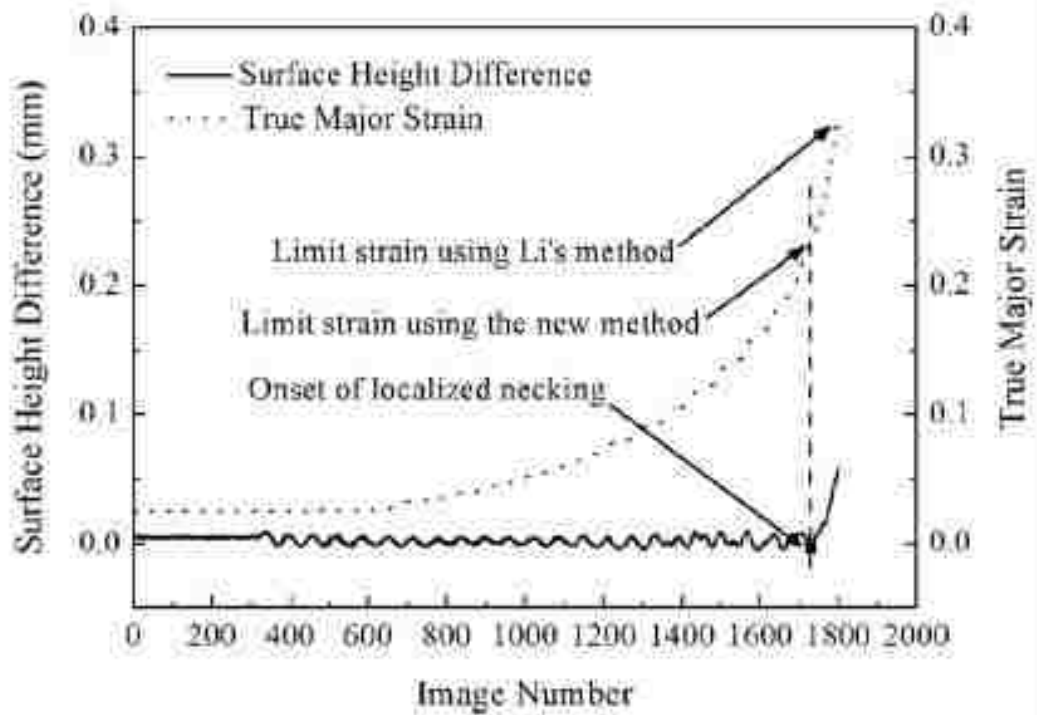
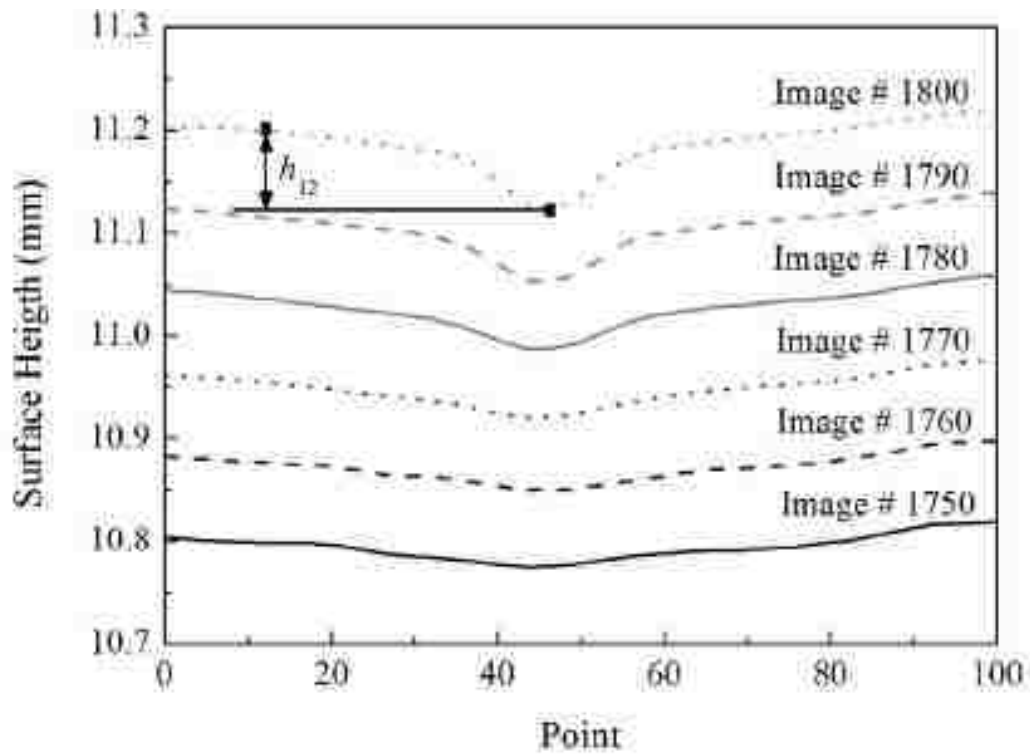


Figure 17 – Description of the surface height difference criterion [38]

### The Strain Gradient Increment Criterion

As proposed by Zhang et al. [37], the strain gradient increment criterion identifies the onset of necking as the location where a strain gradient of 0.005 first occurs, which would be state (b) for the example shown in Figure 18. This criterion is not commonly used; thus, the reliability of this method requires further validation.

### The Transition of Incremental Strain Path Criterion

The transition of strain path criterion is based on the theory that the strain path switches to plane strain when the width strain rate goes to zero at the onset of necking [39]. As shown in Figure 19, “Element B” inside the necking zone has a width strain trending towards zero, while “Element A” outside the necking zone has its major strain trending towards zero (i.e. the strain ratio  $\Delta\varepsilon_{11}/\Delta\varepsilon_{22}$  tends to minus infinity). This method is quite similar to the strain rate departure criterion but has a more exaggerated trend. The plotted incremental strain ratio for both elements represents the ratio of the minor strain to the major strain.

### The 2<sup>nd</sup> Derivative of Thickness Strain Criterion

As investigated in Zhang et al. [39], the 2<sup>nd</sup> derivative of thickness strain criterion assumes a drastic change in thickness strain in the necking zone at the onset of necking, and seeks for the instance of highest “strain acceleration”. As shown in Figure 20(b), the onset of necking is identified as  $t_2$ , where the magnitude of the thickness strain acceleration is at a maximum. This method is based entirely on thickness strain, which can be a challenge to accurately estimate from DIC data. The two-time differentiation of experimental thickness strain data also requires a robust frequency low-pass digital differentiator. This method may be more suitable for FEA analysis.

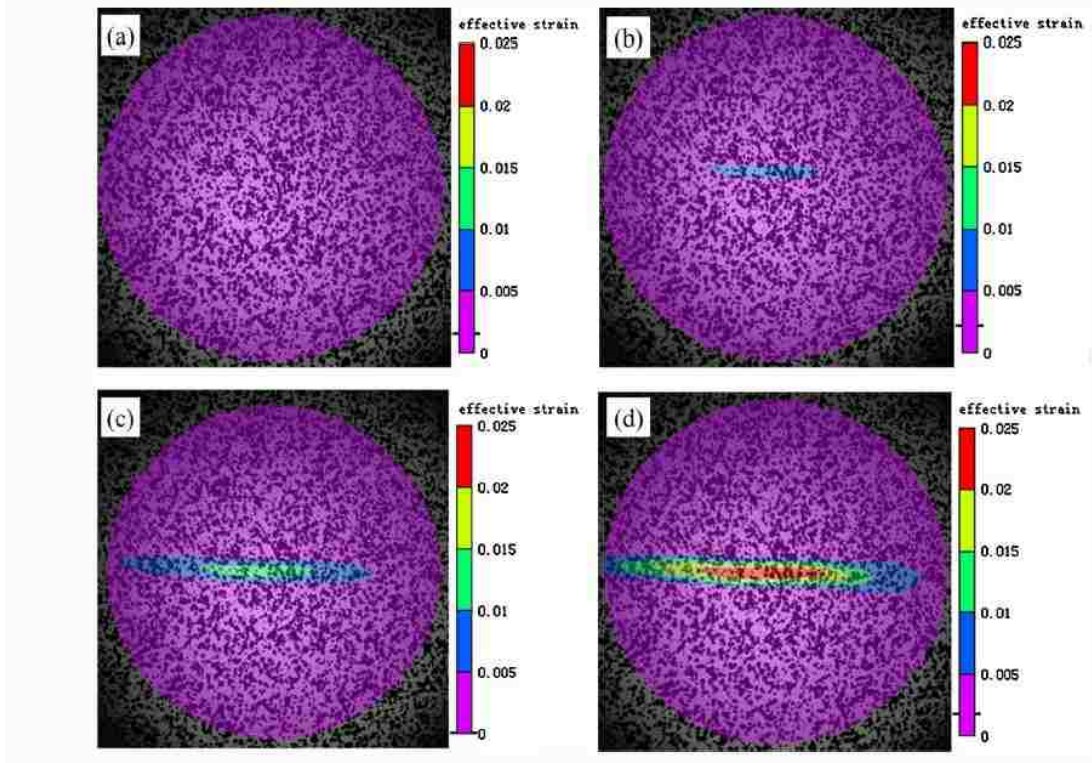


Figure 18 – Illustration of the strain gradient increment criterion [37]

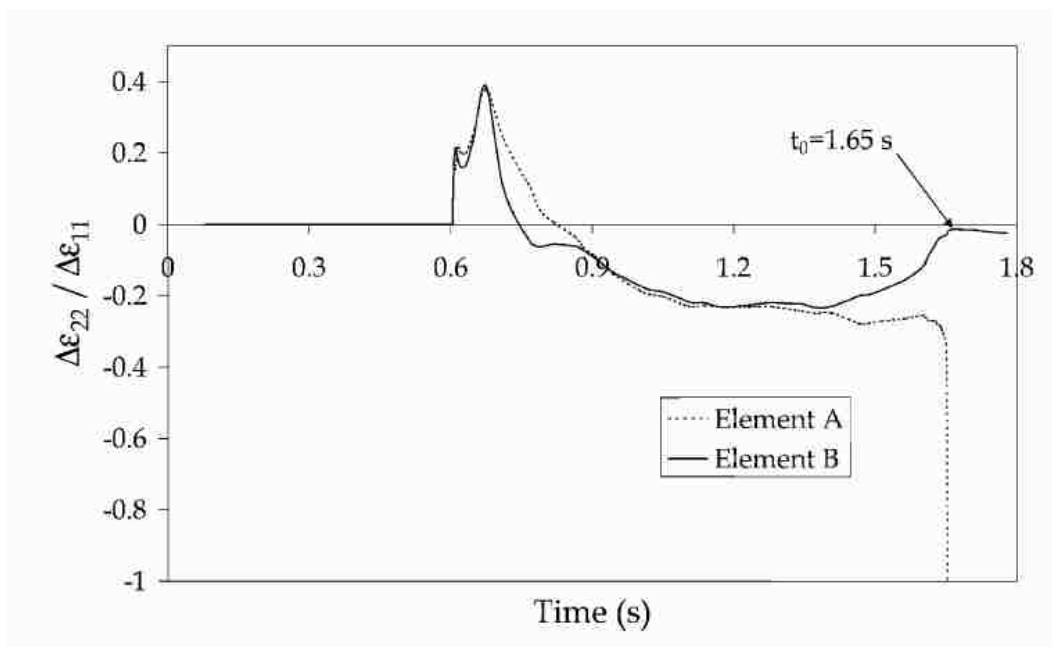
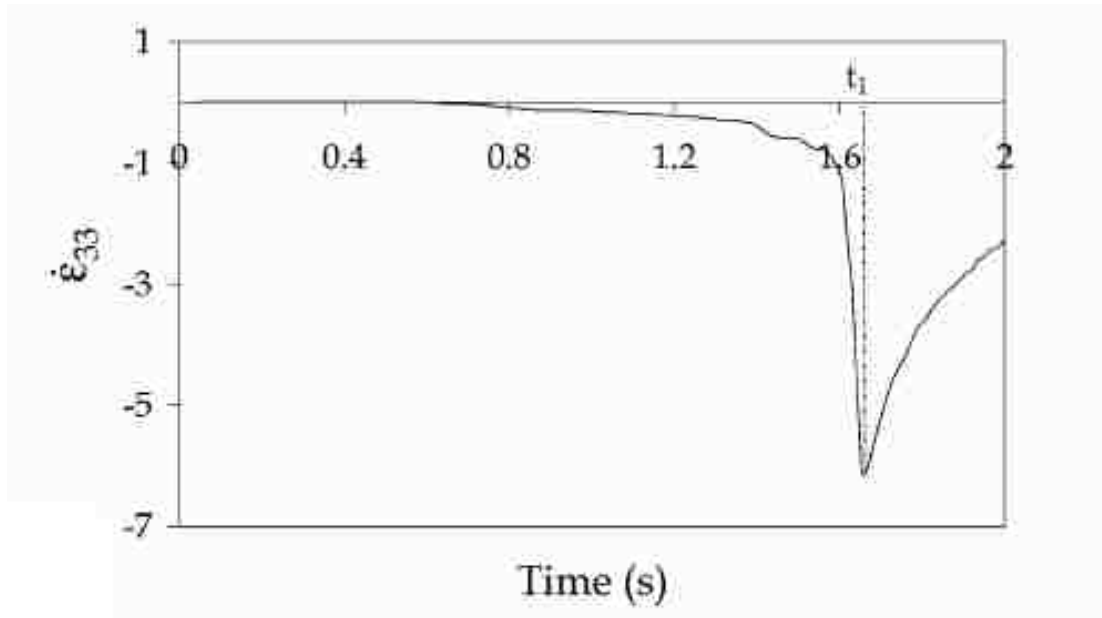
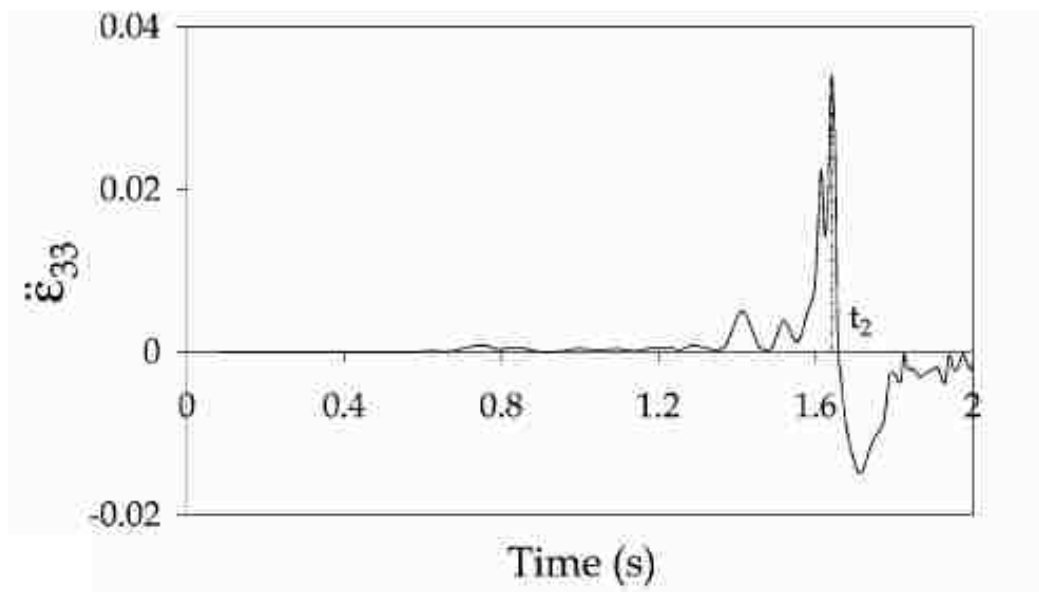


Figure 19 – Illustration of the transition of incremental strain path criterion [39].



a)



b)

Figure 20 – Example of the 2<sup>nd</sup> derivative of thickness strain criterion [39]

### The Maximum Load Criterion

A load-based criterion where the maximum load is determined from the incremental load was proposed by Savic et al. [40]. As shown in Figure 21, the incremental load is plotted against the displacement of the punch. The onset of necking is identified when the incremental load switches from positive to negative, indicating that the test is beyond uniform strain.

The proposed maximum load criterion has been applied to a uniaxial tensile test (Figure 21), rather than a formability test. The more complicated stress and strain state in the formability test may introduce inaccuracy to the results obtained by this method. In a Marciniak test, the extra load induced by the punch interacting with the carrier blank would need to be considered.

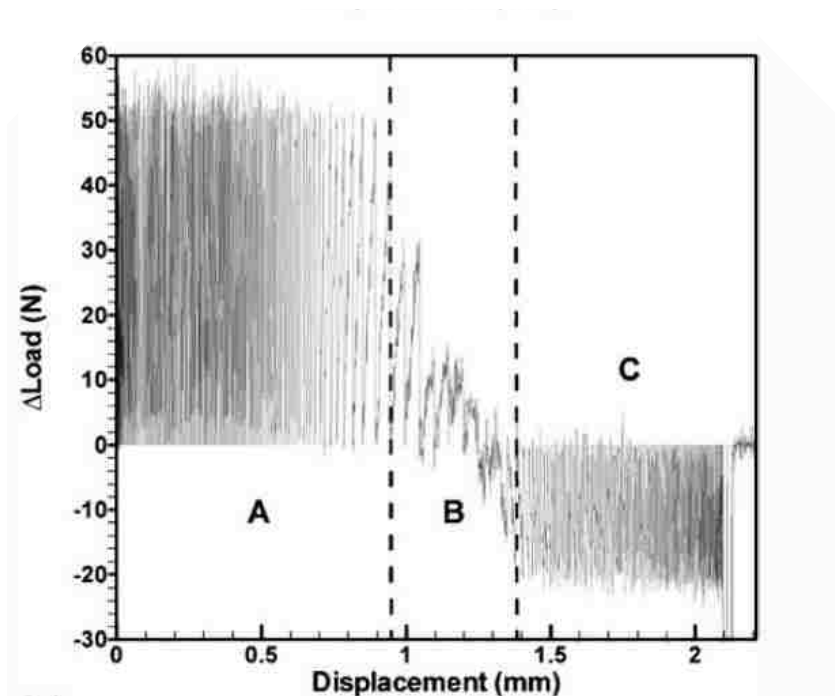


Figure 21 – Illustration of the maximum load criterion applied to uniaxial tension test data [40]

#### 2.6.4 Compensation for Process-Dependent Effects in Nakazima Tests

The Nakazima test is known to produce an inaccurate forming limit due to the effect of curvature, the nonlinear strain path (NLSP), and the contact pressure between the punch and the blank [33].

The curvature effect is induced by the hemispherical punch, creating a bending condition where the outer layer of the blank will be subject to more tension than the inner layer that is in contact with the punch. As the localized through-thickness necking requires every layer of the material to exceed the limiting strain [41][42], the inner layer with the lowest strain is most likely the critical layer. The strains for the middle and inner layer can be calculated from Equation 2.18a and 2.18b, where  $i$  represents the major and minor direction,  $j$  represents the time,  $\kappa$  and  $t$  are the curvature of the geometry and thickness at the necking location.

$$\varepsilon_{i,j}^M = \varepsilon_{i,j}^O + \ln(1 - t_j \cdot \kappa_{i,j}^O/2) \quad \text{for } i = 1, 2, j = (1, N) \quad (2.18a)$$

$$\varepsilon_{i,j}^I = \varepsilon_{i,j}^O + \ln(1 - t_j \cdot \kappa_{i,j}^O) \quad \text{for } i = 1, 2, j = (1, N) \quad (2.18b)$$

The Nakazima test inevitably leads to NLSP due to a series of factors such as friction, punch geometry and contact stress. A strain-based FLC is created from experimental data that assume linear major – minor strain history from zero strain all the way to failure strain for each strain path; hence strain data collected from Nakazima tests do not accurately represent the forming limits of the material. Since the behaviour of the material is strain-path dependent rather than strain-state dependent, and since the direct cause of damage and failure in materials is dependent on stress, a stress-based FLC, or forming limit stress diagram (FLSD) has been proposed by multiple scholars to replace the traditional strain-based FLC. The FLSD approach requires stress data from the entire loading history. Since it is difficult to obtain a direct measure of the stress distribution, high resolution strain distribution from DIC measurement within the entire time span of the test is required in combination with a yield and hardening model to derive the history of stress states. Equation 2.19 can be used to calculate the limiting stress states, where  $\sigma_y$

can be expressed with Equation 2.20a), with the principal stresses,  $\sigma_1$  and  $\sigma_2$ , replaced with  $\alpha$ , the stress ratio, as shown in the modified Equation 2.20b). The flow stress,  $\sigma_Y$ , can be expressed with the power law hardening function and the flow strain,  $\bar{\epsilon}_p^X$ , can be expressed with Equation 2.12, where  $X$  represents the inner, middle and outer layers. It is worth noting that the through-thickness stresses are eliminated for a plane-stress condition, before contact pressure is compensated for.

$$\begin{pmatrix} \sigma_1^X \\ \sigma_2^X \end{pmatrix} = \begin{pmatrix} 1 \\ \alpha^X \end{pmatrix} \frac{\sigma_Y(\bar{\epsilon}_p^X)}{\bar{\sigma}_y(1, \alpha^X)} \quad (2.19)$$

$$\bar{\sigma}_y(\sigma_1, \sigma_2) = \sqrt{\sigma_1^2 + \sigma_2^2 - \frac{2\bar{R}}{1+\bar{R}}\sigma_1\sigma_2} \quad (2.20a)$$

$$\bar{\sigma}_y(1, \alpha) = \sqrt{1 + \alpha^2 - \frac{2\bar{R}}{1+\bar{R}}\alpha} \quad (2.20b)$$

The contact pressure between the hemispherical punch and the metal blank voids the plane stress assumption. When the material is loaded with a through-thickness stress, the increased stress triaxiality tends to suppress the occurrence of voids and the necking of the material. The contact pressure can be compensated with Equation 2.21a) and 2.21b), where  $P$  is expressed in Equation 2.22,  $t$  is the sheet thickness and  $\kappa=50.8^{-1}\text{mm}^{-1}$  in a standard Nakazima test.

$$\begin{pmatrix} \sigma_1^M \\ \sigma_2^M \end{pmatrix} = \begin{pmatrix} 1 \\ \alpha^M \end{pmatrix} \frac{\sigma_Y(\bar{\epsilon}_p^M)}{\bar{\sigma}_y(1, \alpha^M)} - \frac{P}{2} \begin{pmatrix} 1 \\ 1 \end{pmatrix} \quad (2.21a)$$

$$\begin{pmatrix} \sigma_1^I \\ \sigma_2^I \end{pmatrix} = \begin{pmatrix} 1 \\ \alpha^I \end{pmatrix} \frac{\sigma_Y(\bar{\epsilon}_p^I)}{\bar{\sigma}_y(1, \alpha^I)} - P \begin{pmatrix} 1 \\ 1 \end{pmatrix} \quad (2.21b)$$

$$P = t\kappa^I(1 + 0.5t\kappa^I)(\sigma_1 + \sigma_2) \quad (2.22)$$

Finally, the forming limit strain states can be calculated from the forming limit stress states using Equation 2.23, where the strain ratio  $\beta$  can be expressed in terms of the stress ratio  $\alpha$  as shown in Equation 2.24.

$$\begin{pmatrix} p_1 \\ p_2 \end{pmatrix} = \begin{pmatrix} 1 \\ \beta \end{pmatrix} \frac{\bar{\epsilon}_p^X}{\dot{\bar{\epsilon}}_p(1,\beta)} \quad (2.23)$$

$$\beta = \frac{(1+\bar{R})\alpha - \bar{R}}{1+\bar{R} - \alpha\bar{R}} \quad (2.24)$$

## 2.7 Summary of Literature Review

The two existing standardized methods for determining FLC have their pros and cons. The Keeler method is subjective due to the tactile and visual detection of onset of necking, while the Bragard method calculates the failure strain with a quadratic fit, instead of experimentally identifying the localized necking. It is obvious that more advanced criteria for identifying the onset of necking are needed to produce an accurate and robust FLC. DIC online strain measurement provides high resolution strain data for the deformation field and in full-time history, while the traditional grid measurement gives lower resolution strain data at one point in time (when the test is stopped at the onset of necking). However, both standardized methods do not require the implementation of online DIC. Thus, to improve upon the standardized methods, experiments and strain analysis with different necking criteria based on DIC strain data should be investigated.



### **3. Research Methodology**

The general methodology for this study consists of a series of mechanical tests – which include tensile tests after rolling induced pre-strain and simple shear tests – performed on the TRIP780 sheet metal to obtain the work hardening behaviour of the material. Finite Element (FE) simulations of the Nakazima formability tests were also conducted using the material properties obtained from the mechanical characterization tests in order to optimize the geometry of the Nakazima specimens for different strain paths. Simulations were then followed by experimental formability tests and surface strains were measured with both grid analysis and DIC method; and the experiments were used to validate the simulations. Post-processing of the formability test results led to the determination of an FLC. The differences in results from different necking criteria were analyzed, and a robust criterion was selected.

#### **3.1 Uniaxial Tensile Tests Combined with Incremental Rolling**

The purpose of the tensile tests with various pre-strains induced by flat rolling was to obtain the work hardening behaviour of the material well beyond the uniform elongation of conventional uniaxial tensile tests. Sheet metal strips were electro-etched with a 2.54-mm (0.1-inch) grid pattern. The strips were then rolled to different levels of plastic strain. The effective plastic pre-strain was obtained by measuring grid deformation and thickness after rolling. ASTM E8 tensile specimens were machined from the rolled strips with wire electric-discharge machining (EDM). A speckle pattern was applied to tensile specimens with spray paint for image-based strain measurements. Tensile tests were performed using an MTS Model 43 Universal testing machine with a 50kN loading capacity. A 25mm gauge mechanical extensometer as well as a video extensometer and 2D DIC post-processing tools were used for strain measurements. The data from the MTS machine and the DIC system were combined and synchronized in a custom MATLAB code for further post processing and analysis. The true stress - true plastic strain flow curve was obtained over a wide strain range, as well as Lankford coefficients in different

loading directions. Figure 22 shows the etched and etched-rolled strips, as well as an EDM cut ASTM E8 specimen with speckle pattern applied. Tensile specimens were tested in three material orientations, the rolling, transverse and diagonal directions, to characterize the planar anisotropy of the material. Specimens at different rolling induced pre-strains were tested in the rolling and transverse direction, while only the unrolled specimens were tested in the diagonal direction. All test conditions were repeated three times. More images of the testing are included in Appendix A.

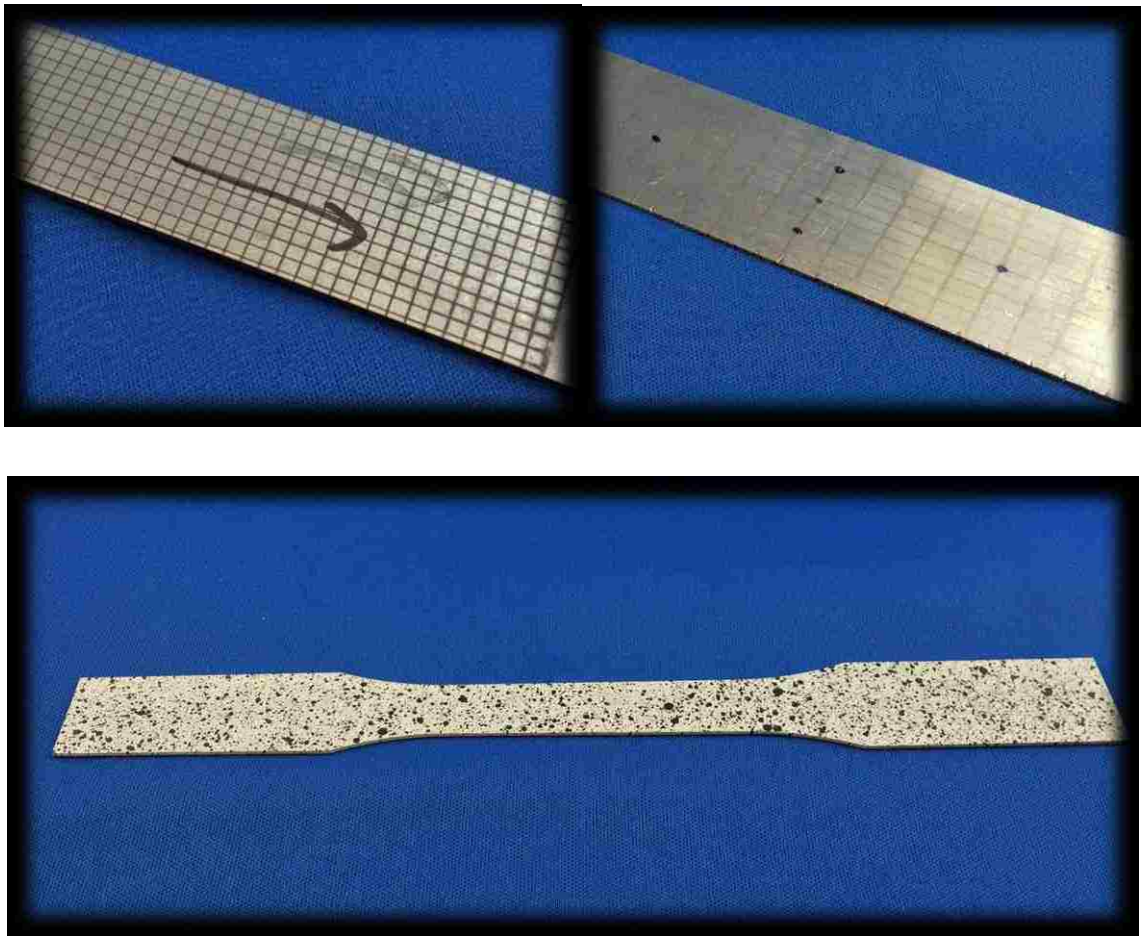


Figure 22 – Preparation of tensile specimen

### 3.2 Shear Tests

The purpose of the shear tests was to determine the work hardening behaviour of the TRIP780 sheet material with a different loading history and strain path up to a higher strain level than that which can be achieved in a tensile test. The specimen geometry and testing fixture shown in Figure 23 and Figure 24 were designed by Sarker [14], for the purpose of cyclic shear testing. Speckle patterns were applied to the gauge areas of the specimens for strain measurements. Shear tests were performed on the same testing apparatus as the tensile tests with a custom fixture adapted to the crosshead of the MTS machine for loading.

It is important to note that both stress and strain states in the shear test history must be converted into effective scalar values to obtain an equivalent stress – strain flow curve that can be compared with the tensile flow curve. This conversion was carried out assuming Hill's 1948 anisotropic yield criterion. Work hardening behaviour data obtained from shear tests were then compared with data from tensile tests coupled with incremental rolling.

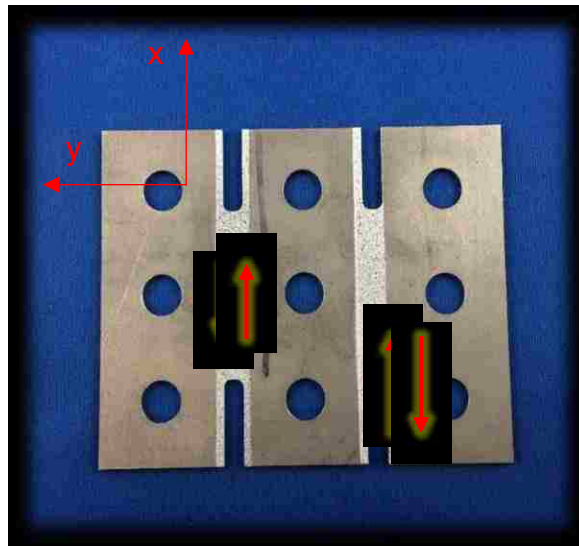


Figure 23 – Shear test specimen with speckle pattern in the two gauge areas

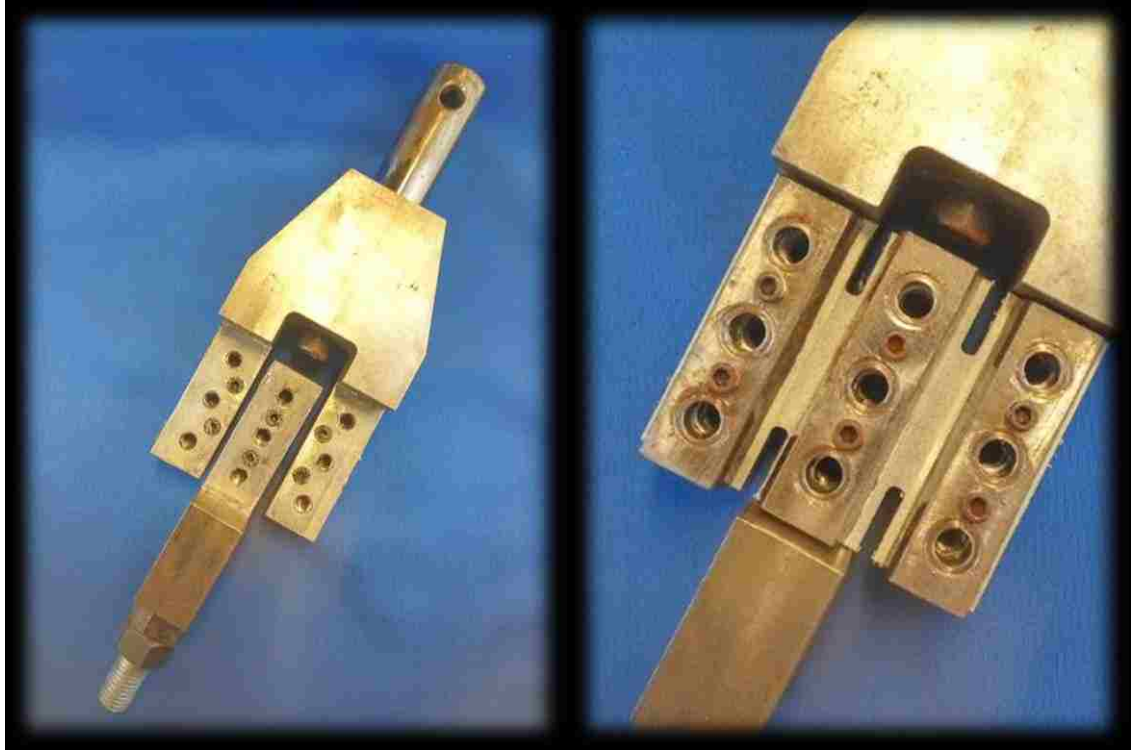


Figure 24 – Shear test fixture

### 3.3 Finite Element Simulation of Nakazima Tests

The purpose of the finite element simulations was to accurately predict the strain distribution in the TRIP780 sheet specimens deformed in formability tests, as well as to design and optimize the blank geometries to achieve the desired strain paths in the formability tests. LS-DYNA SMP971 R800 was configured on 4 threads to run the simulations. LS-Prepost 4.3 was used as the main pre-processor.

While LS-DYNA is widely used to analyze high speed impact problems with many contact discontinuities in explicit mode, the current release of the code supports a wide selection of material models and contact algorithms for implicit mode. The implicit solving mode is known for its unconditional stability, so that a much larger time-step size can be used making the calculation less time-consuming. Since Nakazima tests are

typically conducted at a quasi-static loading rate, inertia and dynamic effects can be conveniently neglected; the contact conditions are also not complex and have low severity of discontinuities. Therefore, implicit time integration was selected for the FE simulation of TRIP780 formability tests for its efficiency and robustness. The implicit scheme was configured with a time-step size of 0.05 s, and the displacement and energy convergence tolerance defaulted to 0.001 and 0.01, respectively. This configuration on four CPU threads provides a computing cost advantage of about ten times, over an explicit configuration over 16 threads with comparable results.

A fine mesh in a radial pattern was used to show the detailed deformation and strain distribution of the Nakazima specimen clamped with circular rings. Directions of all elements for the specimen were defined relative to the rolling direction of the sheet. Mesh size was 1.0×1.0 mm at the center of the specimen, and gradually increases as it moves away from the center. The aspect-ratio of elements was kept well under 1.5 for the core area where the strain distribution is to be analyzed. The hemispherical punch had the same mesh size of 1.0×1.0 mm, while the other die surfaces were generally discretized with a coarser mesh. The die surfaces where a radius was present were meshed with reduced element size to better represent the surface contour, and clearances were carefully defined for shell thickness scaling and thickness update.

The small elastic deformation of the dies was ignored in this study. The die surfaces that interact with the specimen (the top and bottom dies, and the punch) were modeled as rigid materials with Belytschko-Tsay reduced integration shell elements without thickness. On the other hand, the sheet specimen was modeled with fully-integrated shell elements, with shell thickness updates and five integration points through the thickness. A version of Hill's 1948 anisotropic material model (MAT-122 in LS-DYNA) was applied to the specimen, with a piecewise linear flow curve acquired from the successive flat rolling and tensile tests to define the work hardening behaviour, and three R-values to define the planar anisotropy of the sheet material. There was no forming limit or failure criterion applied to the model. The clamping of the specimen was modeled by fixing all six degrees of freedom of a set of nodes located on a circle where clamping actually

happens on the physical specimen. As a result, there was no modeling of the lock bead or lock rings. The displacement of the punch was modeled with a prescribed motion.

The contact between the dies and the specimen was modeled with a segment-based and penalty-based contact algorithm, especially suited for implicit solving, with friction modelled by Coulomb's law. The static and dynamic coefficient of friction were set to 0.05 and 0.04, respectively, while the exponential decay coefficient was set to 1000. A reduced keyword input is included in Appendix B.

As shown in Figure 25, a special "material coordinate system" was applied for the model to represent surface strains that follow the Z deformation of the surface, while conserving the X and Y direction projected on the X-Y plane. This way of representing the strain closely resembles the way that strains are measured on etched grids.

Specimen geometry designs were inspired from the work of Raghavan [43] with circular cut-outs that reduce stretching in the minor direction. Exact specimen dimensions were determined from simulation results. Since the balanced-biaxial strain path (or the closest approximation) is always produced with a fully clamped specimen, and the uniaxial strain path is always produced with a narrow specimen resembling a tensile specimen, the focus of simulations was on the plane strain specimen. All other specimen geometries were designed such that the strain path achieved in the gauge would lie between uniaxial tension and plane strain tension, or between plane strain and balanced-biaxial tension.

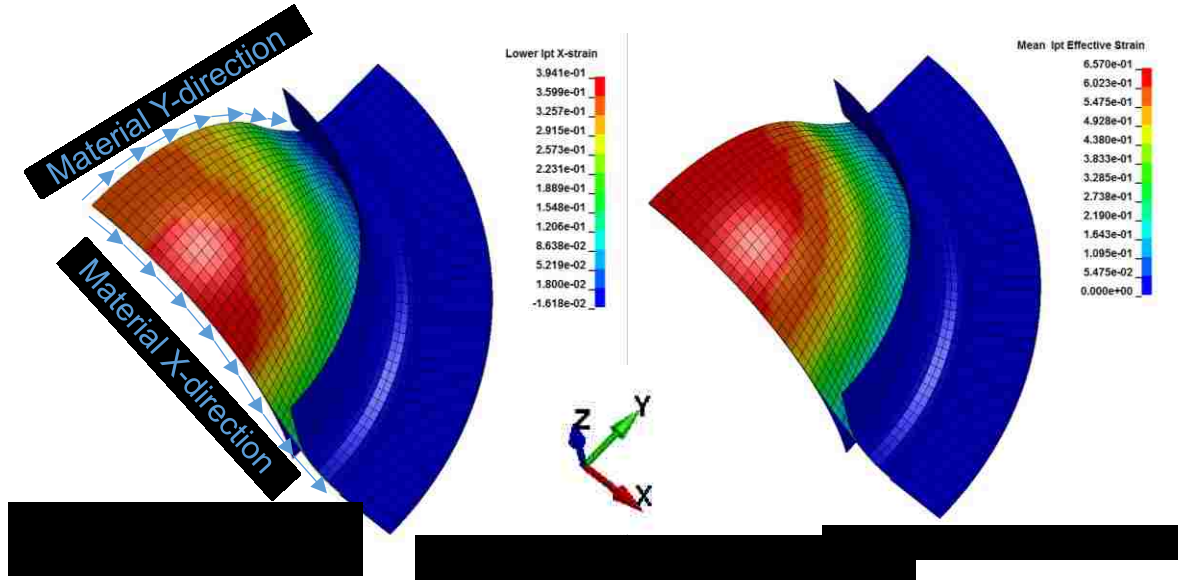


Figure 25 – A quarter simulation model for a fully clamped Nakazima test

The simulation model was verified with energy and contact behaviour inspection. Model validation was conducted with the validation metric shown in Equation 3.1, as suggested in the work of Oberkampff et al. [44], where  $V$  is the validation metric,  $y(x)$  is the theoretical results predicted by the LS-DYNA FEA model, which is validated against  $Y(x)$ , the experimental results. An accumulated error,  $Err$ , was also calculated as shown in Equation 3.2. A mesh sensitivity study was conducted for the simulation results.

$$V = 1 - \frac{1}{L} \int_0^L \tanh \left| \frac{y(x) - Y(x)}{Y(x)} \right| dx \quad (3.1)$$

$$Err = \frac{1}{L} \int_0^L \left| \frac{y(x) - Y(x)}{Y(x)} \right| dx \quad (3.2)$$

### 3.4 Formability Tests

The Nakazima test was chosen due to the simplicity of the experimental setup. The tests were performed with a double-action hydraulic press, with approximately 1000 kN of force available for clamping (blank holder force) and forming (punch force), respectively. The press is equipped with LVDT position sensors and load cells to measure blank holder and punch forces, and a data acquisition system that outputs the loads and positions at over 30 Hz. Stereo cameras were mounted on top of the press, ensuring the specimen is fully visible in the field of view of the cameras through the conical opening in the crown of the press. All fasteners on the camera mount were tightened down to keep the structure rigid. Cameras were focused with consideration of the out-of-plane motion of the specimen. An aperture value of 16 (smallest available) was used to improve the depth of focus. Since the vibrations of the press would make the calibration go off over time, calibration was conducted after each test, with consideration of the out-of-plane motion of the specimen.

The Keeler formability analysis method and the new analysis methods that use DIC strain data were integrated into the same test, with a speckle pattern generated by spray paint over an etched specimen. The strain measurements from etched grids were accessed by removing the paint from the specimen. The friction between the punch and the specimen was varied from no lubrication, Vaseline, Teflon spray, thin Teflon film, or any combination thereof.

Specimen geometries were designed for seven strain paths, with #1, #4 and #7 being uniaxial tension, plane-strain and balanced-biaxial, respectively. Strain path #6 and #7 were both tested with fully clamped specimens, but were modified by applying different friction conditions between the punch and the specimen. Specimen geometries are included in Appendix C.

A brief experimental procedure is specified below and a more detailed procedure is provided in Appendix D.



- Shear sheet metal into full blank size, apply the grids with electro-etching and machine to the designed specimen geometry
- Clean specimen surface and apply speckle pattern with spray paint
- Setup the DIC System along with dedicated lighting on top of the Eagle Press, ensure the system is firmly fixed down, calibrate the DIC stereo rig and watch out for any kind of image distortions
- Adjust the process control on the “Eagle Press”, perform Nakazima tests, stop tests at the onset of necking if needed, export and store output data from each test before running a new test
- Conduct grid strain measurement on formed specimens with FMTI grid gun
- Conduct DIC post-processing and strain analysis
- Conduct calculations and analyses with custom built MATLAB code to derive FLC

All the output variables from the press data acquisition and from the DIC post processing were analyzed, and different necking criteria were examined, as previously described in Section 2.5.3. The criterion that consistently produced a forming limit curve closest to that obtained by the Keeler method was chosen to be the preferred criterion; provided that a result from Keeler method is available and valid for the given strain path.

A section view of the tooling is included in Figure 26. A process flow chart for the formability testing and data analysis is included in Figure 27. More images of the testing setup are included in Appendix E.

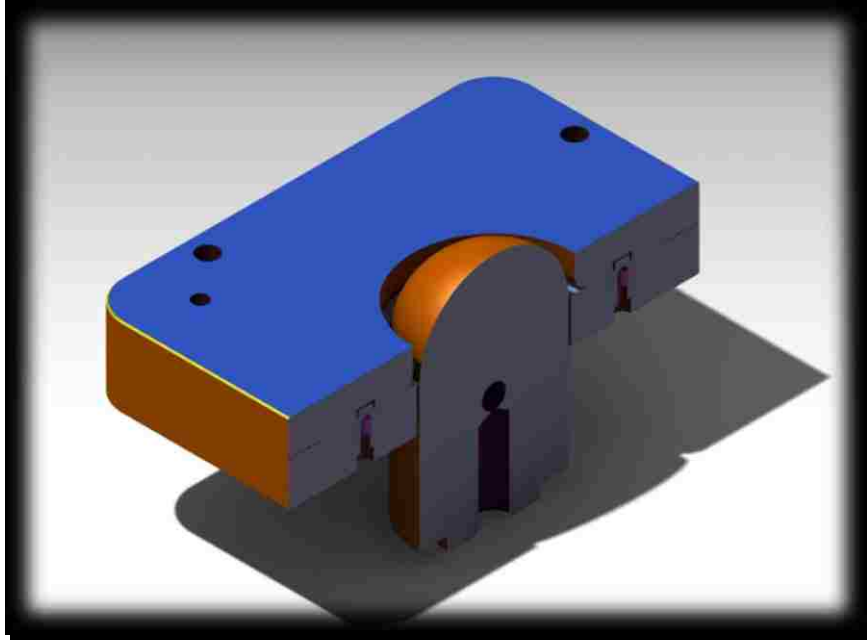


Figure 26 – Section view of Nakazima test tooling

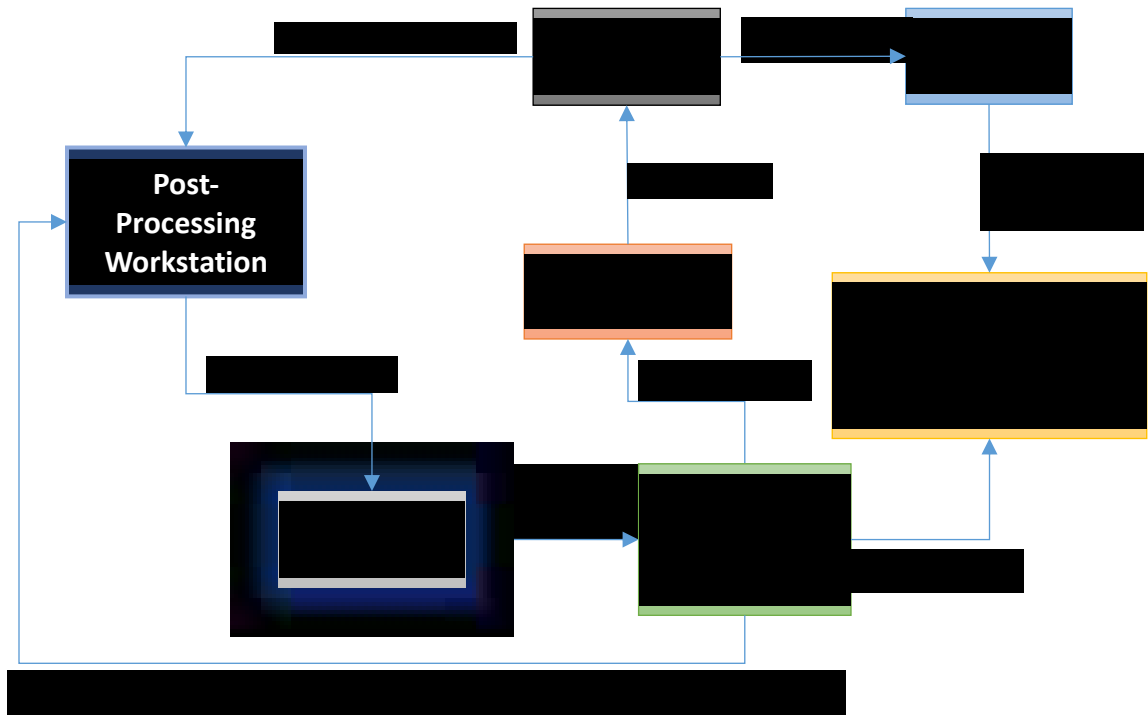


Figure 27 – Nakazima test process flow chart

## 4. Results and Analysis

### 4.1 Tensile Test Results Analysis

The post-processing of flat rolling and tensile tests was performed with a custom MATLAB code. The rolling induced prestrains are shown in Table 3. The strain measurement produced by the mechanical strain gauge was comparable to the major strain history obtained from DIC post processing up to maximum load, and provided better quality data in terms of noise suppression. Beyond maximum load, the strain measurements diverged because the gauge length is different. The minor strain was only produced by the DIC strain measurement since no mechanical strain gauge is applied in the minor direction.

The code synchronized the data output at very different sampling frequencies from the 2D DIC strain measurement and the MTS tensile machine, and considered the pre-load and the small amount of strain induced by tightening the grips before loading, and compensated for the starting condition of the tests. A series of numerical operations were performed to calculate the elastic modulus (Young's modulus), yield stress and strain. As shown in Figure 28, 'Mech', 'Vid' and 'DIC' represent strain measurements from the mechanical gauge, video extensometer, and DIC post processing, respectively. The in-plane stress and strain history data were then converted to true stress and true (logarithmic) plastic strain to obtain the flow curve. The through-thickness strain was obtained with an assumption of constant volume. Lankford coefficients were calculated from strain ratios at 75% maximum major strain, as shown in Figure 29. The flow curve data was output to a file for further processing.

After data from all repeat tests conducted for all levels of rolling-induced pre-strains, another MATLAB code was used to derive an overall work hardening behaviour flow curve that characterizes the material up to a strain level over 1.0 mm/mm strain. As shown in Figure 30 for the rolling direction results, the green x symbols represent the original data, and the red curve shows the stress-strain curve fitted to a power law

equation ( $\sigma = K \varepsilon_p^n$ ). Since the purpose of creating this flow curve is to characterize the material at high strain level, the fitting of the curve is weighted more towards the data at higher strains. As a result, the fitted power law curve does not perfectly resemble the flow curve in the low strain range, which is obtained from a tensile test with zero pre-strain. With concerns that this may affect the accuracy of simulation results, a piece-wise linear curve was derived from the original flow curve at low strains and from the fitted curve at high strains, and is shown in Figure 30 as blue dots. This piece-wise linear curve is intended for input in LS-DYNA simulations, so that the fit can remain a simple power law relation with only two parameters. Results for the transverse direction are included in Figure 31. The fitted power law equation yields  $K = 1399$ ,  $n = 0.21$  for the rolling direction, and  $K = 1388$ ,  $n = 0.19$  for the transverse direction. The coefficient of determination are 0.991 and 0.987, for the two directions, respectively. The anisotropy of the material can be described by  $R_0$ ,  $R_{90}$  and  $R_{45}$ , which are determined to be 0.62, 0.76 and 0.85, respectively.

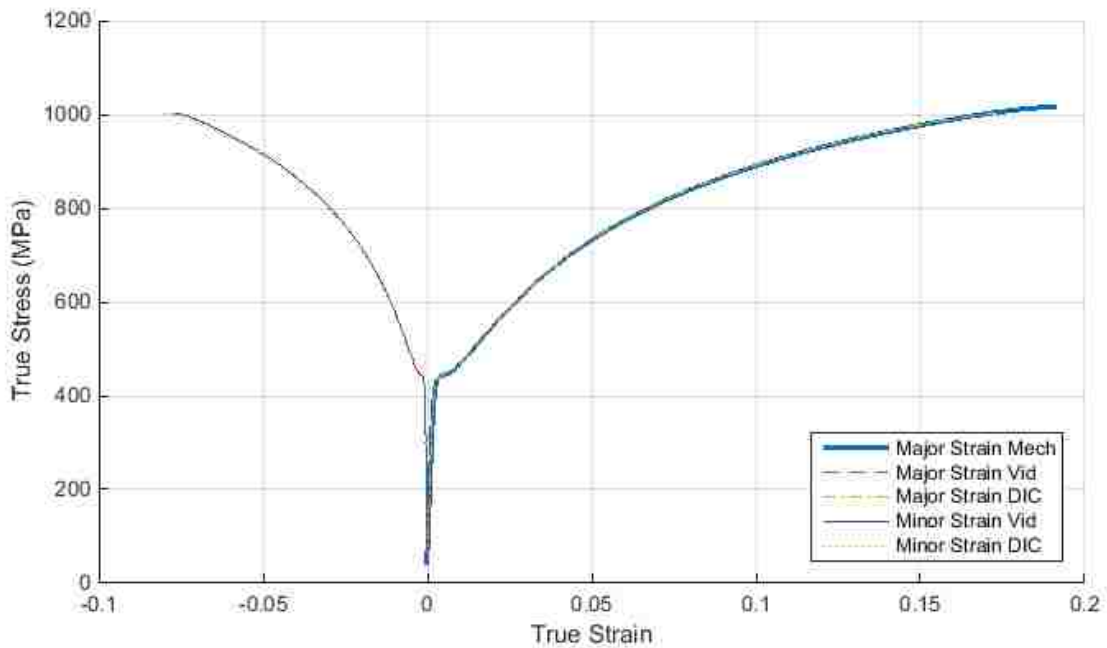


Figure 28 – Tensile stress-strain curve

Sample	$l_0$	$l_f$	$w_0$	$w_f$	$\epsilon_1$	$\epsilon_2$	$\epsilon_{3,cal}$	$\epsilon_{eff}$
AR-1	25.220	<del>25.220</del>	15.130	<del>15.130</del>	<del>0.000</del>	<del>0.000</del>	<del>0.000</del>	<del>0.000</del>
AR-2	25.220	<del>25.220</del>	15.130	<del>15.130</del>	<del>0.000</del>	<del>0.000</del>	<del>0.000</del>	<del>0.000</del>
AR-3	25.220	<del>25.220</del>	15.130	<del>15.130</del>	<del>0.000</del>	<del>0.000</del>	<del>0.000</del>	<del>0.000</del>
RP1-1	25.220	30.210	15.130	15.300	0.181	0.011	-0.192	0.215
RP1-2	25.220	30.250	15.130	15.310	0.182	0.012	-0.194	0.217
RP1-3	25.220	30.250	15.130	15.310	0.182	0.012	-0.194	0.217
RP2-1	25.220	36.180	15.130	15.330	0.361	0.013	-0.374	0.424
RP2-2	25.220	36.200	15.130	15.330	0.361	0.013	-0.375	0.425
RP2-3	25.220	36.300	15.130	15.320	0.364	0.012	-0.377	0.428
RP3-1	25.220	42.250	15.130	15.550	0.516	0.027	-0.543	0.612
RP3-2	25.220	42.460	15.130	15.510	0.521	0.025	-0.546	0.616
RP3-3	25.220	42.620	15.130	15.550	0.525	0.027	-0.552	0.622
RP4-1	25.220	50.250	15.130	15.550	0.689	0.027	-0.717	0.812
RP4-2	25.220	50.520	15.130	15.520	0.695	0.025	-0.720	0.817
RP4-3	25.220	50.380	15.130	15.540	0.692	0.027	-0.719	0.815
RP5-1	25.220	62.250	15.130	15.570	0.904	0.029	-0.932	1.060
RP5-2	25.220	62.260	15.130	15.570	0.904	0.029	-0.932	1.060
RP5-3	25.220	62.330	15.130	15.600	0.905	0.031	-0.935	1.063
TD-1	25.220	<del>25.220</del>	15.130	<del>15.130</del>	<del>0.000</del>	<del>0.000</del>	<del>0.000</del>	<del>0.000</del>
TD-2	25.220	<del>25.220</del>	15.130	<del>15.130</del>	<del>0.000</del>	<del>0.000</del>	<del>0.000</del>	<del>0.000</del>
TD-3	25.220	<del>25.220</del>	15.130	<del>15.130</del>	<del>0.000</del>	<del>0.000</del>	<del>0.000</del>	<del>0.000</del>
TP1-1	25.220	30.720	15.130	15.300	0.197	0.011	-0.208	0.235
TP1-4	25.220	30.110	15.130	15.250	0.177	0.008	-0.185	0.209
TP1-5	25.220	30.000	15.130	15.230	0.174	0.007	-0.180	0.204
TP2-1	25.220	35.580	15.130	15.450	0.344	0.021	-0.365	0.410
TP2-4	25.220	35.050	15.130	15.360	0.329	0.015	-0.344	0.389
TP2-5	25.220	34.850	15.130	15.360	0.323	0.015	-0.339	0.382
TP3-1	25.220	42.560	15.130	15.620	0.523	0.032	-0.555	0.623
TP3-2	25.220	42.510	15.130	15.550	0.522	0.027	-0.549	0.619
TP3-3	25.220	42.250	15.130	15.600	0.516	0.031	-0.547	0.614
TP4-1	25.220	50.310	15.130	15.710	0.691	0.038	-0.728	0.820
TP4-2	25.220	50.410	15.130	15.740	0.693	0.040	-0.732	0.823
TP4-3	25.220	50.350	15.130	15.790	0.691	0.043	-0.734	0.824
TP5-1	25.220	60.280	15.130	15.850	0.871	0.046	-0.918	1.034
TP5-2	25.220	60.440	15.130	15.740	0.874	0.040	-0.914	1.033
TP5-3	25.220	60.050	15.130	15.930	0.868	0.052	-0.919	1.033
DD-1	25.220	<del>25.220</del>	15.130	<del>15.130</del>	<del>0.000</del>	<del>0.000</del>	<del>0.000</del>	<del>0.000</del>
DD-2	25.220	<del>25.220</del>	15.130	<del>15.130</del>	<del>0.000</del>	<del>0.000</del>	<del>0.000</del>	<del>0.000</del>
DD-3	25.220	<del>25.220</del>	15.130	<del>15.130</del>	<del>0.000</del>	<del>0.000</del>	<del>0.000</del>	<del>0.000</del>

Table 3 – Rolling Strain

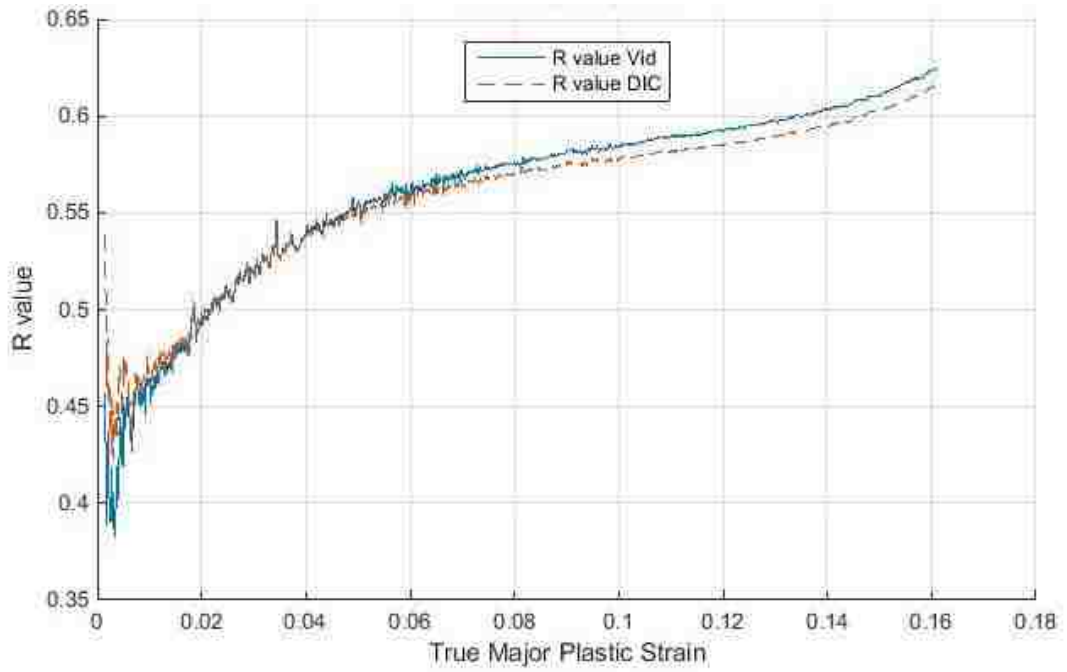


Figure 29 – R-value vs. true plastic strain

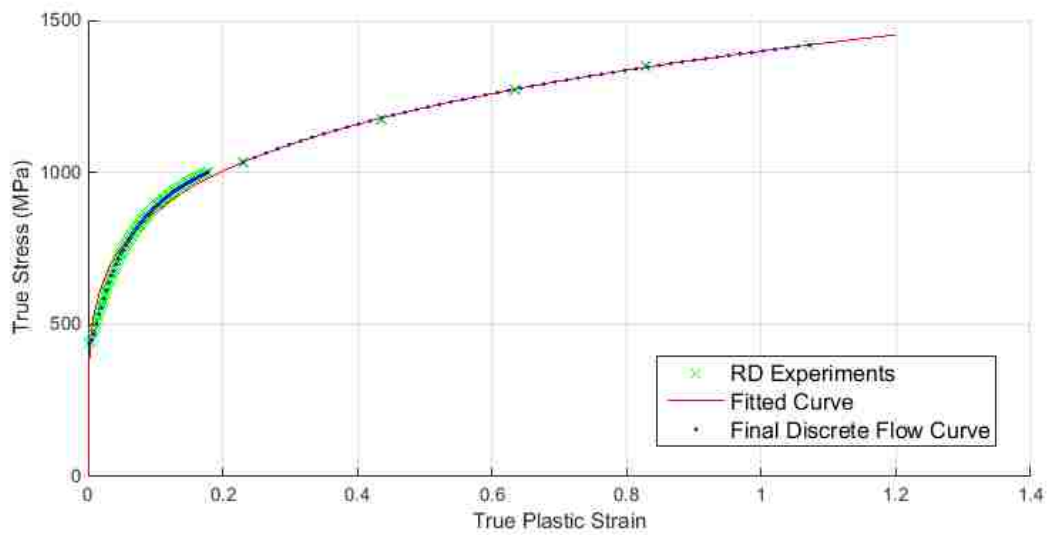


Figure 30 – Extended flow curve (RD) obtained from tensile tests after successive flat rolling

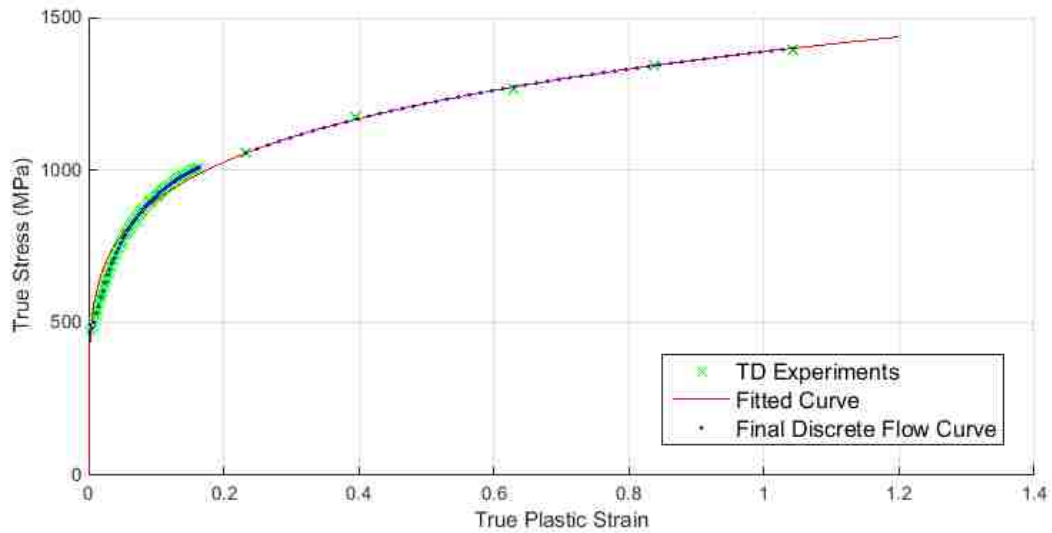


Figure 31 – Extended flow curve (TD) obtained from tensile tests after successive flat rolling

## 4.2 Shear Test Results Analysis

The post-processing of shear tests was also performed with a custom MATLAB code. The data synchronization and calculations were performed in a similar manner as for tensile tests. Since the setup was originally designed for cyclic testing, the gauge area of the specimen was larger than a typical shear test, which caused the stress state to deviate from ideal simple shear because of some bending effects. With a rotation of coordinate system for strains, the first and second principal strains were analyzed and test data were plotted as principal stress-strain curves (Figure 32). This was to account for the small but maybe significant normal strains that developed during the test, as shown in Figure 33. The flow curve was then determined in terms of true stress and true plastic strain data, shown as a blue line in Figure 34. The flow curve with shear stress converted to effective stress is shown as a red line, also in Figure 34, for comparison.

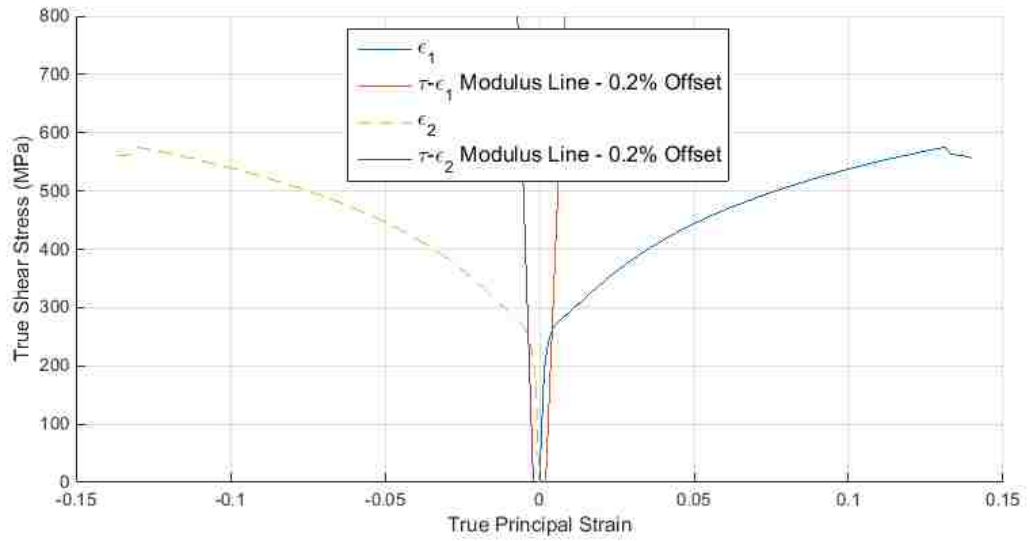


Figure 32 – Shear stress - principal strain curves obtained from a shear test

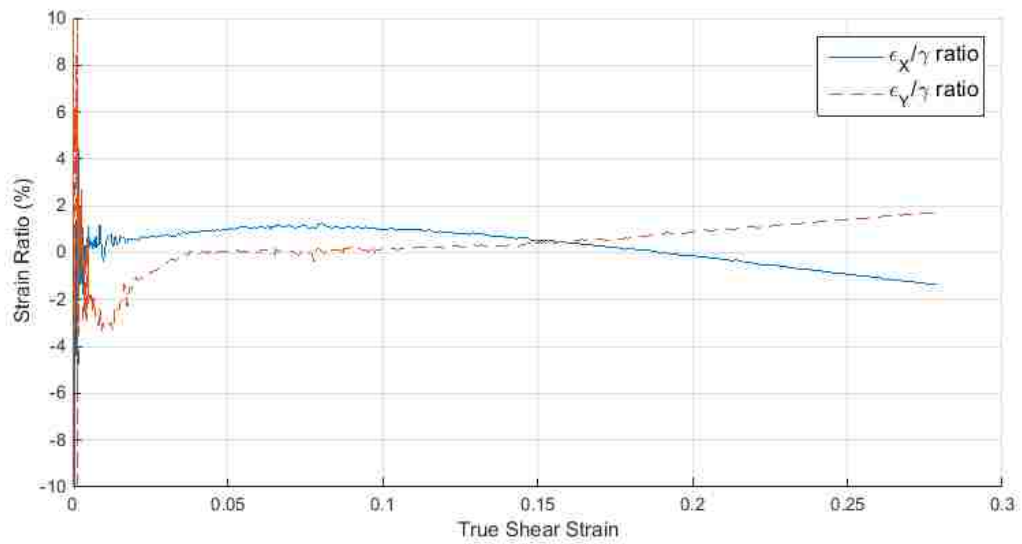


Figure 33 – Normal/shear strain ratio in a shear test



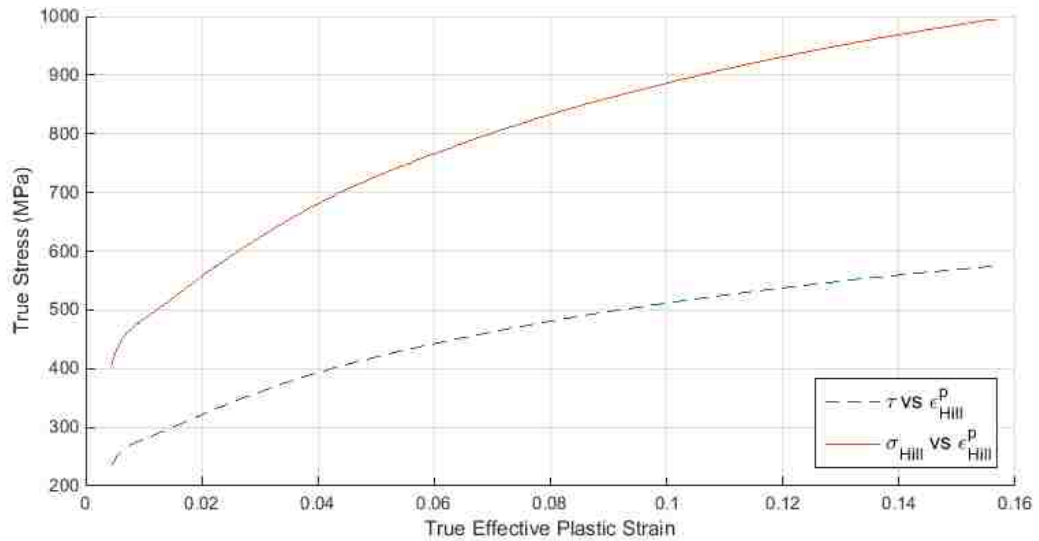


Figure 34 – Shear test flow curves

### 4.3 Simulation Results Analysis

Finite element simulations were used to predict the strain distribution on the surface of the specimen, and to examine the strain path of the elements in the gauge area, in order to help design the geometry of each Nakazima specimen (Figure 35). At the same time, the strain distribution and strain path measurements from the experiments were used to calibrate and validate the simulation model. With the implementation of fully-integrated shell elements combined with 5 points through the thickness, and the surface-to-surface segment based “mortar” contact algorithm, the simulation results agree with the experimental results very well. Figure 36 shows the predicted and experimental major and minor strain distribution across a quarter plane-strain specimen at the same punch displacement of 17.1mm. The validation metrics calculated for the major and minor strain distributions are 0.965 and 0.947, respectively. The accumulated error calculated for the major and minor strain distributions are 0.0354 and 0.0536, respectively. Figure 37 shows the predicted and experimental strain path of an element in a plane-strain specimen that eventually develops a neck. The simulation captures the nonlinear strain path caused

by the bending effect of the hemispherical Nakazima punch, and the magnitude of the minor strain caused by bending is accurately calculated. The simulated strain path does slightly deviate from the experimental strain path at higher major strain level, and the reason may be an inadequate material model for the complex work hardening behaviour of TRIP780 steel in three-dimensional stress states. The simulation model does not include a failure criterion therefore it is not capable of predicting the onset of necking of the specimen. Nevertheless, the simple simulation model is shown to be effective for the purpose of designing specimen geometry. The conservation of energy was verified and contact behaviour was inspected; plots for model verification are included in Appendix F. Mesh sensitivity analyses were also conducted, with results shown in Figure 37. The strain path results from the three simulation runs (one original run, and two additional runs with greater mesh density) are right on top of each other; this indicates that the change in mesh density does not affect the behaviour of the model. The validation metrics calculated for the major and minor strain history predicted with normal mesh density are 0.865 and 0.716, respectively. The accumulated error calculated for the major and minor strain history predicted with normal mesh density are 0.116 and 0.189, respectively.

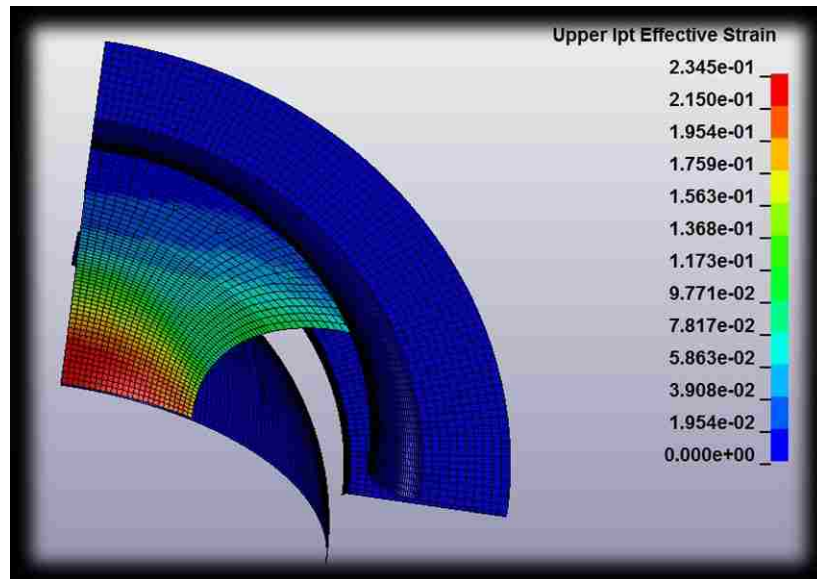
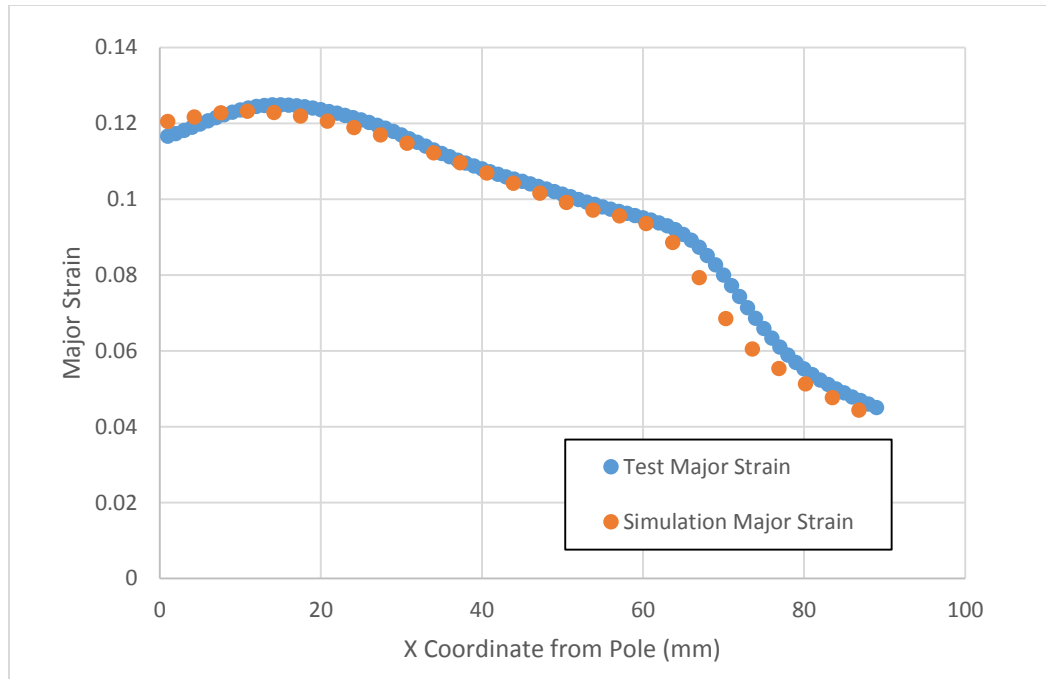
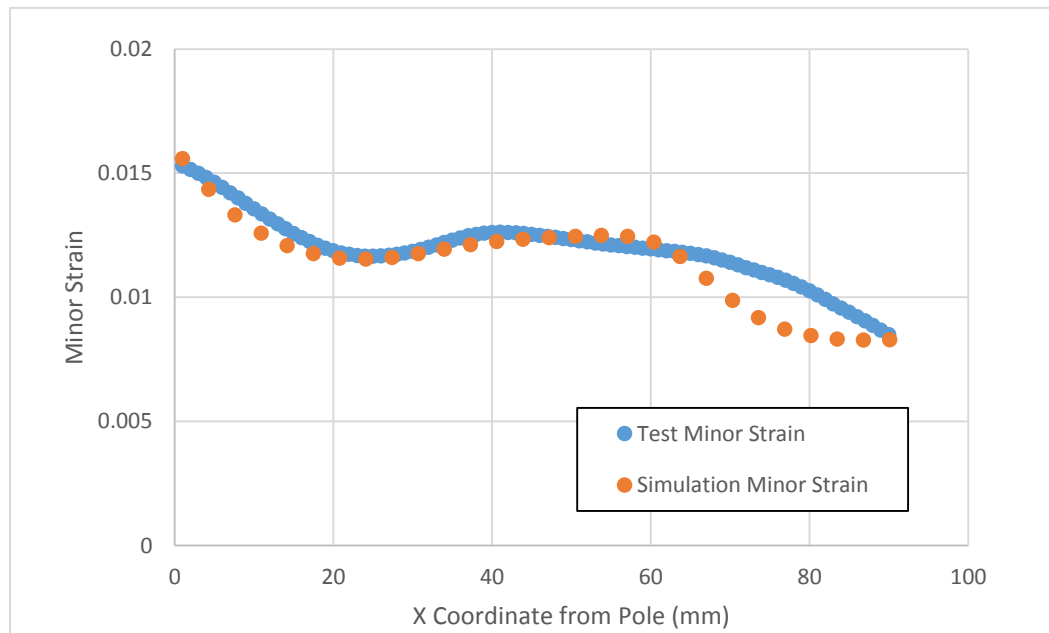


Figure 35 – Finite element model of a plane strain Nakazima specimen showing the distribution of the effective strain



a)



b)

Figure 36 – Validation of the predicted strain distribution in a plane-strain Nakazima test specimen in terms of, a) the major strain, b) the minor strain

The simulation helped confirm the specimen geometry for the plane-strain specimen. The specimen geometry for all other strain paths was obtained by adjusting the minimum width of the specimen, and no further simulation was needed. Figure 35 is an illustration of the simulation model for the plane-strain specimen, Figure 38a) is a photograph of a plane-strain specimen, after it was cut to size using water-jet cutting, and Figure 38b) is a photograph of the formed plane-strain specimen used for validating the simulation.

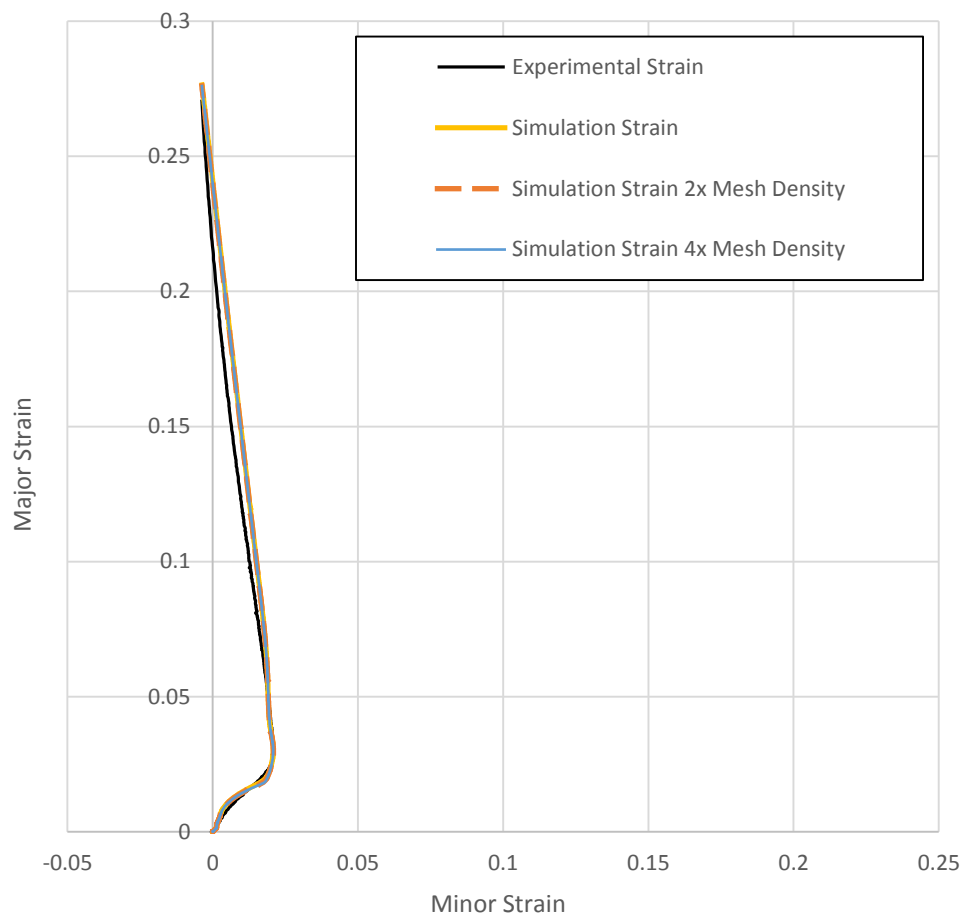
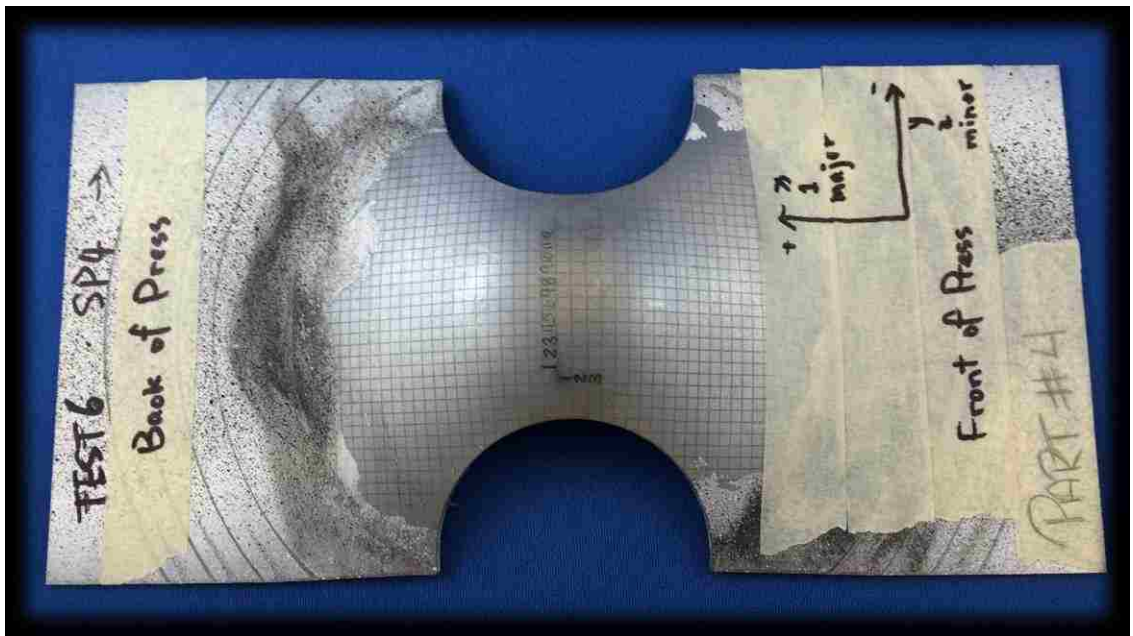


Figure 37 – Validation of the predicted strain path for a point near the center of a plane strain Nakazima specimen, with mesh sensitivity analysis



a)



b)

Figure 38 – Photograph of plane-strain Nakazima specimens: a) the undeformed blank, and b) the as-formed specimen

## 4.4 Analysis of Nakazima Test Results

The Nakazima test results were processed with a set of MATLAB codes that follow a similar procedure as that used to process previous experiments. As the post-processing for the Nakazima test is more complicated, robust numerical methods and high level automation were implemented to create an effective and efficient code. The code is designed to do all the analysis for one Nakazima test with the click of a button, given that the inputs are properly prepared. A series of formatted data input files, and a number of mandatory and optional parameters are to be specified in the parameter code for each test, and the common main code is called in for processing. This ensures that any change to the analysis process can be easily tested and verified, and the process kept consistent for all strain paths and all repeated test runs.

Since the Nakazima test involves a three-dimensional field of view for the DIC measurement, the data structure has one more independent variable to consider. It is important to note that the three-dimensional DIC still measures the strains “in-plane”, which is in two dimensions, because it is impossible for the cameras to view the through-thickness strain under the top surface of the specimen. The nature of the Nakazima test creates contoured surfaces on a formed blank, so the better term may be “in-surface” two-dimensional strains, where the x (major) and y (minor) axes bend and follow the contour of the top surface of the specimen, and at the same time remain straight lines when projected on the x-y plane, and the z axis is always normal to the surface of the specimen. This concept is similar to the material coordinate system as detailed in Section 3.3, and illustrated in Figure 25. Therefore, there are three independent variables in the data matrix, x-grid coordinate, y-grid coordinate and time. The dependent variables include x, y and z locations, strains, principal angles and uncertainty measures. A four-dimensional matrix is used to easily manage and access the DIC data.

The code first plots a load – displacement history comparison graph for multiple test runs of the same strain path, for visual verification of test repeatability. The tensorial strain data is extracted and converted into effective strains in order to search for the location of

necking on the x-y grid coordinates. The maximum effective strain in the x-y-time domain is identified as the location where necking begins. All further processing is then based on this identified point, and the variables (x, y and z locations, strains, etc.) are reduced to one-dimensional arrays in the time domain. Figure 39 is a plot of the strain paths determined at the identified necking location for each Nakazima specimen, with illustrations of the corresponding specimen geometries. The strain path for the identified necking location for an intermediate draw specimen (strain path #2, a strain path between uniaxial tension and plane-strain) is shown as the dashed green curve in the figure.

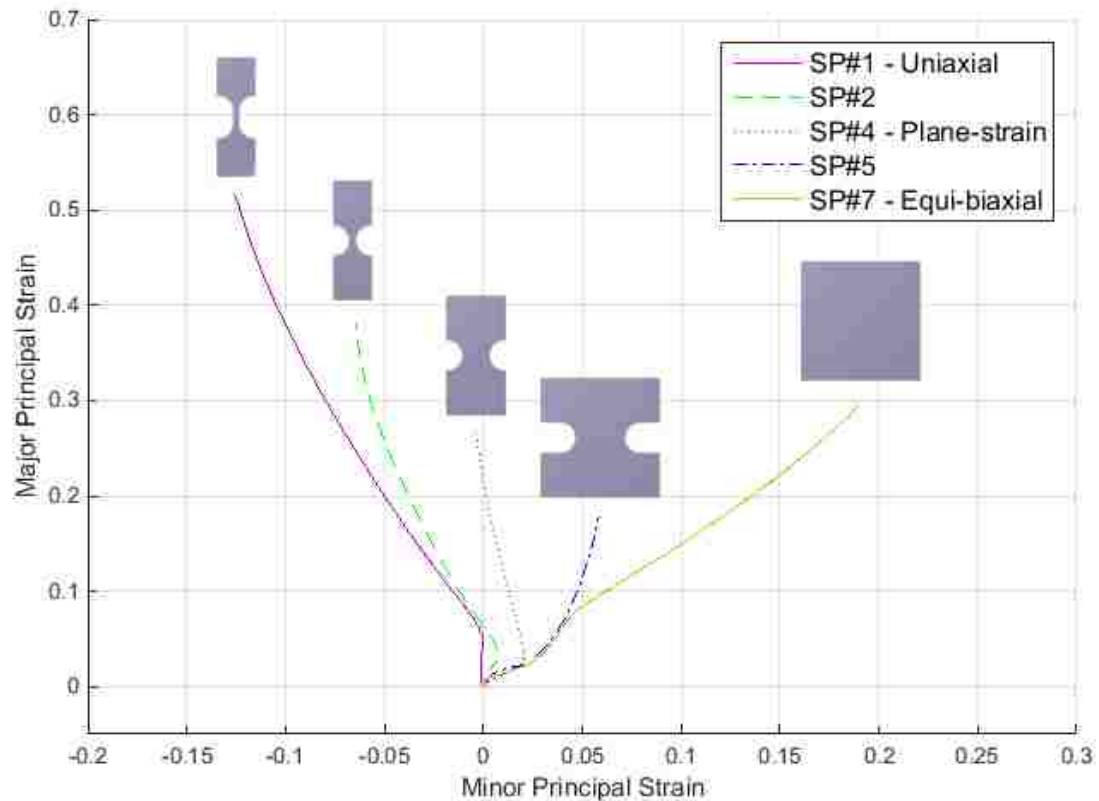


Figure 39 – Experimental strain paths in the Nakazima tests determined using DIC

Three necking criteria were implemented in the code: the surface slope criterion, the strain-rate departure criterion, and the maximum load criterion. The maximum load

criterion generally identifies the onset of necking much later than the other criteria. It is commonly seen that the maximum load is recorded at the last frame before specimen fracture when the sheet material is already well beyond the onset of necking. The maximum load criterion is therefore deemed not suitable for Nakazima tests.

The strain-rate departure criterion searches for the maximum major strain rate of a point that is 2.54 mm away from the identified necking location in the major direction: this point is referred to as “outside” the neck. The size of a standard square electro-etched grid is 2.54 mm, and is the distance it takes to “move out” of the necking zone for this sheet material. Due to the noise level in the strain data, a frequency low pass filtered digital differentiator [45] was used to calculate the strain rate. As all digital filters induce a phase lag, the strain rate for the outside point was calculated twice, once in the normal direction, and once in reverse, to compensate for the phase lag. As shown in Figure 40, the time at the onset of necking is identified as an average of the peaks of the yellow and the red dashed curves, again for the specimen subject to strain path #2. The strain-rate departure criterion only works when the specimen is formed all the way to fracture with an approximately constant loading rate; stopping the test at the onset of necking will affect the result for identification. This makes it impossible to directly compare the forming limit results from DIC on the same specimen with results from the Keeler method.

The surface slope criterion is the only method that identifies the onset of necking regardless of the rate effects, as it is geometry-based. The z-location data is plotted against the x-location data for a straight line that lies on the top surface of the specimen in the major direction, and intersects the identified necking point (Figure 41, for strain path #2 specimen). The x- and z-positions of this line are recorded in time history. Two digital differentiations are performed on the successive cross-section curves in the x-z plane for all instances, to produce  $dz/dx$  and  $d^2z/dx^2$  curves in time history. Since the punch is hemispherical, the portion of the curve near the top of the dome should approximately be an arc if no necking is occurring. Since the derivative of a semicircle function close to the mid-point of its x-span can be approximated by a straight line, the



deviation of the  $dz/dx$  curve from a straight line (i.e. the occurrence of a “bump”) can be used to identify the onset of necking (Figure 42). To further quantify the method, a maximum  $d^2z/dx^2$  of  $-0.003$  is used as a threshold value to identify the “bump” for this particular TRIP780 sheet metal (Figure 43 and Figure 44). Although the digital filtered differentiation causes a phase lag in the  $x$  direction, it is not important for identifying an instant in time, so the reverse filtering compensation is not required.

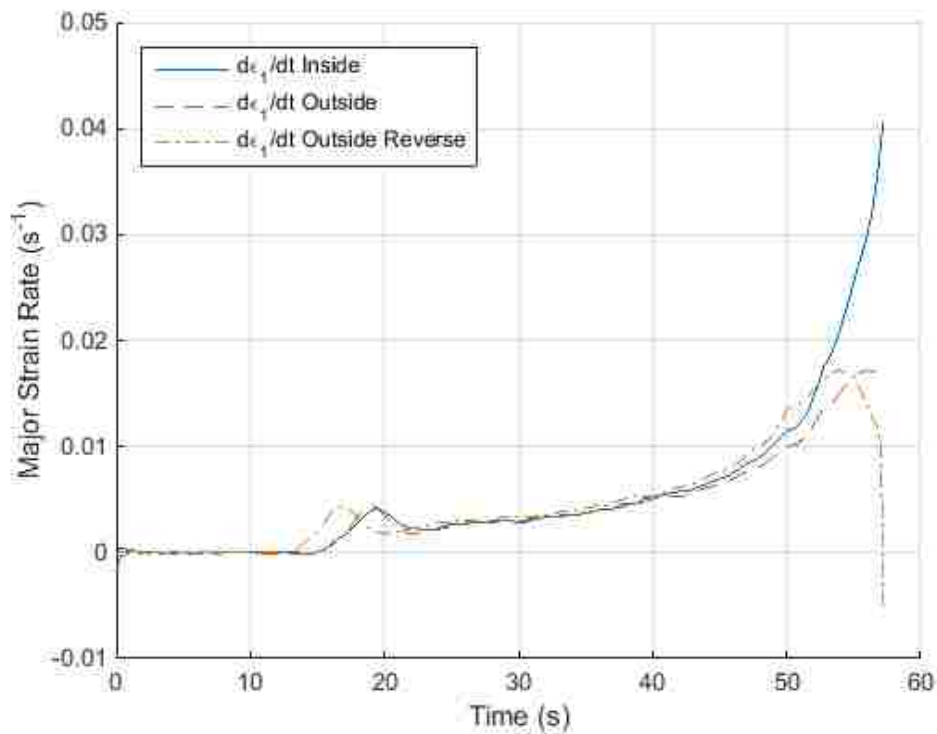


Figure 40 – Example of the strain-rate departure criterion for a Nakazima test specimen deformed along strain path #2

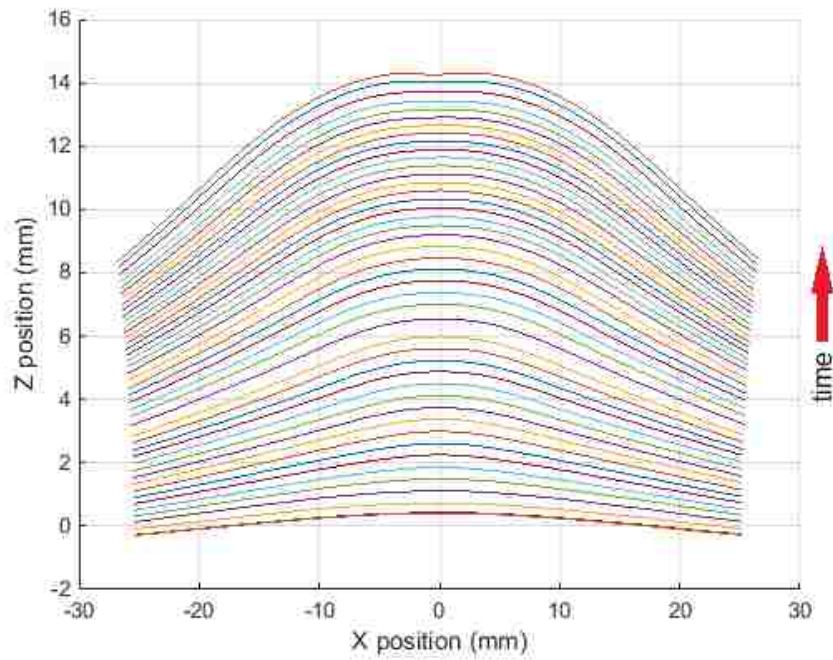


Figure 41 – Evolution of the 2D cross-sectional contour of the top surface of a Nakazima specimen,  $t = [0, 47.58]$  sec

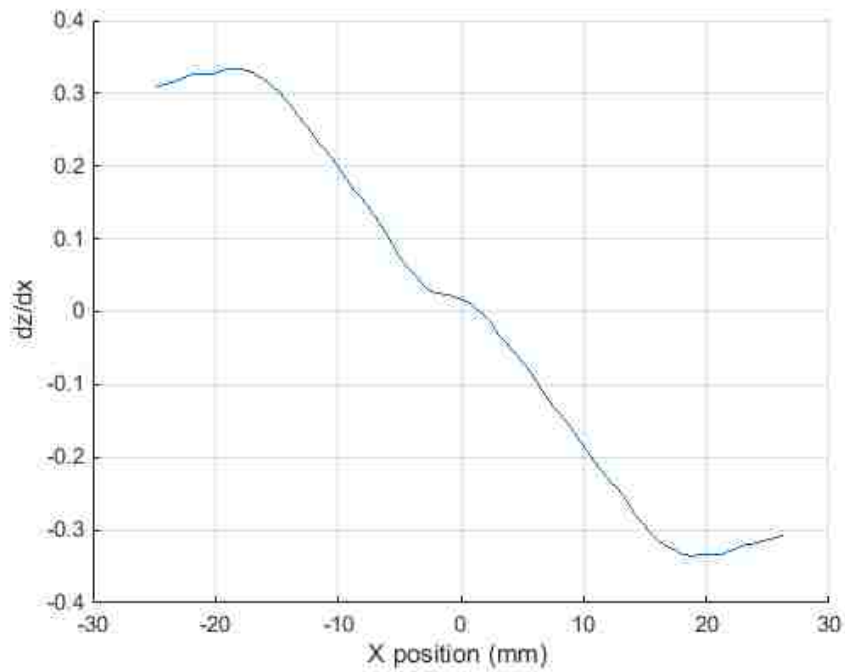


Figure 42 – 1<sup>st</sup> derivative of a cross-sectional contour from Figure 41

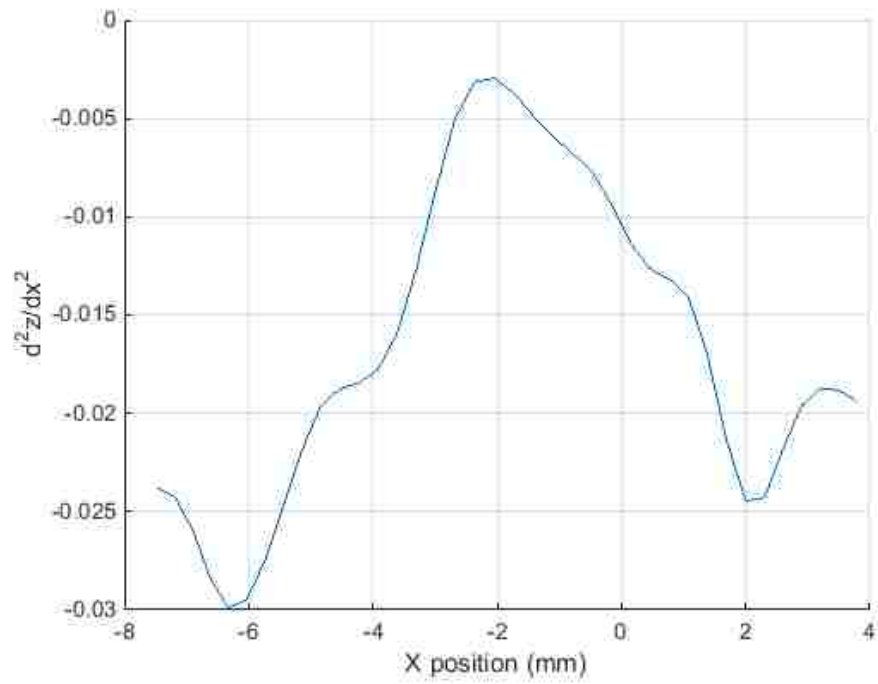


Figure 43 – 2<sup>nd</sup> derivative of a cross-sectional contour from Figure 41

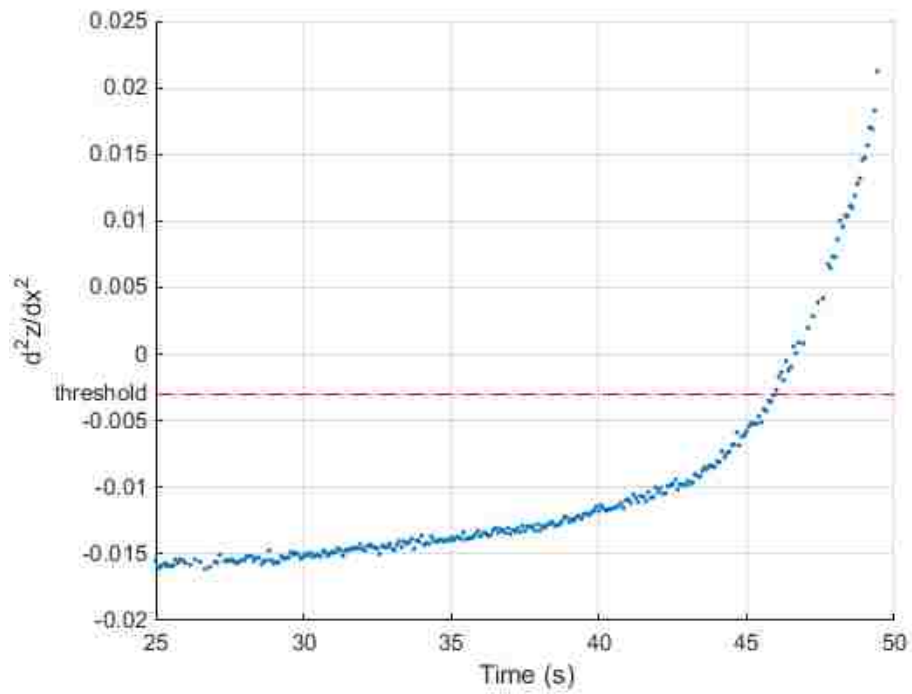


Figure 44 – Maximum 2<sup>nd</sup> derivative of cross-sectional contour vs. time

There are other strain, strain rate and derivatives of strain based methods available, as detailed in the literature review. However, given the noise level in the DIC strain data, and the punch speed control of the hydraulic press, most of these methods are ineffective. Figure 45 is an illustration of the oscillations in the second derivative of strain even after digital filtering. The specific method that utilizes the thickness strain and strain rate is promising, but due to the fact that the thickness strain can only be calculated with an assumption of volume constancy, without the deduction of elastic strains in major and minor strain, the accuracy of the method is also questionable.

It is worth noting that for strain paths #5 to #7, the specific conditions resulting from the combination of the biaxial strain path and the material properties of the TRIP780 sheet, produce no neck before cracking. Therefore, all the forming limits are taken as the strain state at the last frame before fracture. This assumes that the 12Hz sampling rate of the DIC cameras is sufficiently fast to capture the maximum safe strain just before fracture occurs.

Testing of specimens along strain path #5 yields a special forming condition, in which the combined effect of friction, strain path, strain distribution and the complex evolution of the through-thickness stress state creates a crack on the specimen where the measured effective strain is not the most severe. It is suspected that the contact stress induced by the hemispherical punch increases the stress triaxiality at the location of the crack, and suppresses the formation of a neck. As indicated in [46], contact between the sheet metal and the forming die can generate a compressive hydrostatic stress, which tends to suppress the damage and change the failure mode of the material.

Testing of specimens for strain path #6 also yields especially difficult forming conditions, in which the lack of lubrication causes the neck location to move significantly and inconsistently away from the dome of the specimen, resulting in random unanticipated variations in strain path. Results for tests along strain path #6 were therefore removed from the analysis.

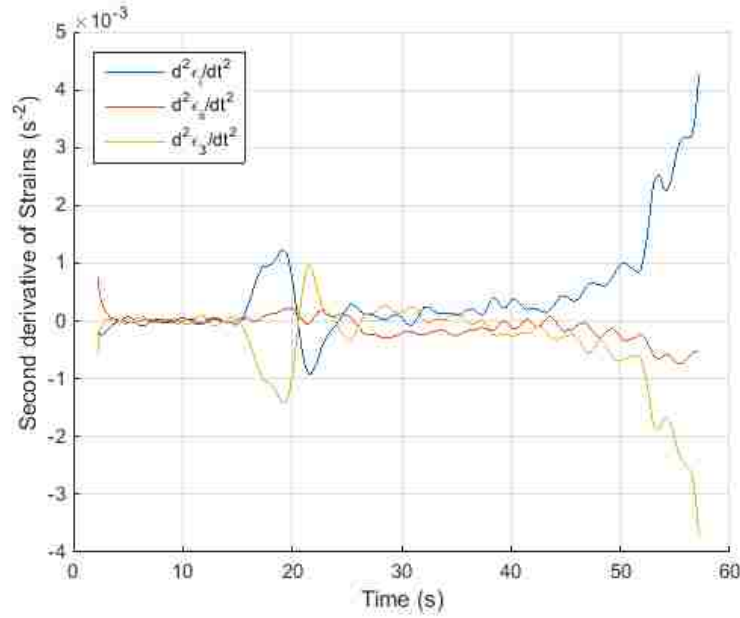


Figure 45 – Evolution of the 2<sup>nd</sup> derivative of strains in time

The process-dependent effects of the Nakazima tests were compensated, as documented in [33]. An analytical method (Equation 4.1) was used to find the curvature,  $\kappa$ , at the necking location, and the curvature effect was compensated.

$$R = \frac{\left[1 + \left(\frac{dy}{dx}\right)^2\right]^{\frac{3}{2}}}{\left|\frac{d^2y}{dx^2}\right|} \quad \text{and} \quad R = \frac{1}{|\kappa|} \quad (4.1)$$

The thickness strain history was used directly instead of the interpolation method for specimen thickness. A plot of the strain paths for the outer, middle and inner layers is shown in Figure 46. Due to the elastic strain being neglected, principal strain increments that are sufficiently large (0.05 effective strain increments as specified in work of Min et al. [33]) were used to calculate the stress states, as the compensation method is based on FLSD. Figure 47 presents the results after they were corrected for curvature (bending effect) alone, for both curvature and strain path, and the results with all three corrections. The lowest strain state for the results with all three corrections should be chosen as the compensated forming limit.

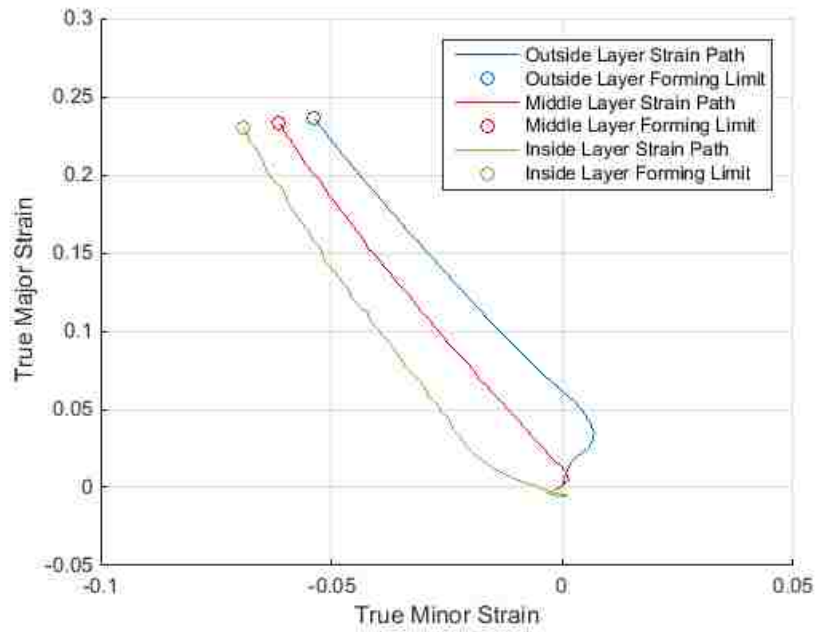


Figure 46 – An illustration of strain history for outer, middle and inner layers of a Nakazima specimen

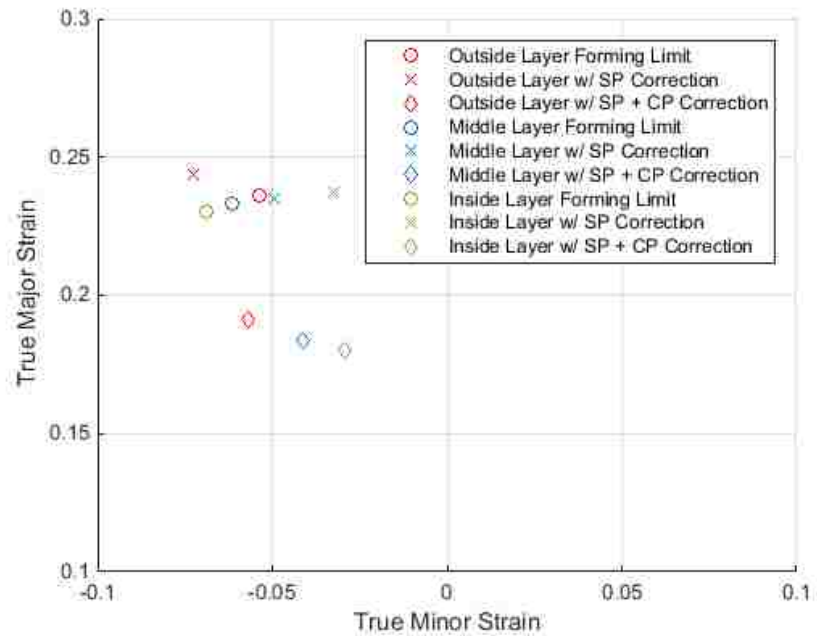


Figure 47 – Forming limit strain results after different corrections (SP: strain path correction; CP: contact pressure correction)

## 5. Discussion

### 5.1 The Work Hardening Behaviour of TRIP780

The work hardening behaviour of the TRIP780 steel was characterized with two different experimental methods, as detailed in previous sections. Figure 48 is a comparison of the flow curves in the lower strain level, obtained from the tensile tests along three material orientations and from the shear test. It can be observed that the three tensile flow curves are slightly different, due to the planar anisotropy of the material. The shear test flow curve only extends to just below 0.14 mm/mm strain, which is less than the tensile data, although it replicates the trend of the tensile curves very well. This is due to the fixture designed for cyclic shear loading failing to properly grip the specimen and also due to the large gauge area of the shear specimen. It nevertheless provides a good validation of the tensile results.

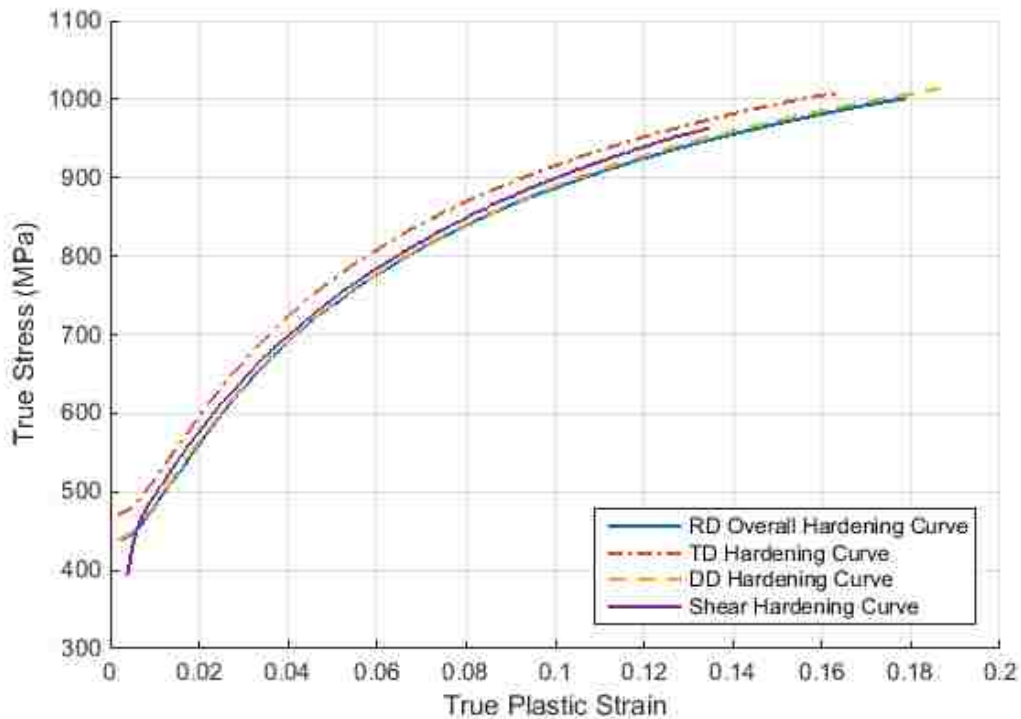


Figure 48 – The work hardening behaviour of TRIP780

As shown in Figure 49 and Figure 50, the rolling-induced prestrains help to extend the flow curves beyond 1 mm/mm strain. This is beneficial for input into FE simulation codes to predict the material behaviour when the forming process leads to an effective strain that exceeds that which can be obtained in a simple tensile test.

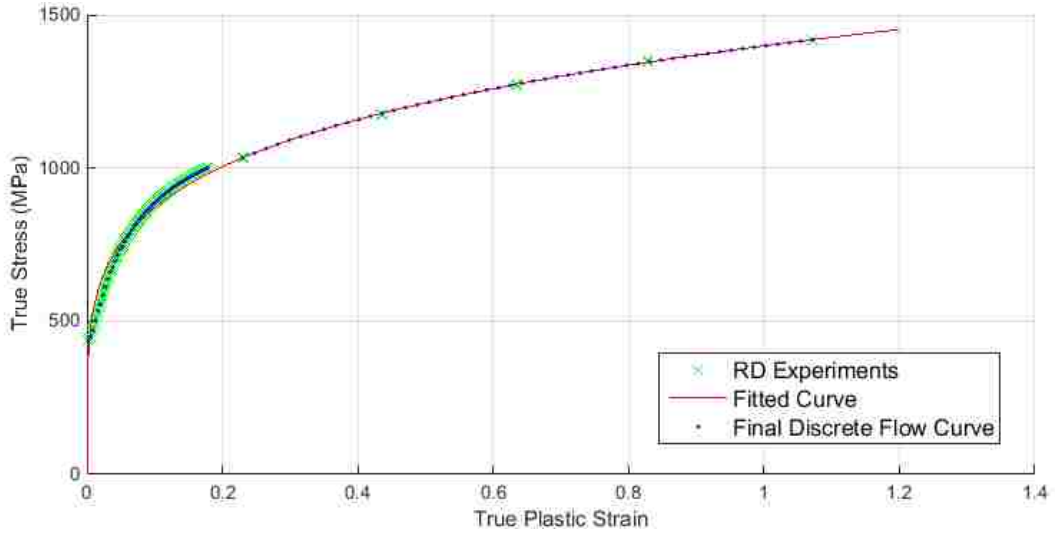


Figure 49 – Extended flow curve (RD) obtained from tensile tests after successive flat rolling

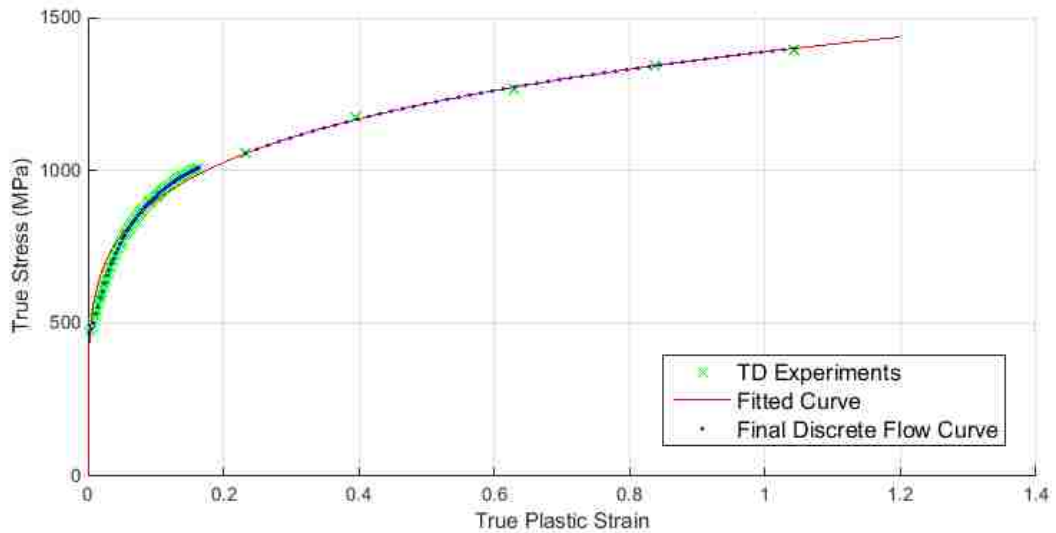
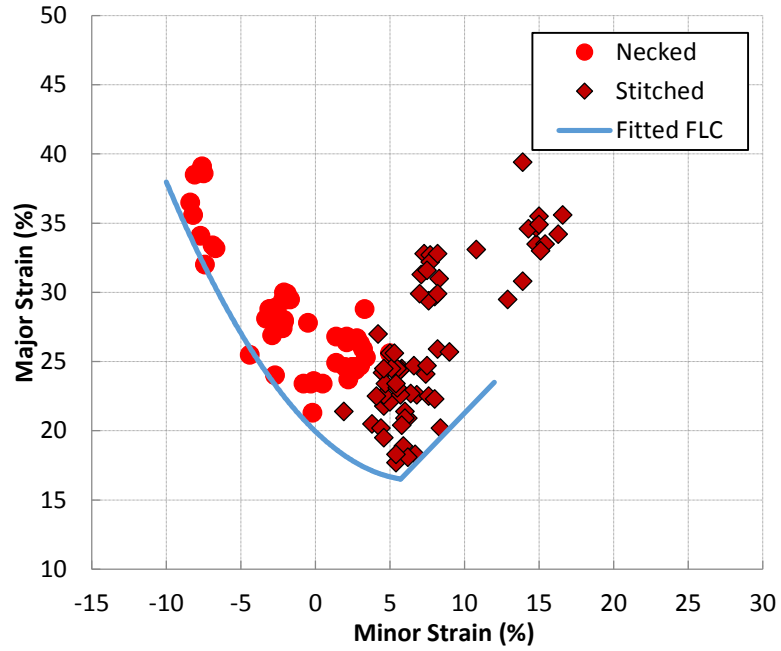


Figure 50 – Extended flow curve (TD) obtained from tensile tests after successive flat rolling

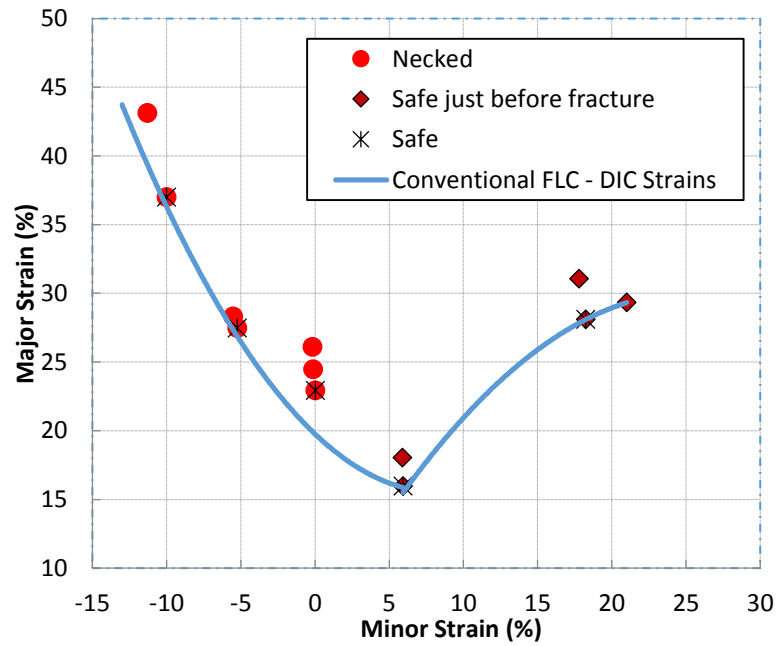


## 5.2 Forming Limits of TRIP780

The conventional FLC of the TRIP780 material is shown in Figure 51a): this FLC was determined from grid measurements on necked specimens for strain paths #1 to #4, and from stitched grid measurements on fractured specimens for strain paths #5 to #7. The stitching method can be quite subjective, and should only be used as a last resort if no better alternative is available. Since no necked specimen could be produced for strain paths #5 and #7, the right-hand side of the FLC would remain indeterminate without the stitched data. The FLC shown in Figure 51b) was determined from limit strains measured with DIC on the same specimens that were used for Figure 51a). The FLC in Figure 51b) was determined by using the same visual and tactile evaluation to identify the onset of necking as the Keeler method, and is intended to completely replace the labour-intensive grid measurement method. This FLC will also be a reference from which to evaluate the FLCs obtained by various DIC necking criteria. In Figure 51b), forming limit strain data from DIC measurement is shown for strain path #1 to #4, where the strain values were averaged in the area around the identified neck location, to mimic the resolution of the grid measurement. Limiting strain data for strain paths #5 and #7 were taken from safe strains in the last frame before the specimen cracked. The conventional FLC's generated with the two different strain measurements are very close to each other, as the comparison in Figure 52 shows, which demonstrates that the DIC strain measurement can be processed to replicate and replace the conventional grid measurement and formability analysis.



a) FLC generated with grid measurements



b) FLC generated with a DIC strains to replace grid measurements

Figure 51 – Conventional FLC of the TRIP780 determined by the Keeler method

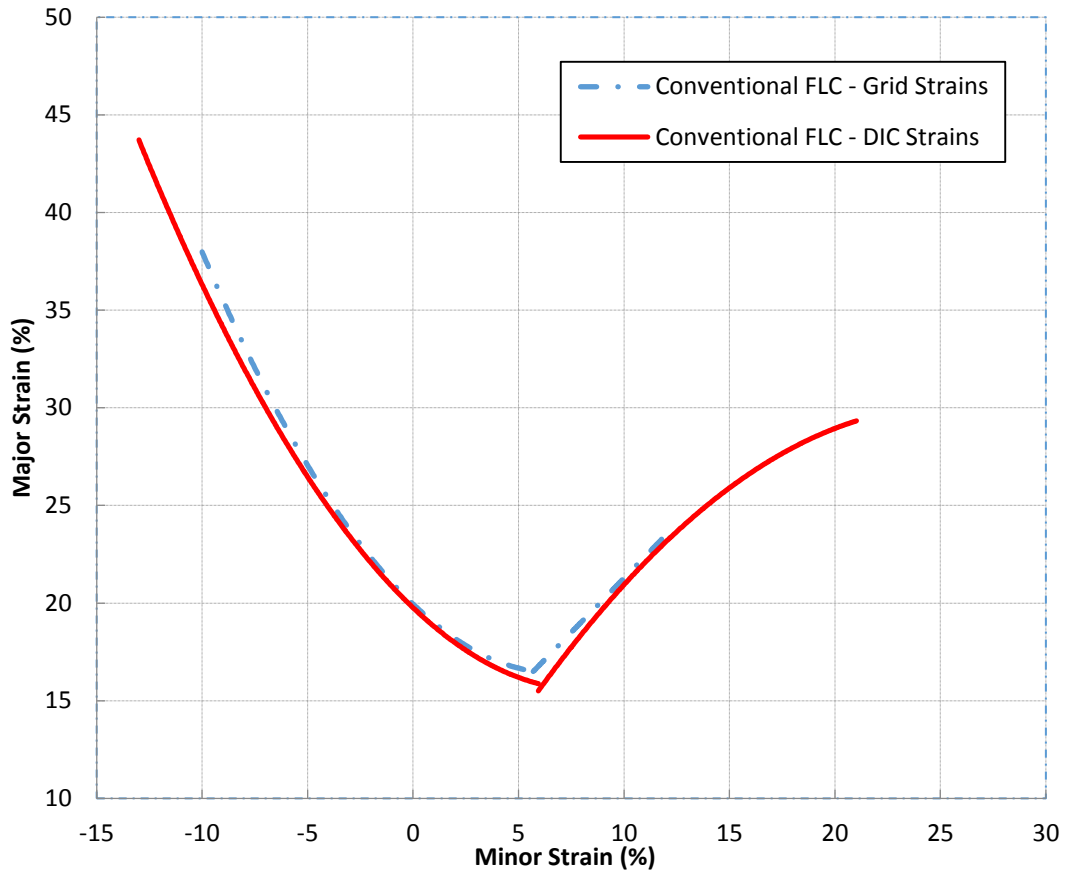


Figure 52 – Comparison of FLC's for TRIP780 obtained using different strain measurements

The FLC obtained with DIC strain measurements and the surface-slope necking criterion is shown in Figure 53. It is observed that the cluster for strain path #2 is relatively low on the plot when compared to the conventional Keeler FLC (Figure 53 compared to Figure 51a/b). Due to the small gauge area on the specimen, strain path #2 is the most sensitive to misalignments with the top of the punch, and may induce experimental errors. The right-hand side of the FLC is also populated with some valid data from safe strains measured in the last frame before fracture, similar to Figure 51b). It is worth noting that the star symbols on the plot come from the last strain state of a specimen without

fracture; these safe data points are not used to determine the FLC, and are only shown for reference.

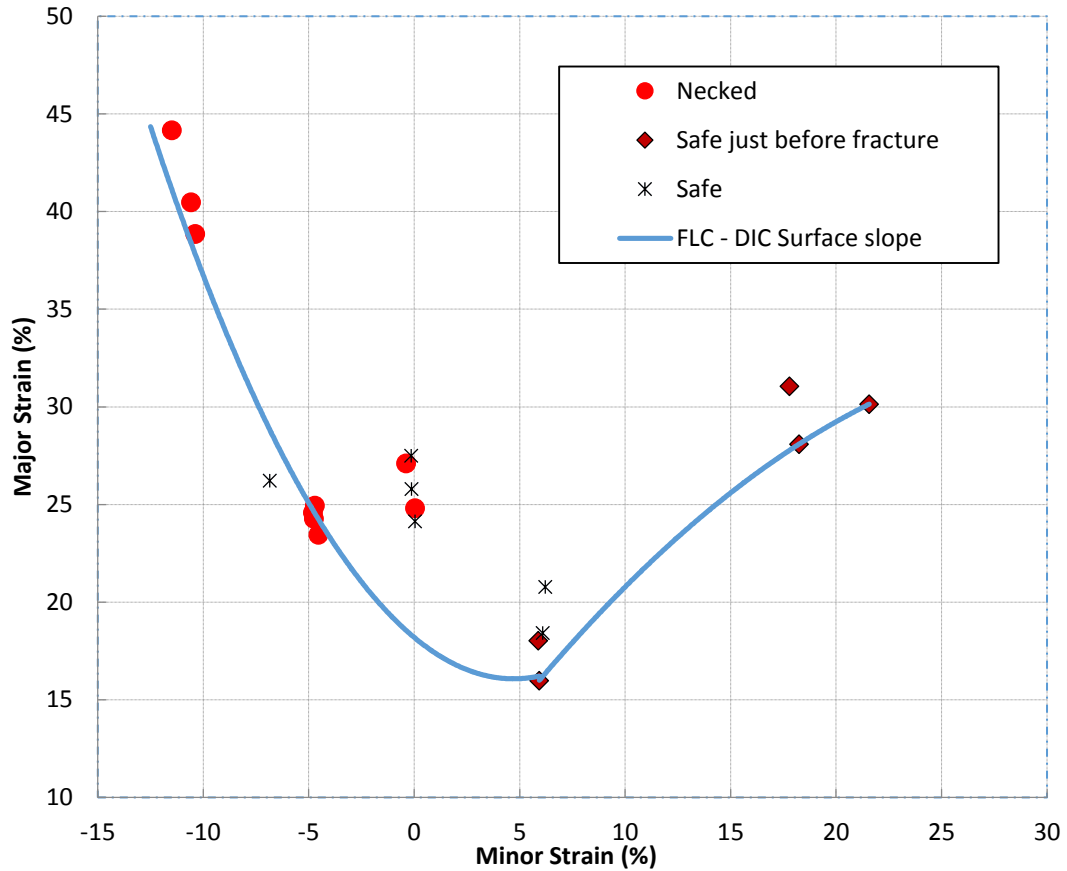


Figure 53 – FLC of TRIP780 generated with the surface-slope criterion

The FLC created with strain rate-departure criterion is shown in Figure 54. This plot more closely resembles the plot from the SGA method on the left-hand side, where the forming limit strains on the right hand side are essentially identical to previously created FLC's. Figure 55 has four FLC's on the same plot: a conventional FLC determined from grid measurements, a conventional FLC determined from DIC strain, an FLC determined from DIC strains with the surface slope criterion, and an FLC determined from DIC strains with the strain-rate departure criterion. Based on the comparison, the strain rate-

departure criterion produces forming limit strains that best conform to the conventional Keeler FLC.

As shown in the FLC's in Figure 53 and Figure 54, it is obvious that the FLC is shifted in the minor strain domain, since the lowest point on the curve is to the right of the major strain axis. This is due to the nature of the Nakazima test which inevitably leads to bending and stretching in the minor strain direction. More specifically, the curvature (bending) effect, the non-linear strain paths and the through-thickness contact stress are the factors that cause the shift of the FLC.

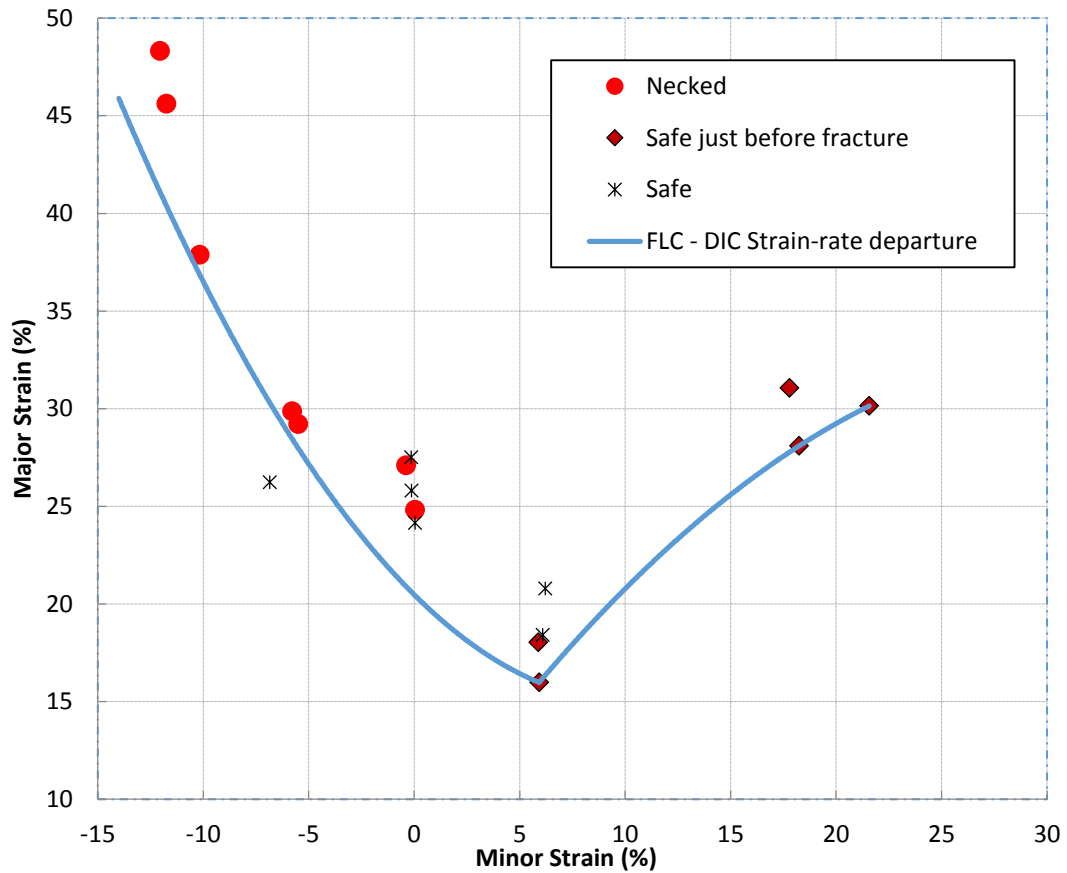


Figure 54 – FLC of TRIP780 generated with the strain-rate departure criterion

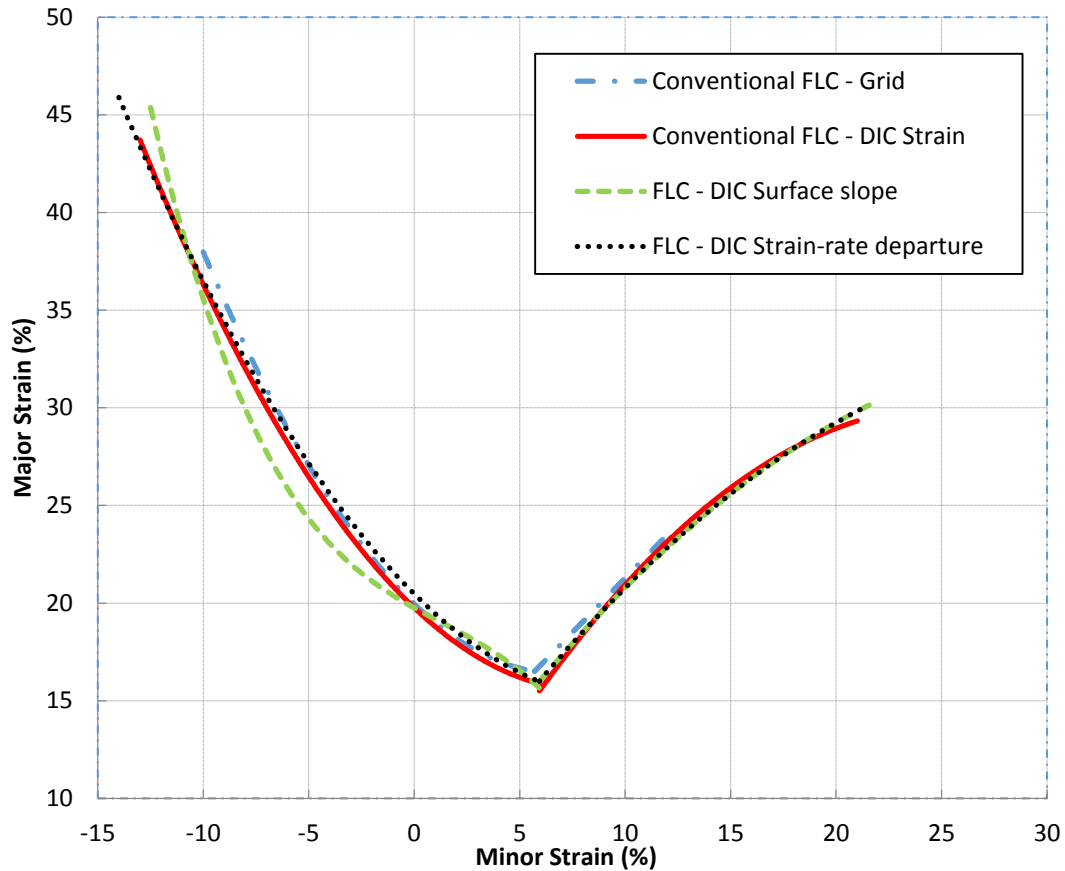


Figure 55 – Comparison of FLC's for TRIP780 obtained using different analysis methods

Figure 56 and Figure 57 show the FLC with all three compensations on the forming limit strains for process-dependent effects, for results from both the surface slope and the strain rate departure necking criterion. Since the strain-rate departure criterion appears to be better based on uncompensated results, the FLC shown in Figure 57 is the final FLC for the TRIP780 material. The compensated FLC based on the surface slope criterion seems to amplify the errors in strain path #2. A possible reason for this is the neglected elastic strain, which is significant when the minor strain is small. The FLC is approximated with a straight line on the right-hand side, due to the lack of data. One interesting observation is that correction applied to the stain data for strain path #5 brings up the limiting strain before fracturing, so it is now higher or equal to the strain in the area of the most severe

strain captured by DIC. As shown in Figure 56 and Figure 57, compared to Figure 53 and Figure 54, the limiting strain data for strain path #5 have increased in the major strain direction after correction. This supports the previous hypothesis that the presence of a through-thickness contact stress suppresses the formation of necking. It is also observed that the limiting strain data for most strain paths have translated on the minor strain axis, causing undesired deviations from the initially intended strain paths. The determined final FLC is shown in Figure 57, with the piece-wise curves defined in Equation 5.1 through Equation 5.4, and the lowest point on the non-compensated and compensated FLC located at [5.9, 16.0] and [2.5, 15.7], respectively. The FLC determined with DIC strain and strain-rate departure criterion was validated against the conventional FLC determined with Keeler’s method using Equation 3.1 and Equation 3.2. The calculated validation metric and the accumulated error are 0.987 and 0.0325, respectively.

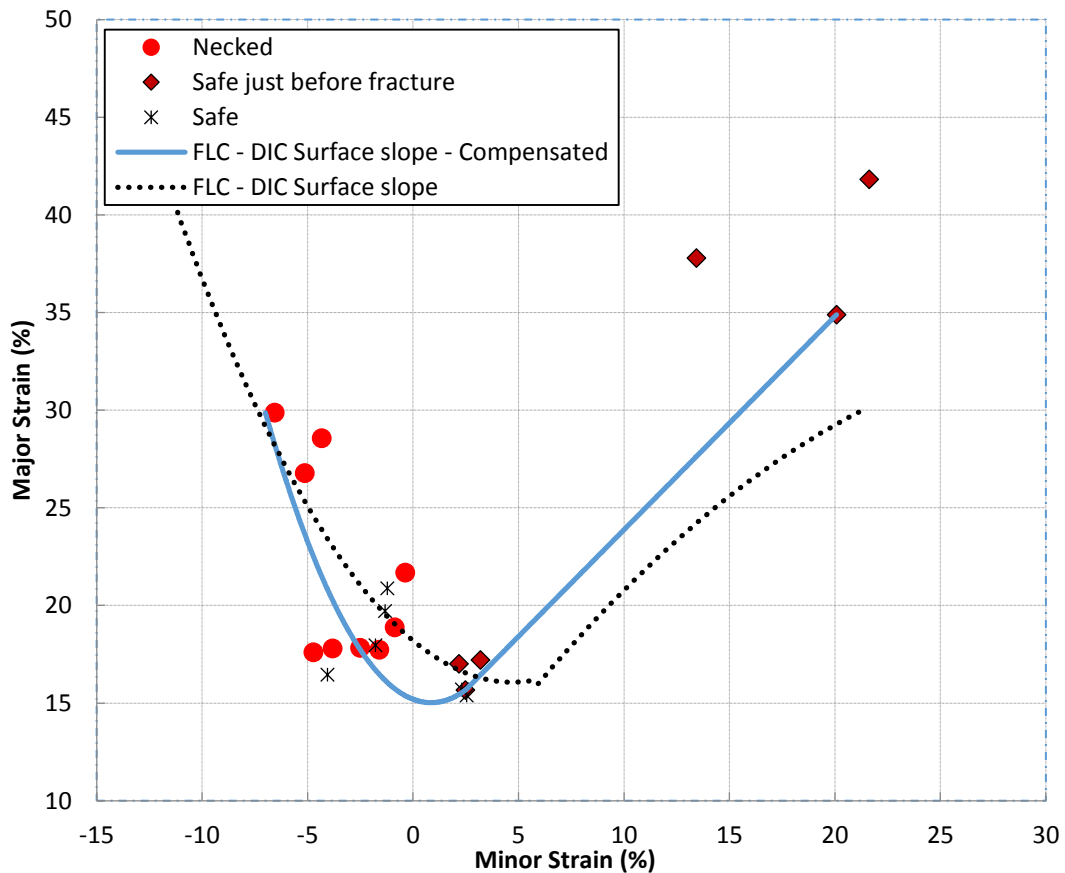


Figure 56 – FLC of TRIP780 generated with the surface-slope criterion (compensated)

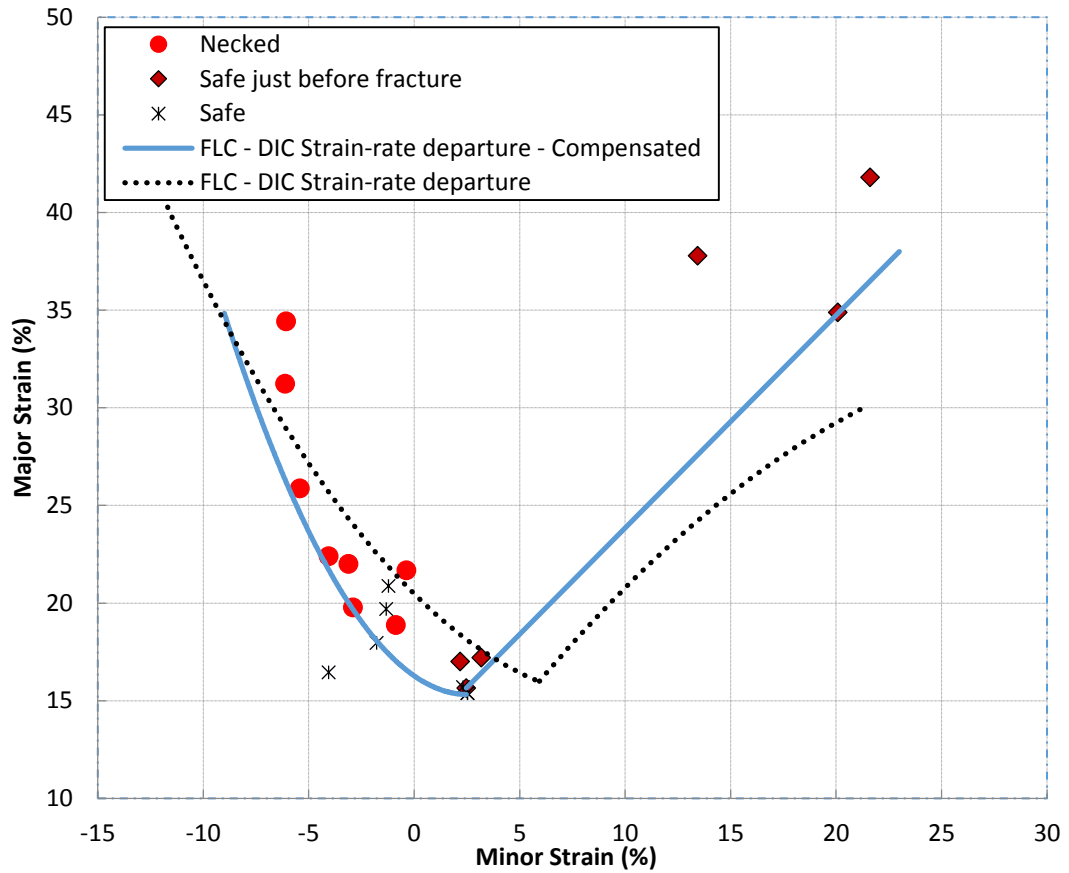


Figure 57 – FLC of TRIP780 generated with the strain-rate departure criterion (compensated)

$y \Rightarrow$  major strain,  $x \Rightarrow$  minor strain

$L \Rightarrow$  left hand side,  $R \Rightarrow$  right hand side

$$y_L = 0.053x^2 - 1.0728x + 20.475 \quad (5.1)$$

$$y_R = 0.235x^2 + 1.5503x + 7.6234 \quad (5.2)$$

$$y_{L,Compensated} = 0.146x^2 - 0.7483x + 16.274 \quad (5.3)$$

$$y_{R,Compensated} = 1.0887x + 12.959 \quad (5.4)$$



## 6. Conclusions, Recommendations and Future Work

Consistent with the objectives of this thesis, the work hardening behaviour and the forming limit of the TRIP780 sheet material were experimentally determined. With strains measured using both DIC and conventional grid analysis, it has been shown that DIC is a very reliable strain measurement technique, and is capable of replacing the conventional grid measurement. The experimental method which prestrains the sheet by flat rolling before the tensile tests enable us to extend the flow curve of the material from about 0.2 mm/mm to above 1 mm/mm strain. The extended flow curve will help improve the robustness of the FE simulations, since experimental data is more dependable than extrapolating a flow curve for beyond its domain.

A robust and highly-automated post-processing software was created to determine the experimental forming limit for each Nakazima test. While the post processing software may need further modifications as a result of analyzing the forming limits for a range of different sheet materials, the strain-rate departure criterion produced forming limit strains that best conformed to the FLC obtained by the Keeler method. Some tests were conducted with the punch speed changed during the test, and these were difficult to analyze with this criterion, because it is time-dependent and sensitive to loading rate. The surface slope criterion presents some errors in the negative minor strain range, which may be a result of specimen geometry and misalignment with the punch. However, the criterion is insensitive to loading rate.

The process-dependent correction algorithm proposed by Min et al. [33] generally led to improved results by eliminating the effects of bending, NLSP and non-negligible contact stress in the Nakazima test. While the correction of the limit strain data obtained with the surface slope criterion led to some questionable FLC results, the compensation for the strain-rate departure criterion yielded good results.

Overall, a robust and process-independent procedure was created for determining the FLC for sheet metals, including experimental testing, data post-processing and compensation.

It is worth noting that it might be impossible to determine the necking limit for this particular grade of TRIP780 steel for positive minor strains beyond 5%, since no necked specimen could be produced for these biaxial stretch conditions.

For further development, additional necking criteria should be examined, with different grades of materials, to ensure a particular method is generally applicable to a range of sheet metals. A more complex Barlat material model, and a better hardening model could be implemented in simulations and experimental process-dependent corrections, to better represent the anisotropy of the material, and to properly calculate the experimental elastic strain. Marciniak tests with a flat punch would also generate more ideal plane-stress loading conditions and would be useful to verify the forming limits experimentally determined using the Nakazima test. The specimen geometries may also be further optimized to produce strain paths that are more linear. The compensation of process-dependent effects for Nakazima tests was found to decrease the value of the minor strain and thereby shift the FLC to the left. Therefore, if the FLC with process-dependent correction is to be used for the final FLC, the geometry of the various specimens should be modified to offset the shift in minor strain.

## Bibliography

- [1] UltraLight Steel Auto Body Consortium, “UltraLight Steel Auto Body Final Engineering Report,” Southfield, Michigan, 1998.
- [2] R. Sierra and J. A. Nemes, “Investigation of the mechanical behaviour of multi-phase TRIP steels using finite element methods,” *Int. J. Mech. Sci.*, vol. 50, no. 4, pp. 649–665, 2008.
- [3] M. Bhargava, A. Tewari, and S. K. Mishra, “Forming limit diagram of Advanced High Strength Steels (AHSS) based on strain-path diagram,” *Mater. Des.*, vol. 85, pp. 149–155, 2015.
- [4] S. Keeler and W. A. Backofen, “Plastic instability and fracture in sheets stretched over rigid punches,” *Asm Trans Q*, vol. 56, no. 1, pp. 25–48, 1963.
- [5] R. Brannon, “Define Your Strain.” University of Utah, 2000.
- [6] W. T. Lankford, S. C. Snyder, and J. A. Bauscher, “New criteria for predicting the press performance of deep drawing sheets,” *Thirty-first Annu. Conv. Soc.*, vol. 42, pp. 1–28, 1949.
- [7] R. Hill, “A theory of the yielding and plastic flow of anisotropic metals,” *Proc. R. Soc. London A Math. Phys. Eng. Sci.*, vol. 193, no. 1033, pp. 281–297, 1948.
- [8] R. Hill, “Constitutive modelling of orthotropic plasticity in sheet metals,” *J. Mech. Phys. Solids*, vol. 38, no. 3, pp. 405–417, 1990.
- [9] F. Barlat and K. Lian, “Plastic behavior and stretchability of sheet metals. Part I: A yield function for orthotropic sheets under plane stress conditions,” *Int. J. Plast.*, vol. 5, no. 1, pp. 51–66, 1989.

- [10] ASTM International, “Standard Test Methods for Tension Testing of Metallic Materials,” no. E8/E8M – 09. ASTM International, West Conshohocken, PA, 2009.
- [11] M. Vasilescu, “Development of a Hydraulic Bulge Test to Determine the Work Hardening Behaviour of Sheet Materials,” MSc Thesis, University of Windsor, Canada, 2016.
- [12] J. G. Sevillano, P. Van Houtte, and E. Aernoudt, “Large Strain Work Hardening and Textures,” *Prog. Mater. Sci.*, vol. 25, pp. 77–79, 1981.
- [13] ASTM International, “Standard Test Method for Shear Testing of Thin Aluminum Alloy Products,” vol. 64, no. Reapproved. pp. 4–6, 1998.
- [14] M. S. A. Sarker, “Development of a Shear Test to Determine the Cyclic Behaviour of Sheet Materials,” MSc Thesis, University of Windsor, Canada, 2011.
- [15] B. Zillmann, T. Clausmeyer, S. Bargmann, T. Lampke, M. F. Wagner, and T. Halle, “Validation of Simple Shear Tests for Parameter Identification Considering the Evolution of Plastic Anisotropy,” *Tech. Mech.*, vol. 32, no. 2–5, pp. 622–630, 2012.
- [16] C. W. Koh, “Design of a Hydraulic Bulge Test Apparatus,” MSc Thesis, Massachusetts Institute of Technology, 2008.
- [17] G. Gutscher, H. C. Wu, G. Ngaile, and T. Altan, “Determination of flow stress for sheet metal forming using the viscous pressure bulge (VPB) test,” *J. Mater. Process. Technol.*, vol. 146, no. 1, pp. 1–7, 2004.
- [18] P. Ludwik, *Elemente der technologischen Mechanik*. Springer-Verlag, 2013.
- [19] J. H. Hollomon, “Tensile Deformation,” *Met. Technology*, vol. 12, no. 4, pp. 268–290, 1945.

- [20] G. R. Johnson and W. H. Cook, "A constitutive model and data for metals subjected to large strains, high strain rates and high temperatures," in *7th International Symposium on Ballistics*, 1983, pp. 541–547.
- [21] A. S. Khan and R. Liang, "Behaviors of three BCC metal over a wide range of strain rates and temperatures: Experiments and modeling," *Int. J. Plast.*, vol. 15, no. 10, pp. 1089–1109, 1999.
- [22] C. M. Tamarelli, "AHSS 101 the evolving use of advance high-strength steel for automotive applications," Southfield, MI, 2011.
- [23] D. Green, J. Samei, A. Hasannejadasl, A. Jenab, and I. Sari Sarraf, "Metal Forming Processes Research - APC Project (EHF)," 2012. [Online]. Available: <https://web2.uwindsor.ca/apc-ehf/index.html>. [Accessed: 25-Jul-2015].
- [24] S. Keeler, M. Kimchi, R. Kuziak, R. Kawakka, S. Waengler, Y. Weng, H. Dong, and Y. Gan, "Advanced high strength steels for automotive industry," *Arch. Civ. Mech. Eng.*, vol. 8, no. 2, p. 511, 2014.
- [25] C. Cayron, "One-step theory of fcc-bcc martensitic transformation," *Acta Crystallogr.*, vol. A69, no. January, pp. 1–46, 2013.
- [26] E. C. Bain, "The nature of martensite," *Trans. Am. Inst. Min. Metall. Eng.*, vol. 70, no. 1921, pp. 25–46, 1924.
- [27] A. Gilbert and L. Hobrough, "Obituary," *Photogramm. Rec.*, vol. 18, no. 104, pp. 337–340, 2003.
- [28] M. A. Sutton, J. Orteu, and H. W. Schreier, "Three-Dimensional Digital Image Correlation Measurements, 2000–Present," in *Image Correlation for Shape, Motion and Deformation Measurements*, New York, NY: Springer US, 2009, pp. 8–10.

- [29] Correlated Solutions, “Digital Image Correlation : Overview of Principles and Software 2D Image Correlation Fundamentals,” in *South Carolina University*, 2009.
- [30] ASTM International, “Standard Test Method for Determining Forming Limit Curves,” vol. E2218 – 15. ASTM International, West Conshohocken, PA, 2015.
- [31] K. Nakazima, T. Kikuma, and K. Hasuka, “Study on the formability of steel sheets,” *Yawata Tech Rep, Sept.*, no. 264, pp. 8517–8530, 1968.
- [32] International Organization for Standardization, “Metallic materials — Sheet and strip — Determination of forming-limit curves — Part 2: Determination of forming-limit curves in the laboratory,” vol. 12004–2. International Organization for Standardization, Geneva, Switzerland, 2008.
- [33] J. Min, T. B. Stoughton, J. E. Carsley, and J. Lin, “Compensation for process-dependent effects in the determination of localized necking limits,” *Int. J. Mech. Sci.*, vol. 117, pp. 115–134, 2016.
- [34] Z. Marciniak and K. Kuczyński, “Limit strains in the processes of stretch-forming sheet metal,” *Int. J. Mech. Sci.*, vol. 9, no. 9, pp. 609–620, 1967.
- [35] A. Bragard, J.-C. Baret, and H. Bonnarens, “Simplified Technique to Determine the FLD on the Onset of Necking,” *C. R. M.*, no. 33, pp. 53–63, 1972.
- [36] A. J. Martinez-Donaire, F. J. Garcia-Lomas, and C. Vallellano, “New approaches to detect the onset of localised necking in sheets under through-thickness strain gradients,” *Mater. Des.*, vol. 57, pp. 135–145, 2014.
- [37] C. Zhang, L. Leotoing, G. Zhao, D. Guines, and E. Ragneau, “A comparative study of different necking criteria for numerical and experimental prediction of FLCs,” *J. Mater. Eng. Perform.*, vol. 20, no. 6, pp. 1036–1042, 2011.

- [38] K. Wang, J. E. Carsley, B. He, J. Li, and L. Zhang, "Measuring forming limit strains with digital image correlation analysis," *J. Mater. Process. Technol.*, vol. 214, no. 5, pp. 1120–1130, 2014.
- [39] C. Zhang, L. Leotoing, D. Guines, and E. Ragneau, "Theoretical and numerical study of strain rate influence on AA5083 formability," *J. Mater. Process. Technol.*, vol. 209, no. 8, pp. 3849–3858, 2009.
- [40] V. Savic, L. G. Hector Jr, and J. R. Fekete, "Digital Image Correlation Study of Plastic Deformation and Fracture in Fully Martensitic Steels," *Exp. Mech.*, vol. 50, no. 1, pp. 99–110, 2010.
- [41] M. R. Tharrett and T. B. Stoughton, "Stretch-bend forming limits of 1008 AK steel," *SAE Tech. Pap.*, no. 2003-01-1157, 2003.
- [42] T. B. Stoughton and J. W. Yoon, "A new approach for failure criterion for sheet metals," *Int. J. Plast.*, vol. 27, no. 3, pp. 440–459, 2011.
- [43] K. S. Raghavan, "A simple technique to generate in-plane forming limit curves and selected applications," *Metall. Mater. Trans. A*, vol. 26, no. 8, pp. 2075–2084, 1995.
- [44] W. L. Oberkampf and T. G. Trucano, "Verification and validation in computational fluid dynamics," *Prog. Aerosp. Sci.*, vol. 38, no. 3, pp. 209–272, 2002.
- [45] J. Luo, "Smooth Differentiation - File Exchange - MATLAB Central," 2004.  
[Online]. Available:  
<https://www.mathworks.com/matlabcentral/fileexchange/6170-smooth-differentiation>. [Accessed: 26-Sep-2016].
- [46] J. M. Imbert, M. J. Worswick, and S. Golovashchenko, "Contributing factors to the

increased formability observed in electromagnetically formed aluminum alloy sheet,” *Proc. 2nd Int. Conf. High Speed Form.*, no. May 2015, pp. 3–12, 2006.



## Appendix

### Appendix A - Rolling and Tensile Test



Figure 58 – the Flat Roller, the EDM tensile specimen and the tensile test setup

## Appendix B – Reduced Keyword Input

LS-DYNA Keyword file created by LS-PrePost(R) V4.3 (Beta) - 17Jan2016(11:00)

Created on May-26-2016 (00:52:37)

\*KEYWORD

\*TITLE

LS-DYNA keyword deck by LS-PrePost

\*CONTROL\_ACCURACY

osu inn pidosu iacc  
0 2 0 0

\*CONTROL\_CONTACT

slsfac rwpnal islchk shlthk penopt thkchg orien enmass  
0.1 0.0 2 1 5 1 2 0  
usrstr usrfrc nsbcs interm xpene ssthk ecdt tiedprj  
0 0 10 0 4.0 1 0 0  
sfric dfrc edc vfc th th\_sf pen\_sf  
0.0 0.0 0.0 0.0 0.0 0.0 0.0  
ignore frceng skiprwg outseg spotstp spotdel spothin  
2 1 0 0 0 0 0.0  
isym nserod rwgaps rwgdth rwksf icov swradf ithoff  
0 0 1 0.0 1.0 0 0.0 0  
shledg pstiff ithcnt tdcnof ftall unused shltrw  
0 0 0 0 0 0.0

\*CONTROL\_ENERGY

hgen rwen slnten rylen  
2 1 2 2

\*CONTROL\_HOURLASS

ihq qh  
8 0.1

\*CONTROL\_IMPLICIT\_AUTO

iauto iteopt itewin dtmin dtmax dtexp kfail kcycle  
0 0 0 0.0 0.0 0.0 0 0

\*CONTROL\_IMPLICIT\_GENERAL

imflag dt0 imform nsbs igs cnstn form zero\_v  
1 0.05 2 0 2 0 0 0

\*CONTROL\_IMPLICIT\_SOLUTION

nsolvr ilimit maxref dctl ectol rctl lstol abstol  
5 0 0 0.0 0.0 0.0 0.01.0000E-10  
dnorm diverg istif nlprint nlnorm d3itctl cpchk  
2 1 0 1 4 0 1  
arcctl arcdir arclen arcmth arcdmp arcpsi arcalf arctim  
0 0 0.0 1 1 0 0 0  
lsmt d lsdire rad srade awgt sred  
5 2 0.0 0.0 0.0 0.0

\*CONTROL\_IMPLICIT\_SOLVER

lsolvr lprint negev order drcm drcprm autospc autotol  
5 3 2 0 4 0.0 1 0.0

lcpack mtxdmp  
2 0

\*CONTROL\_SHELL

wrpang esort irnxx istupd theory bwc miter proj  
20.0 1 -1 4 16 2 2 0  
rotascl intgrd lamsht cstyp6 tshell

```

1.0  0  0  1  0
$# psstupd sidt4tu cntco itsflg irqquad
0  0  1  0  2
$# nfail1 nfail4 psnfail keepsc delfr drcpsid drcprm
0  0  0  0  0  0  1.0
*CONTROL_SOLUTION
$# soln nlq isnan lcint
0  0  1  100
*CONTROL_TERMINATION
$# endtim endcyc dtmin endeng endmas
100.0  0  0.0  0.01.000000E8
*DATABASE_DEFGE0
$# dt binary lcur ioopt
0.05  0  0  1
*DATABASE_ELOUT
$# dt binary lcur ioopt option1 option2 option3 option4
0.05  0  0  1  0  0  0  0
*DATABASE_GCEOUT
$# dt binary lcur ioopt
0.05  0  0  1
*DATABASE_GLSTAT
$# dt binary lcur ioopt
0.05  0  0  1
*DATABASE_GLSTAT_MASS_PROPERTIES
$# dt binary lcur ioopt
0.05  0  0  1
*DATABASE_MATSUM
$# dt binary lcur ioopt
0.05  0  0  1
*DATABASE_NCFORC
$# dt binary lcur ioopt
0.05  0  0  1
*DATABASE_RBDOUT
$# dt binary lcur ioopt
0.05  0  0  1
*DATABASE_RCFORC
$# dt binary lcur ioopt
0.05  0  0  1
*DATABASE_SLEOUT
$# dt binary lcur ioopt
0.05  0  0  1
*DATABASE_SPCFORC
$# dt binary lcur ioopt
0.05  0  0  1
*DATABASE_BINARY_D3PLOT
$# dt lcdt beam npltc psetid
0.5  0  0  0  0
$# ioopt
0
*DATABASE_EXTENT_BINARY
$# neiph neips maxint strflg sigflg epsflg rltflg engflg
0  5  5  111  1  1  1  1
$# cmpflg ieverp beamip dcomp shge stssz n3thdt ialemat
1  0  0  1  2  3  2  1
$# nintslid pkp_sen sclp hydro msscl therm intout nodout

```

```

0 0 1.0 0 0 0ALL ALL
$# dtdt resplt neipb
0 0 0
*DATABASE_HISTORY_SHELL_SET
$# id1 id2 id3 id4 id5 id6 id7 id8
1 2 3 0 0 0 0 0
*BOUNDARY_PRESCRIBED_MOTION_RIGID
$# pid dof vad lcid sf vid death birth
1 3 2 10.41999999 01.00000E28 0.0
*BOUNDARY_SPC_SET_ID
$# id heading
1Die Fix
$# nsid cid dofx dofy dofz dofrx dofry dofrz
1 0 1 1 1 1 1 1
*BOUNDARY_SPC_SET_ID
$# id heading
2Specimen Fix
$# nsid cid dofx dofy dofz dofrx dofry dofrz
2 0 1 1 1 1 1 1
*SET_NODE_LIST_TITLE
Spec Fix
$# sid da1 da2 da3 da4 solver
2 0.0 0.0 0.0 0.0MECH
$# nid1 nid2 nid3 nid4 nid5 nid6 nid7 nid8
41009 41034 41036 41038 41040 41042 41044 41046
41048 41050 41052 41054 41056 41058 41060 41062
41064 41066 41068 41070 41072 41074 41076 41078
41080 41082 41084 41086 41088 41090 41092 0
*BOUNDARY_SPC_SET_ID
$# id heading
3Specimen XZ
$# nsid cid dofx dofy dofz dofrx dofry dofrz
3 0 0 1 0 1 0 1
*SET_NODE_LIST_TITLE
Spec XZ
$# sid da1 da2 da3 da4 solver
3 0.0 0.0 0.0 0.0MECH
$# nid1 nid2 nid3 nid4 nid5 nid6 nid7 nid8
39490 39569 39571 39573 39575 39577 39579 39581
39583 39585 39587 39589 39591 39593 39595 39597
39599 39601 39603 39605 39607 39609 39611 39613
39615 39617 0 0 0 0 0 0
*BOUNDARY_SPC_SET_ID
$# id heading
4Specimen YZ
$# nsid cid dofx dofy dofz dofrx dofry dofrz
4 0 1 0 0 0 1 1
*SET_NODE_LIST_TITLE
Spec YZ
$# sid da1 da2 da3 da4 solver
4 0.0 0.0 0.0 0.0MECH
$# nid1 nid2 nid3 nid4 nid5 nid6 nid7 nid8
39489 39491 39493 39495 39497 39499 39501 39503
39505 39507 39509 39511 39513 39515 39517 39519
39521 39523 39525 39527 39529 39531 39533 39535

```

```

39537 39539 39541 39543 39545 39547 39549 39551
39553 39555 39557 39559 39561 39563 39565 39567
39569 40555 40556 40557 40558 40559 40560 40561
40562 40563 40564 40565 40566 40567 40568 40569
41009 41011 41013 41015 41017 41019 41021 41023
41025 41027 41029 41031 0 0 0 0
*BOUNDARY_SPC_SET_ID
$# id heading
5Punch Restrain
$# nsid cid dofx dofy dofz dofrx dofry dofrz
5 0 1 1 0 1 1 1
*SET_NODE_LIST_TITLE
Punch Res
$# sid da1 da2 da3 da4 solver
5 0.0 0.0 0.0 0.0 0.0MECH
$# nid1 nid2 nid3 nid4 nid5 nid6 nid7 nid8
29525 29606 0 0 0 0 0 0
*CONTACT_FORMING_SURFACE_TO_SURFACE_MORTAR_ID
$# cid title
1Contact Punch-specimen
$# ssid msid sstyp mstyp sboxid mboxid spr mpr
4 1 3 3 0 0 1 1
$# fs fd dc vc vdc penchk bt dt
0.05 0.04 1000.0 0.0 0.0 1 0.01.00000E20
$# sfs sfm sst mst sfst sfmt fsf vsf
1.0 1.0 0.0 0.0 1.0 1.0 1.0 1.0
$# soft sofsc1 lc1dab maxpar sbopt depth bsort frcfreq
0 0.1 0 1.025 2.0 2 0 1
$# penmax thkopt shlthk snlog isym i2d3d sldthk sldstf
0.0 0 0 0 0 0 0.0 0.0
$# igap ignodprfac/mpadtstif/mpar2 unused unused flang1 cid_rcf
1 3 0.0 0.0 0.0 0
*CONTACT_FORMING_SURFACE_TO_SURFACE_MORTAR_ID
$# cid title
2Contact UpperDie-specimen
$# ssid msid sstyp mstyp sboxid mboxid spr mpr
4 2 3 3 0 0 1 1
$# fs fd dc vc vdc penchk bt dt
0.05 0.04 1000.0 0.0 0.0 1 0.01.00000E20
$# sfs sfm sst mst sfst sfmt fsf vsf
1.0 1.0 0.0 0.0 1.0 1.0 1.0 1.0
$# soft sofsc1 lc1dab maxpar sbopt depth bsort frcfreq
0 0.1 0 1.025 2.0 2 0 1
$# penmax thkopt shlthk snlog isym i2d3d sldthk sldstf
0.0 0 0 0 0 0 0.0 0.0
$# igap ignodprfac/mpadtstif/mpar2 unused unused flang1 cid_rcf
1 3 0.0 0.0 0.0 0
*CONTACT_FORMING_SURFACE_TO_SURFACE_MORTAR_ID
$# cid title
3Contact LowerDie-specimen
$# ssid msid sstyp mstyp sboxid mboxid spr mpr
4 3 3 3 0 0 1 1
$# fs fd dc vc vdc penchk bt dt
0.05 0.04 1000.0 0.0 0.0 1 0.01.00000E20
$# sfs sfm sst mst sfst sfmt fsf vsf

```

```

1.0 1.0 0.0 0.0 1.0 1.0 1.0 1.0
$# soft soffscl lcidab maxpar sbopt depth bsort frcfrq
0 0.1 0 1.025 2.0 2 0 1
$# penmax thkopt shlthk snlog isym i2d3d sldthk sldstf
0.0 0 0 0 0 0 0.0 0.0
$# igap ignodprfac/mpadtstif/mpar2 unused unused flangl cid_rcf
1 3 0.0 0.0 0.0 0
*PART
$# title
Punch
$# pid secid mid eosid hgid grav adpopt tmid
1 1 7806 0 0 0 0 0
*SECTION_SHELL
$# secid elform shrf nip propt qr/irid icompl setyp
1 2 1.0 2 1.0 0 0 1
$# t1 t2 t3 t4 nloc marea idof edgset
1.0 1.0 1.0 1.0 0.0 0.0 0.0 0
*PART
$# title
Die Upper
$# pid secid mid eosid hgid grav adpopt tmid
2 2 7806 0 0 0 0 0
*SECTION_SHELL
$# secid elform shrf nip propt qr/irid icompl setyp
2 2 1.0 2 1.0 0 0 1
$# t1 t2 t3 t4 nloc marea idof edgset
1.0 1.0 1.0 1.0 0.0 0.0 0.0 0
*PART
$# title
Die Lower
$# pid secid mid eosid hgid grav adpopt tmid
3 2 7806 0 0 0 0 0
*PART
$# title
Specimen
$# pid secid mid eosid hgid grav adpopt tmid
4 3 7803 0 0 0 0 0
*SECTION_SHELL
$# secid elform shrf nip propt qr/irid icompl setyp
3 160.83333331 5 1.0 0 0 1
$# t1 t2 t3 t4 nloc marea idof edgset
1.5 1.5 1.5 1.5 0.0 0.0 0.0 0
*DEFINE_CURVE_TITLE
Punch Displacement over Time
$# lcid sidr sfa sfo offa offo dattyp lcint
1 0 1.0 1.0 0.0 0.0 0 0
$# a1 o1
0.0 0.0
8000.0 8000.0
*SET_SHELL_LIST_TITLE
C
$# sid da1 da2 da3 da4
1 0.0 0.0 0.0 0.0
$# eid1 eid2 eid3 eid4 eid5 eid6 eid7 eid8
38400 0 0 0 0 0 0 0

```

\*SET\_SHELL\_LIST\_TITLE

X

\$# sid da1 da2 da3 da4

2 0.0 0.0 0.0 0.0

\$# eid1 eid2 eid3 eid4 eid5 eid6 eid7 eid8

38760 39120 39160 39200 39240 39280 39320 39360

38440 38480 38520 38560 38600 38640 38680 38720

38800 38840 38880 38920 38960 39000 39040 39080

\*SET\_SHELL\_LIST\_TITLE

Y

\$# sid da1 da2 da3 da4

3 0.0 0.0 0.0 0.0

\$# eid1 eid2 eid3 eid4 eid5 eid6 eid7 eid8

38361 38362 38363 39361 39396 39397 39398 39399

39400 39401 39402 39403 39404 39405 39406 39407

39408 39409 39776 39777 39778 39779 39780 39781

39782 39783 39784 39773 39774 39775 38364 38365

38366 38367 38368 38369 38370 38371 38372 38373

38374 38375 38376 38377 38378 38379 38380 38381

38382 38383 38384 38385 38386 38387 38388 38389

38390 38391 38392 38393 38394 38395 38396 38397

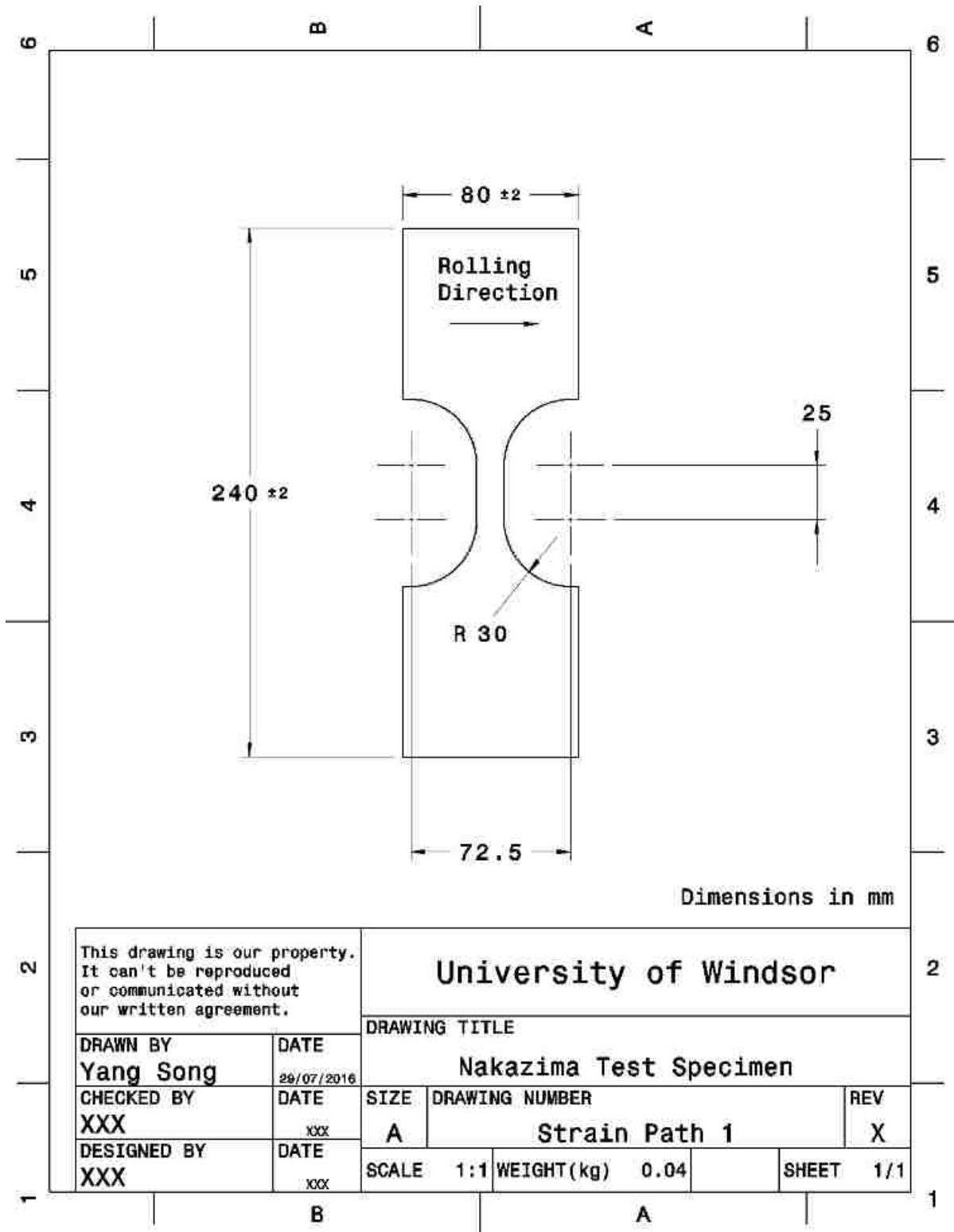
38398 38399 0 0 0 0 0 0

\*INCLUDE

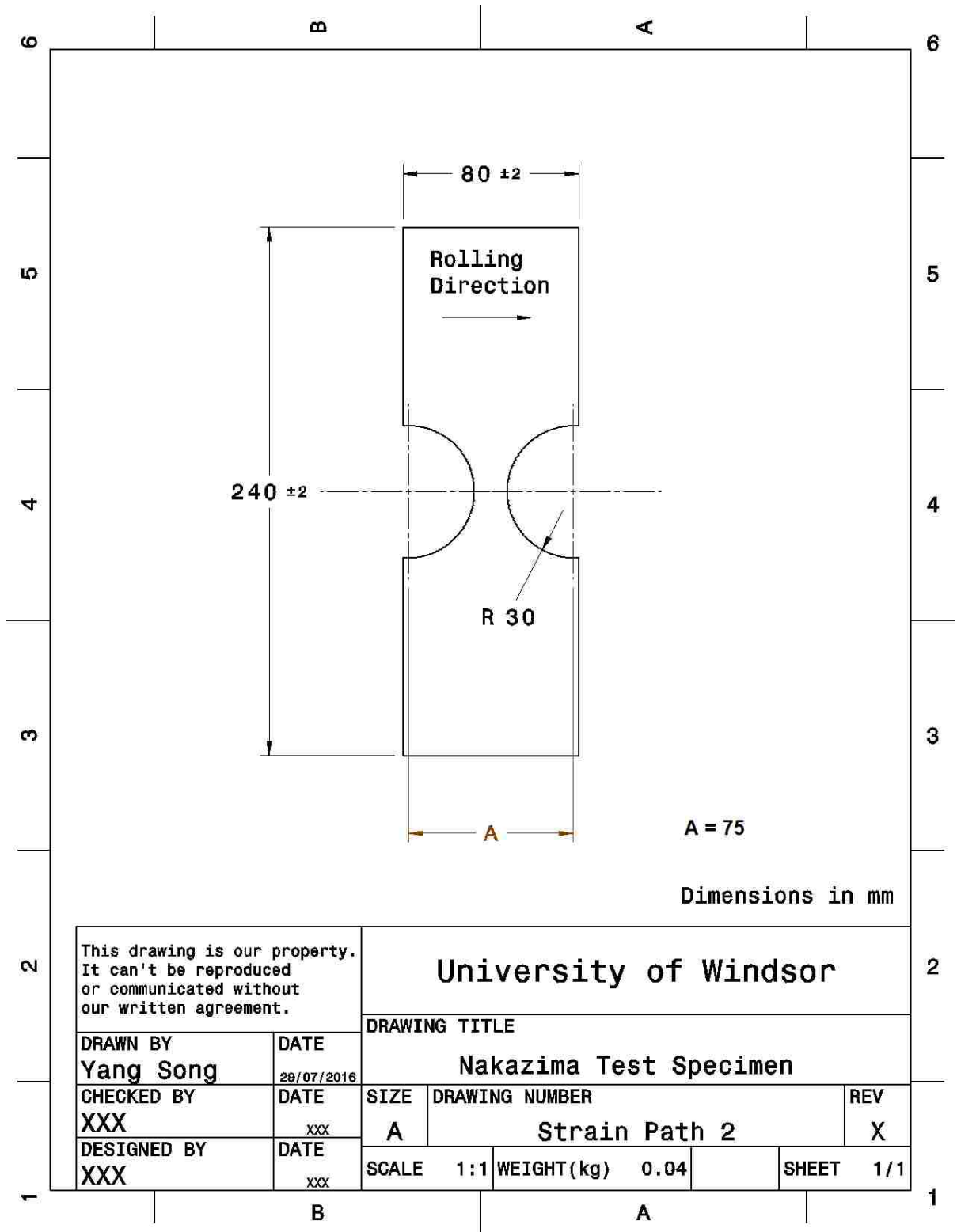
D:\Documents\grad\92-797\trip780 material\TRIP780.k

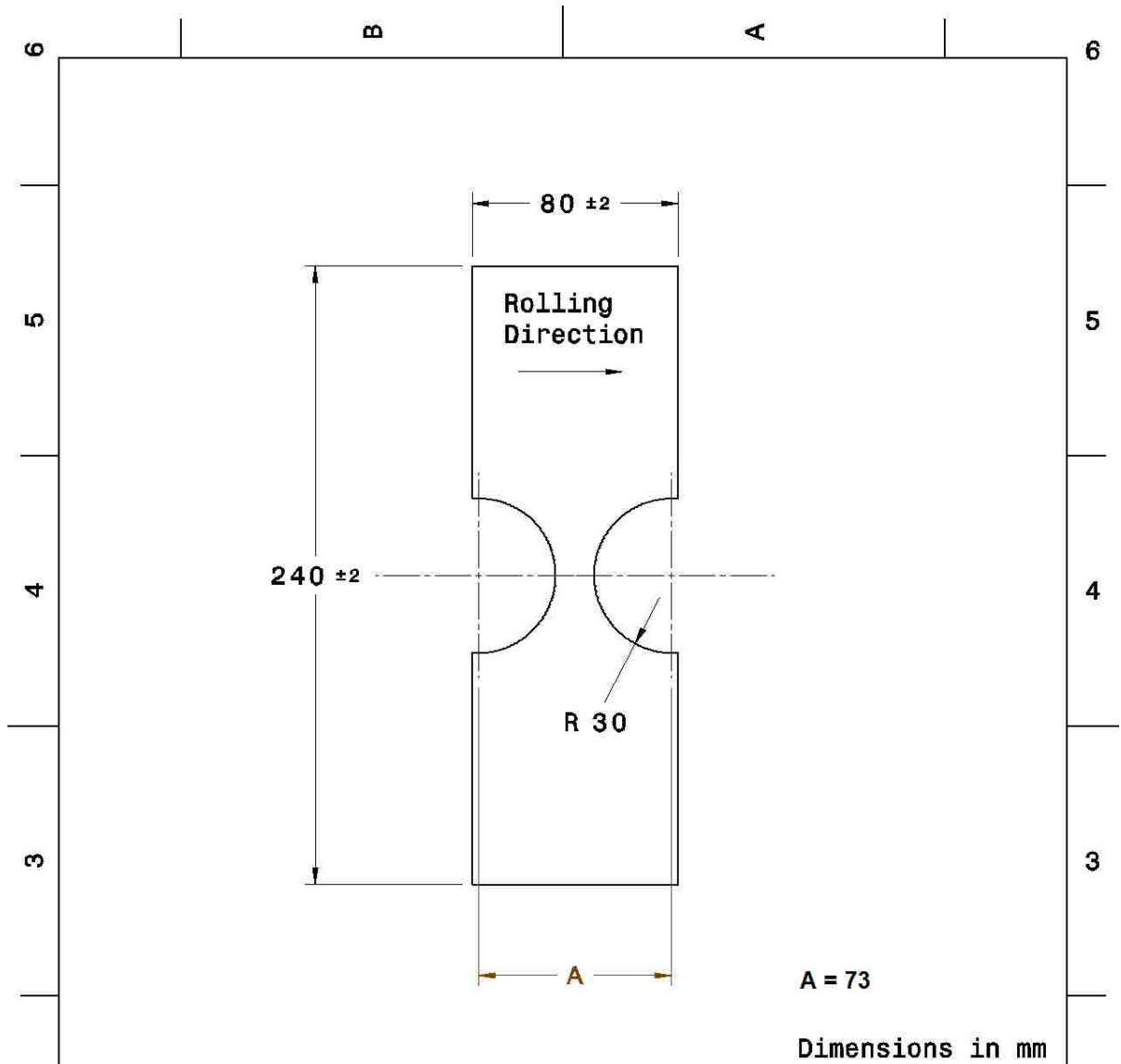
\*END

## Appendix C – Nakazima Specimen Geometries









This drawing is our property.  
It can't be reproduced  
or communicated without  
our written agreement.

## University of Windsor

DRAWN BY <b>Yang Song</b>	DATE 29/07/2016
------------------------------	--------------------

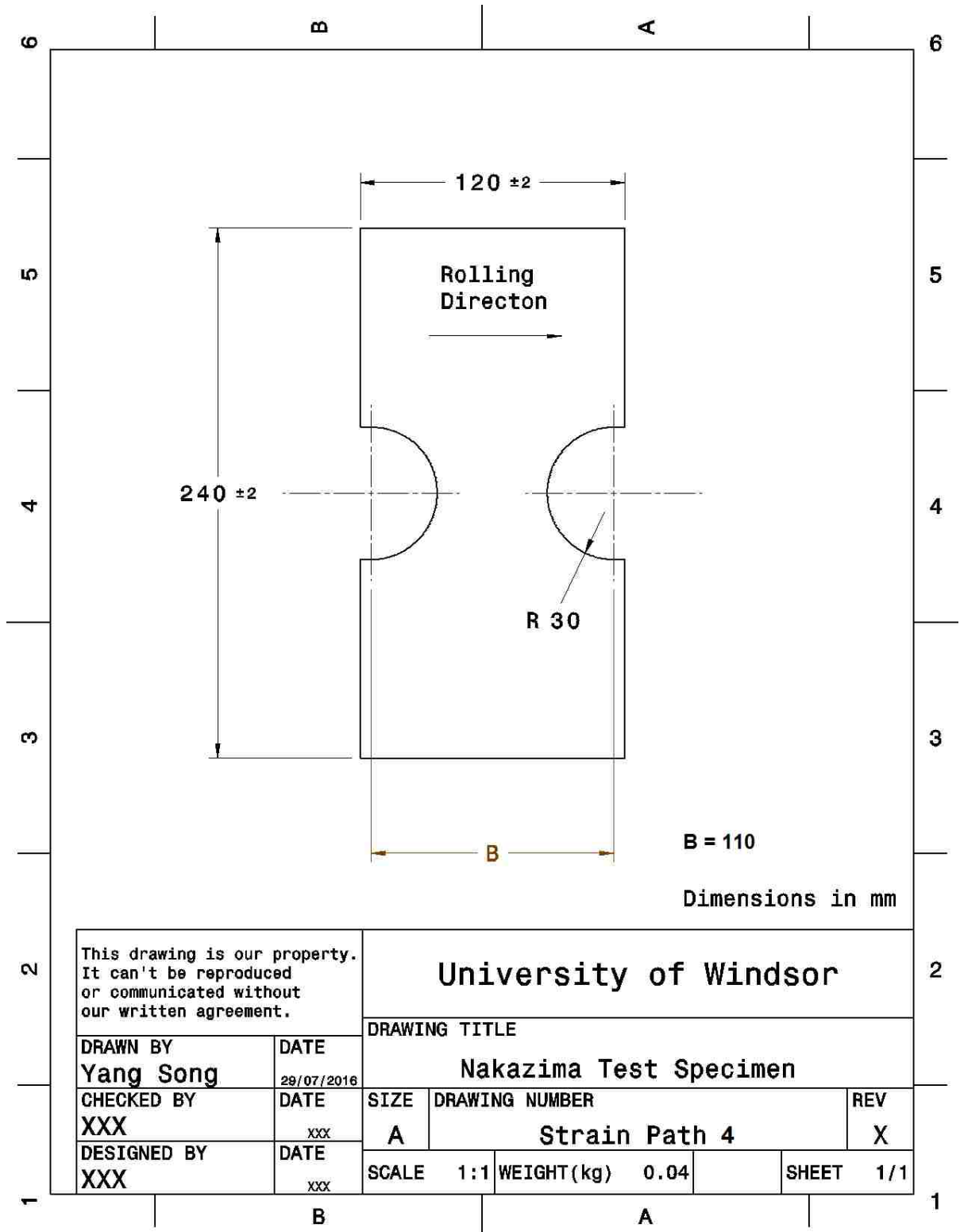
DRAWING TITLE			
Nakazima Test Specimen			

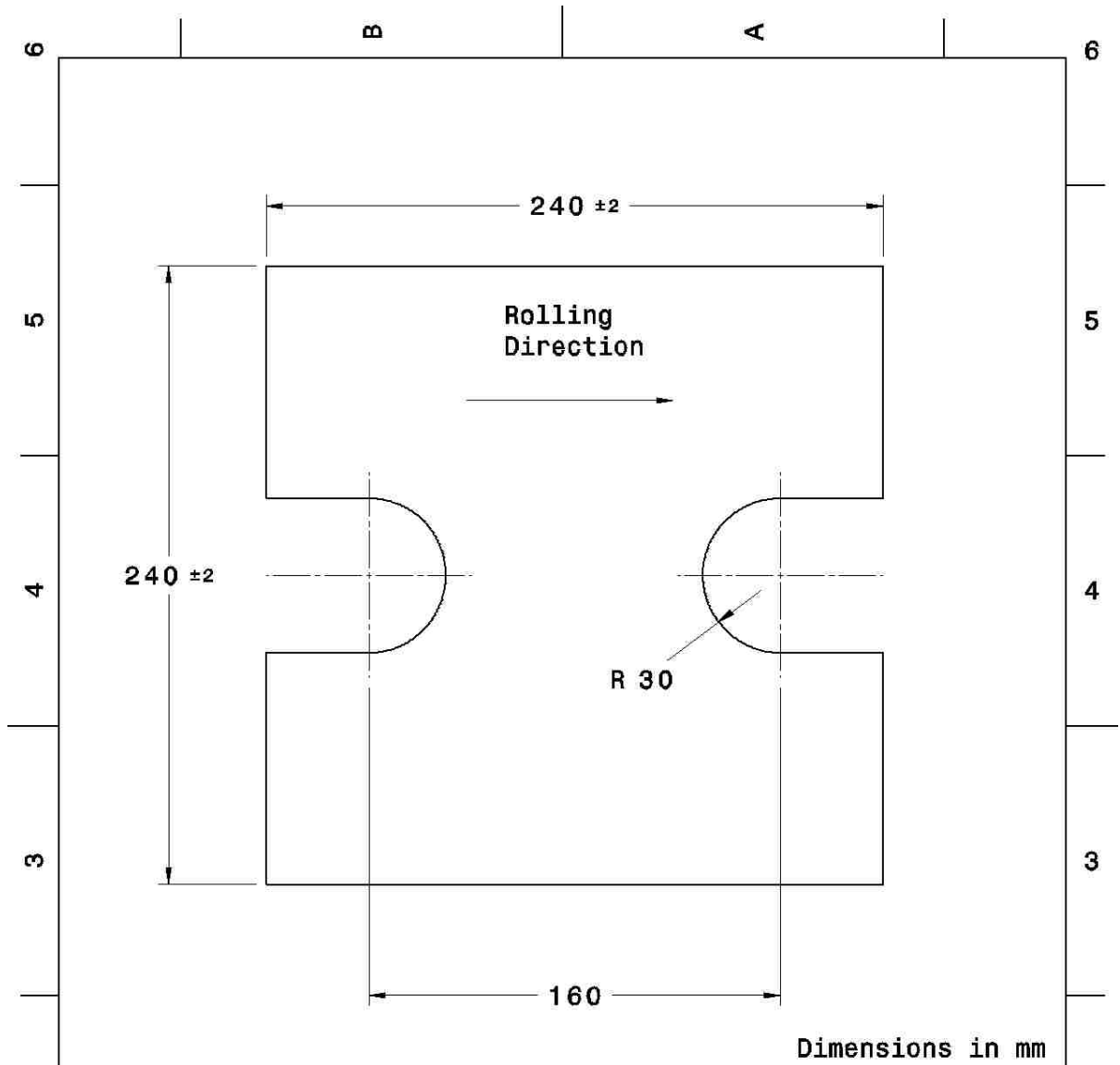
CHECKED BY XXX	DATE XXX
-------------------	-------------

SIZE A	DRAWING NUMBER Strain Path 3	REV X
-----------	---------------------------------	----------

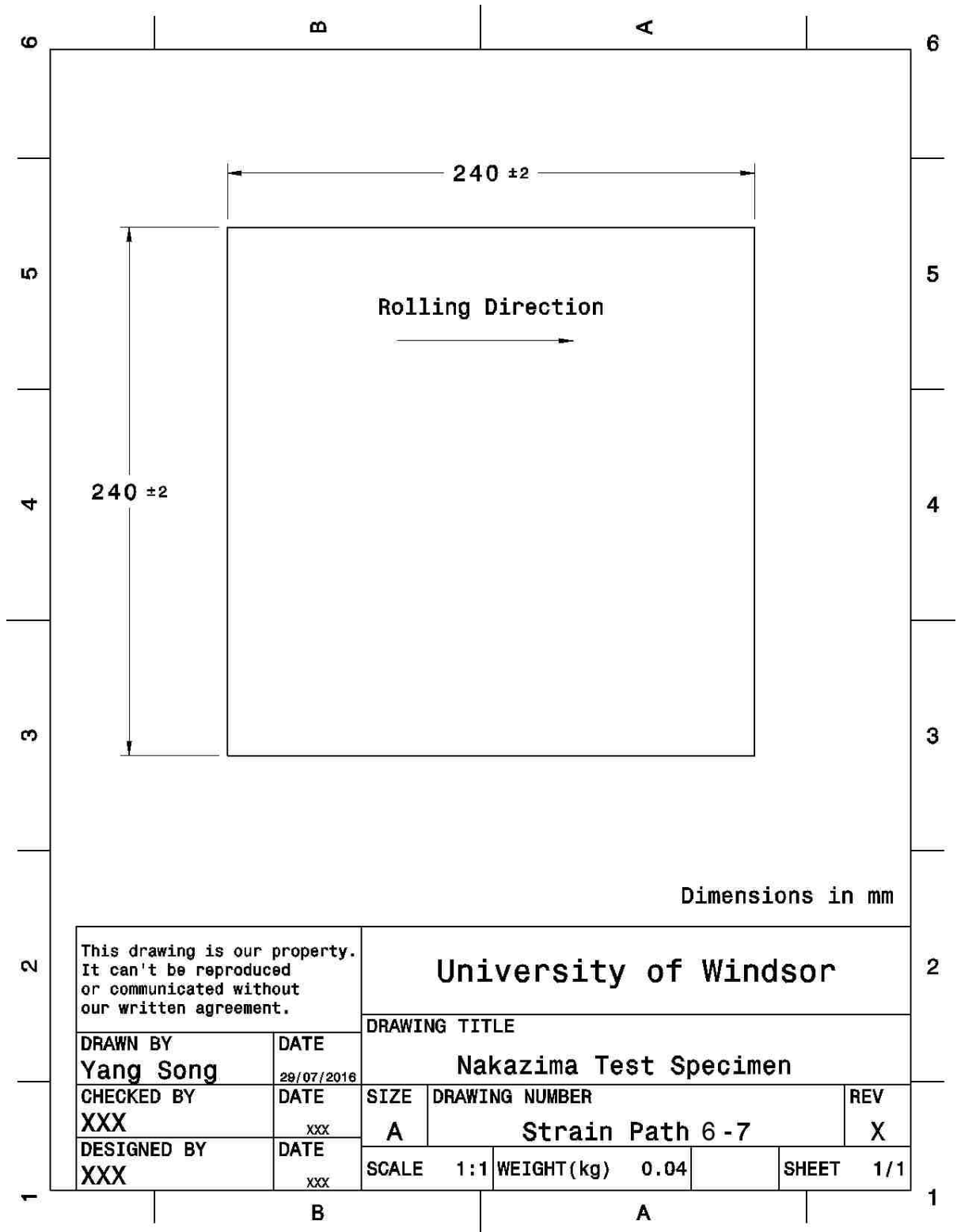
DESIGNED BY XXX	DATE XXX
--------------------	-------------

SCALE	1:1	WEIGHT (kg)	0.04	SHEET	1/1
-------	-----	-------------	------	-------	-----





This drawing is our property. It can't be reproduced or communicated without our written agreement.		<b>University of Windsor</b>			
DRAWN BY <b>Yang Song</b>		DATE 29/07/2016		DRAWING TITLE <b>Nakazima Test Specimen</b>	
CHECKED BY <b>XXX</b>	DATE xxx	SIZE <b>A</b>	DRAWING NUMBER <b>Strain Path 5</b>		REV <b>X</b>
DESIGNED BY <b>XXX</b>	DATE xxx	SCALE <b>1:1</b>	WEIGHT (kg) <b>0.04</b>	SHEET <b>1/1</b>	



## Appendix D – Nakazima Testing Procedure

### Nakazima Test with Superposed SGA and DIC Strain Measurement for Sheet Metals

---

#### Testing Procedure with Apparatus Setup

## Data Processing and Analysis

- xii. Click or press "SAVE"
- xiii. Repeat for all 5-6 grids
- xiv. Click apply and proceed
- d. If existing FLD
  - i. Select old
  - ii. Open file for existing FLD
- e. Label sample with Part ID, as a consecutive integer starting with 1
- f. Prepare a grid numbering system on the sample, with each grid measured having a unique coordinate.
  - i. This coordinate corresponds to the Area ID and Grid ID
  - ii. The Grid ID automatically counts up after every measurement.
  - iii. The Grid ID can correspond to either columns or rows, but keep it consistent across all samples.

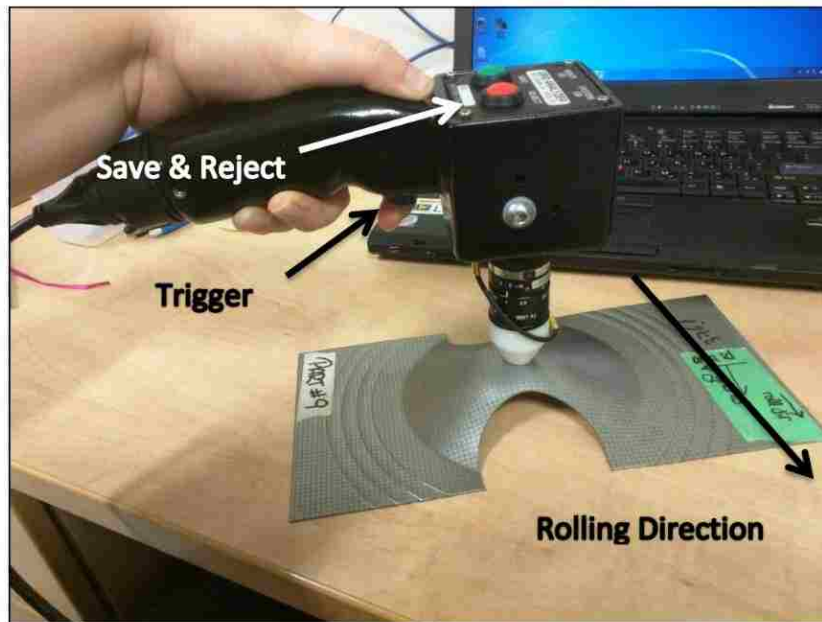


Figure 1: Taking Measurement with Strain Gun Perpendicular to Rolling Direction

- g. Take measurement with strain gun
  - i. Ensure that "auto" option is off under "Severity" (Figure 4)
  - ii. Choose severity of grid (safe, moderate, unsafe)
  - iii. Take perpendicular to rolling direction (Figure 2)
  - iv. Line up the red cross within grid. Keep it as straight and centered as possible (Figure 3)
  - v. Pull trigger to capture image
  - vi. If shape of grid is not well represented by the software, there are 2 options:

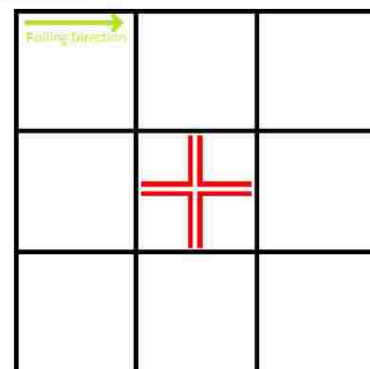


Figure 2: Centered red cross in grid on screen



1. Click or press "REJECT" and take a new picture
  2. "Find grid manually" – follow the instructions on screen
- vii. Click or press "SAVE"
- h. At the end of row/column, increase Area ID by 1 and press "Apply"
  - i. Repeat steps g and h for all areas of interest on sample
  - j. When part is finished, increase the Part ID by 1, change the Area ID to 1
  - k. Repeat steps e-j for every sample of interest
  - l. If severity needs to be changed at any time, use "Browser" to find grid and change severity (Figure 4)

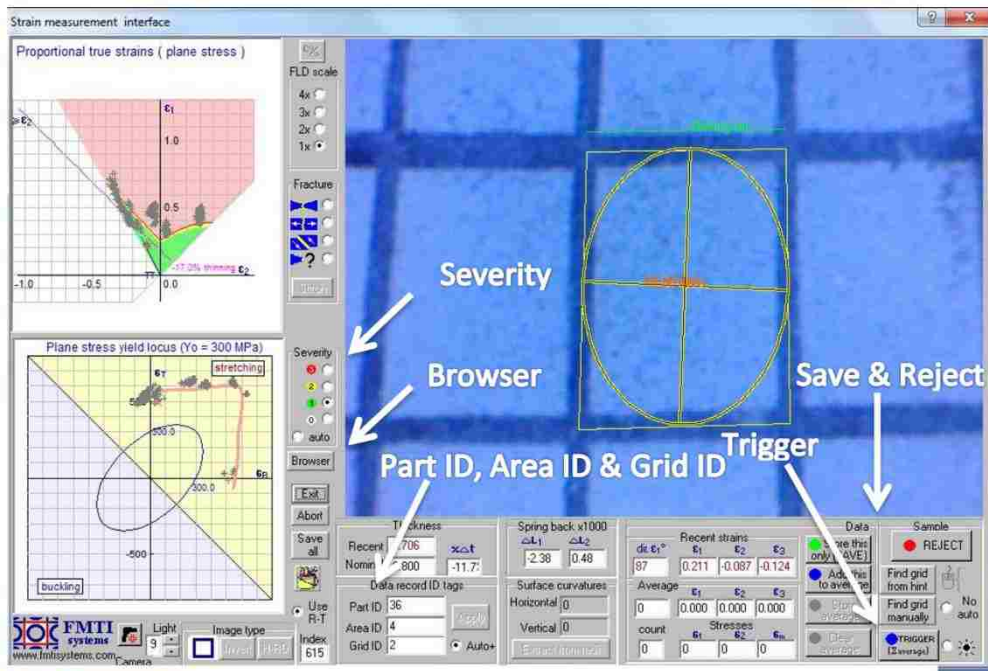


Figure 3: FMTI Software

- m. Dump data
    - i. Click "Write text file" in the top bar of the FMTI software
    - ii. This file can then be opened in excel and saved as a \*.xlsx file or a \*.csv file to be used in other applications.
- II. SGA post processing
- a. Open text file in excel.
    - i. File type is Delimited
  - b. Skip parts c & d if "Format txt Document.xlsm" is available
    - i. Paste all data from exported text file into "PASTE DATA HERE" tab in Format txt Document.xlsm
    - ii. Go into "Formatted Data" Tab and click "Click Here to Format"
  - c. Delete all rows up to "Part ID, Area ID, Grid ID etc." titles

	A	B	C	D	E	F	G	H	I
1	Part ID	Area ID	Grid ID	e2 %	e1 %	e2 minor	e1 major	Tag 0123	Tag 0123
2	1	1	1	1.9	20.7	0.0186	0.1878	1	1

Figure 4: Correct order of columns

#### Document Revision Log

Revision	Person	Date	Details
A	Y. Song/A. Rose	10/05/2016	Document Created
B	Y. Song	10/25/2016	DIC/Analysis minor revision due to changes in MatLAB codes
C	A. Rose	12/7/2016	Added SGA Post Processing section

## Appendix E – Nakazima Testing Setup

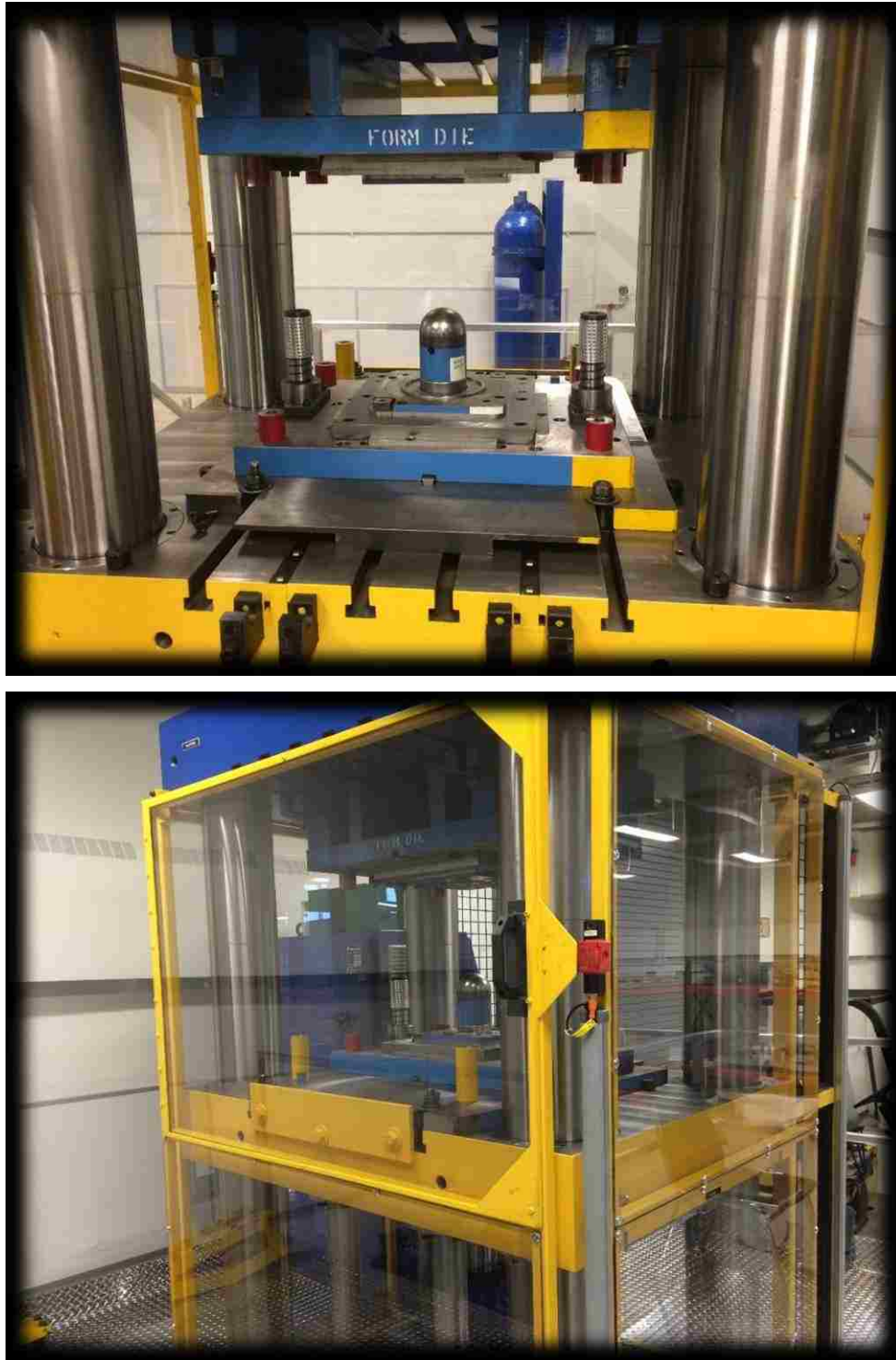


Figure 59 – Nakazima test setup

## Appendix F – Finite Element Results Verification

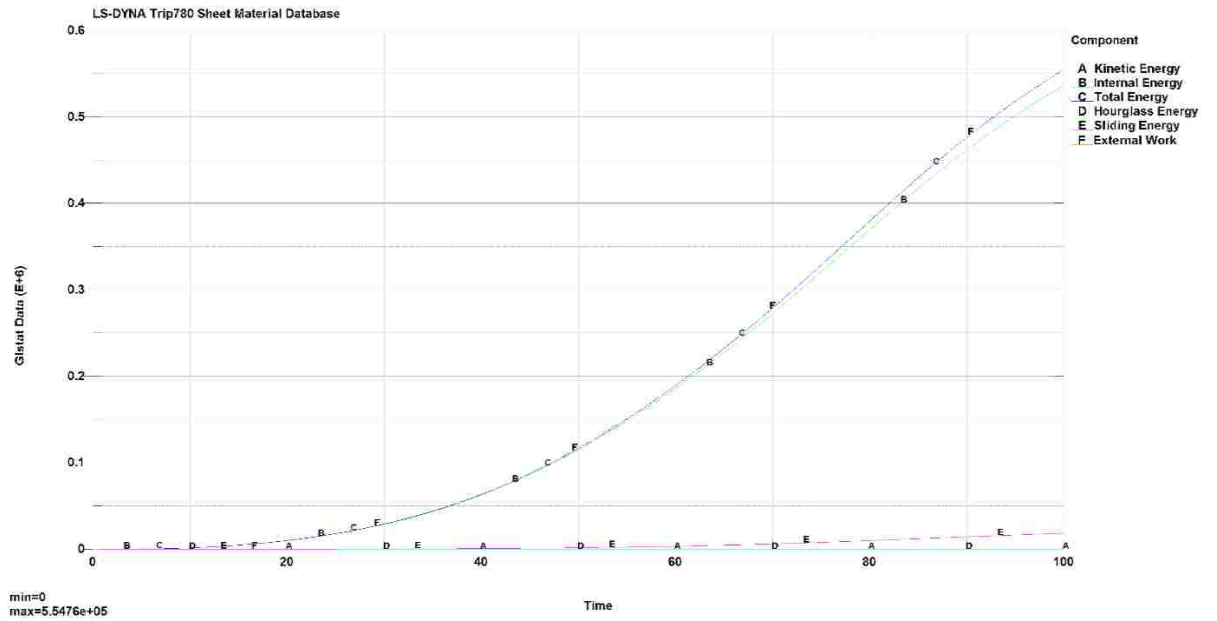


Figure 60 – Energy plot for the entire model of simulation

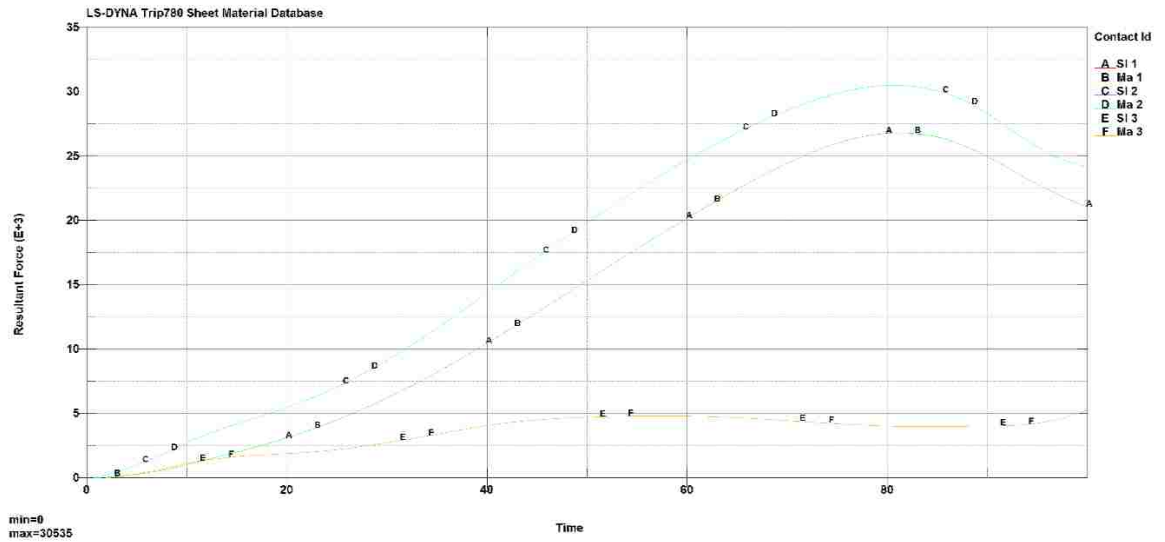


Figure 61 – Contact force couples, No.1, 2 and 3 represent punch-specimen, upper die-specimen and lower die-specimen.

## Vita Auctoris

NAME: Yang Song

PLACE OF BIRTH: Wuhan, PR China

YEAR OF BIRTH: 1990

EDUCATION: Dalian Mapleleaf International School,  
Dalian, China, 2009

University of Windsor, B.A.Sc., Windsor,  
ON, 2014

University of Windsor, M.A.Sc., Windsor,  
ON, 2017